MICROSTRUCTURE AND CONDUCTIVITY OF THE SODIUM NICKEL CHLORIDE (ZEBRA) BATTERY CATHODE

MICROSTRUCTURE AND CONDUCTIVITY OF THE SODIUM NICKEL CHLORIDE (ZEBRA) BATTERY CATHODE

BY

TANNAZ JAVADI-DOODRAN, M. E. Sc, B. E. Sc

A Thesis

Submitted to the School of Graduate Studies

In Partial Fulfillment of the Requirements

For the Degree

Doctor of Philosophy

McMaster University

Doctor of Philosophy (2012) McMaster University

(Materials Science & Engineering) Hamilton, Ontario

TITLE: Microstructure and Conductivity of Sodium Nickel Chloride (ZEBRA) Battery Cathode

AUTHOR: Tannaz Javadi-Doodran, M. E. Sc. (Tarbiat Modares University), B. E. Sc.

(International University of Qazvin)

SUPERVISOR: Professor Anthony Petric

NUMBER OF PAGES: xvi, 154

ABSTRACT

The microstructure of the ZEBRA cells was examined at different cycle lifetimes. Various methods of sample preparation were used to remove the $NaAlCl_4$ electrolyte and expose the cathode microstructure. Features such as layered $NiCl_2$ crystals, large NaCl grains and needle-like $FeCl_2$ phases were observed by SEM. The results indicate that nickel particles grow in size with age of the cell. Moreover, the presence of both Na_6FeCl_8 and $NiAl_2Cl_8$ phases was confirmed by XRD. Thermodynamic modeling was used to predict the phases expected when a cell has undergone overcharge or overdischarge during cycling. It is postulated that some phases observed in the cathode at room temperature may be artifacts due to transformations that occur during cooling and do not exist at the operating temperature.

The presence of isolated nickel particles within the cathode was confirmed by SEM and FIB techniques. Furthermore, the conductivity of the $NaAlCl_4$ electrolyte was measured at high temperatures and various additives were used to make the electrolyte a mixed ionic-electronic conductor.

A special cell was designed to measure the conductivity of hygroscopic and volatile electrolyte at high temperatures. The best conductivity was obtained when using 0.2 mole fraction Bi as an additive to the $NbCl_5$+$NaAlCl_4$ mixture (Nb:Na=0.3, Bi:Nb=0.2). The conductivity values were doubled between 190 and 500˚C. The DC measurements confirm

the presence of electronic conductivity in Bi+$NbCl_5$+$NaAlCl_4$ mixtures. In addition, the effect of NaF and Na_2S on the conductivity of the $NaAlCl_4$ electrolyte was measured.

ACKNOWLEDGEMENTS

Most importantly I would like to thank my supervisor Dr. Anthony Petric. He has taught me so much and has provided me with excellent guidance throughout the course of this study. I am grateful for the many opportunities he has provided me with to present my work at international conferences and to meet others in the field of energy. His support and encouragements has been deeply appreciated.

I would also like to thank my supervisory committee members Dr. Gary Purdy and Dr. Gianluigi Botton for their valuable suggestions and comments that enhanced the quality of this research.

I am also deeply grateful to Dr. Gu Xu whose kind helps and patience made my PhD track enjoyable.

The following people are thanked for their assistance with the experimental work:

Dr. Glynes de Silveira, Dr. Steve Koprich (SEM training), Chris Butcher (optical microscopy training) and Julia Huang (FIB) from the Canadian Center for Electron Microscopy (CCEM), Dr. James Britten and Wen He Gong from the McMaster Analytical X-ray diffraction (MAX), Michael Palme and Jim Garret for glassblowing shop, Doug Culley from MSE labs and Ed McCaffery for solving my computer problems. I would also like to thank administrative staffs, Diana Maltese, Nanci Cole, and Jane Mah.

I would like to acknowledge the financial support of the Natural Sciences and Engineering Research Council of Canada (NSERC) and Vale Canada. I am also grateful to Fiamm SoNick Company, Stabio, Switzerland, for providing the ZEBRA cells. Special Thanks are due to the Brockhouse Institute for Materials Research (BIMR) at McMaster for assistance with sample preparation and analysis.

My deepest gratitude goes to my parents for their eternal helps and supports throughout my life. I am indebted to my father, Vadood Javadi-Doodran, and my mother, Zahra Javar, for their unconditional care and love.

I would also like to express my gratitude to my sisters, Elmira and Ramona, for their supports and valuable encouragements.

Last but not the least I would like to express my warmest and most heartfelt thanks to my loving husband and best friend, Damon, for his understanding and patience during this research. His love, encouragements, and endless support have great contribution toward completion of this work.

TABLE OF CONTENTS

LIST OF FIGURES

LIST OF TABLES

1. INTRODUCTION

The major contributing factor of global warming is high carbon dioxide emissions which has led to a great investment in alternative clean energy such as wind and solar. However, there is a problem of intermittency with solar and wind energy which prevents them from contributing to the grid in the same way as conventional sources of energy. In this case, the difference in power would have to be compensated by other types of generators. A battery can respond quickly and compensate the difference. In fact, the battery is the key enabling device that can store energy and ensure a balance between intermittent supply and cyclical daily demand when the electricity is generated through green energy alternatives.

The ZEBRA battery is a high temperature (260-300˚C), high energy density (90 Wh/kg) battery that is capable of fulfilling the essential requirements for storing electricity [1]. The ZEBRA battery was first introduced in 1978 in South Africa [2] and the term ZEBRA is an abbreviation of Zeolite Battery Research Africa Project. The ZEBRA acronym is also stands for Zero Emission Battery Research Activities [3].

In the past decade, this battery has been manufactured by MES-DEA Company in Stabio, Switzerland. During the term of this thesis, the company name changed from MES-DEA to FZ SoNick to Fiamm SoNick.

Na-$NiCl_2$ is the technical term for this battery. It contains a liquid sodium anode separated from positive electrode by a ceramic electrolyte called β"-Al_2O_3. The positive electrode consists of transition metal chlorides ($NiCl_2$/$FeCl_2$) and excess metals (Ni/Fe) which is impregnated with liquid $NaAlCl_4$ electrolyte [4-5]. Moreover, the power density of this battery is 150 W/kg which makes it an efficient device for powering electric vehicles [1]. Besides the high energy density and high power density, what makes the ZEBRA battery so attractive is the abundant and low cost primary elements (Na, Al, Cl, and Fe) that are used in its fabrication. In addition, the ZEBRA battery has long life, deep discharge cycling ability in which it can withstand at least 1000, 100% DoD charge/discharge cycles [2, 6].

Amidst all promising features, further improvement to the ZEBRA battery could be realized by eliminating intermittent degradation which is related to the relatively high impedance of the positive electrode. This high impedance is due to electrode kinetics, electrode morphology, and cell configuration [2].

There have been continuous process developments to improve ZEBRA battery performance. The energy density and the power density of these cells were improved by optimizing cell geometry [1] and cathode composition [1, 7]. For instance, additives such as sodium halides, iron, and sulfur along with the clover leaf design of the ceramic electrolyte have increased the specific energy to 140 Wh/kg per cell [7] and specific power to 200 W/kg per cell [1]. However, there are still some problems with premature

cell degradation during cycling at 80% depth of discharge (DoD). This degradation can be related to changes in cathode microstructure during cycling which lead to irreversibility of the cell reaction.

In addition, nickel metal is the most expensive material used in the ZEBRA battery. The percolating network of Ni particles is responsible for providing electronic conductivity within the cathode. Therefore, an excess amount of Ni is used to guarantee the formation of the above network. However, the microstructure investigations reveal that not all Ni particles are active in the cell reaction as during large numbers of cycles, some of them form individually within the cathode while they are surrounded with only ionic conductors. The inactive Ni particles increase the internal resistance of the cell and therefore, cause capacity loss. Consequently, introduction of a mixed conductive electrolyte could allow the individual Ni particles to participate in the reactions and thus, prevent the capacity loss caused by gaps in the Ni backbone. In that case there is no need to use a high amount of expensive Ni particles just to maintain the Ni backbone structure.

This thesis addresses the microstructure of the cathode, thermodynamic modeling of the cell reaction and the electrical conductivity of the molten salt component of the cathode. The cycling reaction of the ZEBRA cell during normal, overcharge, and overdischarge conditions is modeled by FactSage thermodynamic software. The microstructure and the thermodynamic modeling results will be discussed in the first

part of Chapter 5 and the second part will focus on the electrical conductivity of the liquid $NaAlCl_4$ electrolyte. Furthermore, the effect of various additives for making a mixed conductive electrolyte will be discussed in this section.

A special conductance cell was designed. The details of the cell construction will be explained in Chapter 3.

The literature review, research objectives and conclusions are discussed in Chapters 2, 4, and 6, respectively.

2. LITERATURE REVIEW

2.1 ZEBRA cell

The sodium/metal chloride battery (ZEBRA) contains sodium metal as the anode and $NiCl_2/FeCl_2$ as the cathode. The anode is separated from the cathode by a ceramic Na- β"-Al_2O_3 solid electrolyte which is a Na ion conductor but an insulator for electrons and anions [4]. As the active cathode materials in these cells (MCl_2, NaCl, and Ni) are solid state at operating temperature, liquid $NaAlCl_4$ is used as a secondary electrolyte to facilitate sodium ion transport inside the positive electrode [5]. The cell is operated at *ca*. 300°C to benefit from higher conductivity of the solid electrolyte [1] and higher diffusivity among solid reactants in the cathode.

The ZEBRA cell uses the same liquid Na anode and β"-Al_2O_3 electrolyte as the sodium-sulfur cell but the liquid sulfur has been replaced by a solid metal chloride [2-8].

Both $NiCl_2$ and $NaAlCl_4$ are hygroscopic and difficult to handle. Therefore, the standard practice is to load the cells in the discharged state, i.e., by adding a granulated mixture of nickel powder and NaCl to the cell and filling the voids with liquid electrolyte [5, 9-10].

2.2 Cell design

A schematic design of the ZEBRA cell is shown in Figure 2.1 [8] and its different components are described in detail in the following sections.

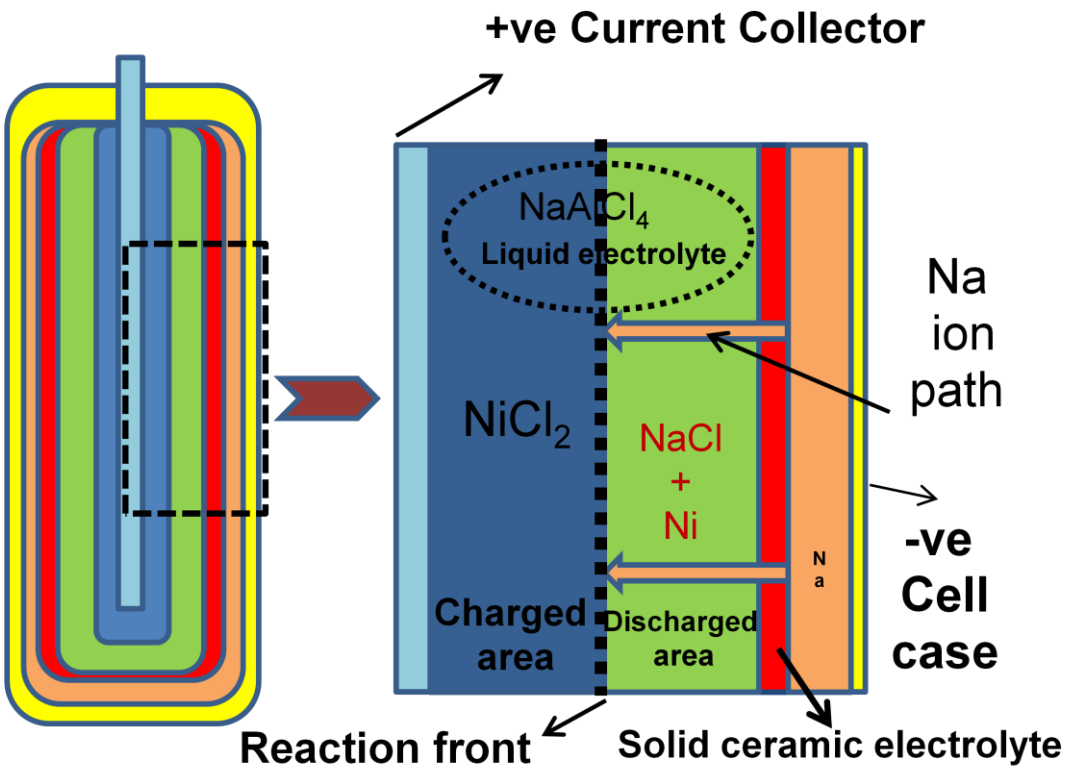

Figure 2.1 Schematic of the ZEBRA cell showing discharge reaction.

2.2.1 The outer cell case

The ZEBRA cell is enclosed in a steel case that is coated with nickel. The thickness of the steel case is about 0.3 mm. As the steel case is in direct contact with

sodium metal, it should be resistant to both the liquid sodium metal and air. Moreover, it must be leak tight to prevent sodium loss.

In addition, the cell contains steel metal foil wicks in close contact with the β"-Al_2O_3 surface in which the liquid Na is drawn up along the electrolyte by capillarity. The role of these wicks is to decrease the contribution of the negative electrode to the overall cell resistance by maintaining a high surface area on the anode side, especially when the sodium level is low (discharged state); they also make good electronic contact with the ceramic tube during initial charging [8].

2.2.2 The negative electrode

The liquid Na metal (negative electrode) forms by reduction of NaCl and is titrated through the ceramic electrolyte during the first charge. The sodium metal is stored between the ceramic electrolyte and the steel case. Sodium is in the liquid state at ZEBRA operating temperature (260-350˚C). It is both volatile and reactive, and thus making a hermetic seal is a critical part of the process.

2.2.3 The solid electrolyte

The ceramic electrolyte plays a twofold role in ZEBRA cells. It acts both as a separator between the liquid constituents of the cathode and the anode and as an ionic conductor [11-12]. Therefore, a proper solid electrolyte must fulfill the following

essential requirements. It should be a good Na ion conductor, electronic insulator, chemically inert to liquid Na and liquid electrolyte, impermeable, and mechanically strong. Only two materials have been found suitable: β-alumina and β”-alumina. These two materials have similar chemical composition but distinct crystal structure. Moreover, the β”-alumina has a significantly higher ionic conductivity [13] ($\geq 0.2\ \Omega^{-1}cm^{-1}$ at 260˚C) that increases with temperature [12-13].

2.2.4 The positive electrode

A practical cathode for a secondary battery must have good reversibility for the cycling reactions, low weight, thermal stability, and chemical compatibility with the solid electrolyte [14].

In ZEBRA cells, the cathode consists of transition metal chlorides and excess metal in the charged state. The transition metals are Ni and Fe.

The open circuit voltage (O.C.V) of the $FeCl_2$ cell is 2.35 V at 250˚C [15-16]. The NaCl-$FeCl_2$ phase diagram has a eutectic at 374˚C. In the absence of NaF, Fe dissolved in the molten salt can enter the solid electrolyte which leads to increased resistance. In this situation, the internal surface of the beta alumina is enriched in iron and becomes darker; moreover, the lattice parameter of the β-Al_2O_3 is changed [11]. Therefore, in the case of using Fe, the operating temperature is in the range of 175˚C - 300˚C [15-16].

In $FeCl_2$ cells, it is also desirable to add a small percentage of Ni metal to the cathode to prevent the formation of $FeCl_3$ phase in case of overcharge (V > 2.75) [17]. Ferric chloride is soluble in the liquid electrolyte; therefore, it may poison the surface of the ceramic electrolyte and increase the resistance of the cell which leads to a decrease in voltage. Owing to the presence of Ni, during overcharge, the Ni metal is chlorinated at 2.58 V and prevents further oxidation of Fe^{2+} to Fe^{3+}. Furthermore, the presence of Ni metal has another advantage in which it changes the morphology of the metal matrix even after a few cycles to large agglomerates which contain very fine Ni-Fe alloy particles [16-17].

In the case of $NiCl_2$, the cell can operate in a wider temperature range between 170˚C and 400˚C [2, 15]. The O.C.V of the $NiCl_2$ cell, as mentioned above, is 2.58 V at 300˚C [18-19]. Moreover, excess Ni powder is always added to these cells to provide good electronic conductivity inside the cathode [1] and to make the cycling characteristics stable [8]. In order to guarantee electronic connectivity throughout the cathode substrate, referred to as formation of a nickel backbone, the cells must undergo a specific cycling regime for their first 12 cycles [20].

2.2.5 The liquid electrolyte

All reacting components of the positive electrode in ZEBRA cells are in the solid state. Therefore, the reaction rates depend on slow solid state diffusion unless a liquid

electrolyte is used to facilitate sodium ion movement within the cathode. One of the best candidates for high sodium mobility is the $NaAlCl_4$ molten salt.

In general, molten salt systems possess a number of advantages that make them much better and more versatile solvents than water and other liquids. They are capable of dissolving a wide range of substances such as water, metals, other salts, oxides, organic substances and nonmetallic elements. Moreover, these systems are stable over a wide range of oxidation-reduction conditions compared to aqueous solutions and provide high decomposition potentials that make them ideal solvents in chemical processes. The factors above, coupled with the higher temperature of molten salt solvents (versus water) facilitate reactions and make them even more practical [21]. For instance, the high conductivity of molten salts along with the relatively high operating temperatures speeds up the electrochemical reactions and therefore, minimizes overpotentials and ohmic losses.

Among different molten chlorides, $NaAlCl_4$ has a much lower melting temperature (156˚C) which allows lower temperature operation. It is a compound of approximately 50% NaCl and 50% $AlCl_3$ and it is a Na ion conductor (0.565 $\Omega^{-1}cm^{-1}$ at 251˚C [22]) in the liquid state.

The $NaAlCl_4$ consists of Na^+ cations and $AlCl_4^-$ anions. In the solid crystal, the chlorine atoms are positioned around the aluminum atoms tetrahedrally and all the

$AlCl_4^-$ tetrahedra are joined together in three dimensions by the sodium ion which is located at the centroid between them [23-24].

In general, the full structure of $NaAlCl_4$ is an arrangement of $AlCl_4^-$ parallel to the (001) plane. They point upward and downward along the c axis in the (020) and (010) planes, respectively. Therefore, pairs of layers of chlorine atoms which coordinate aluminum ions tetrahedrally, are placed at right angles to the c axis and sodium ions are located in a layer in between. Figure 2.2 (a-c) shows the $AlCl_4^-$ tetrahedra and sodium ion arrangement with the planes of chlorine along the c axis. Furthermore, the lattice of $NaAlCl_4$ is orthorhombic [23-24].

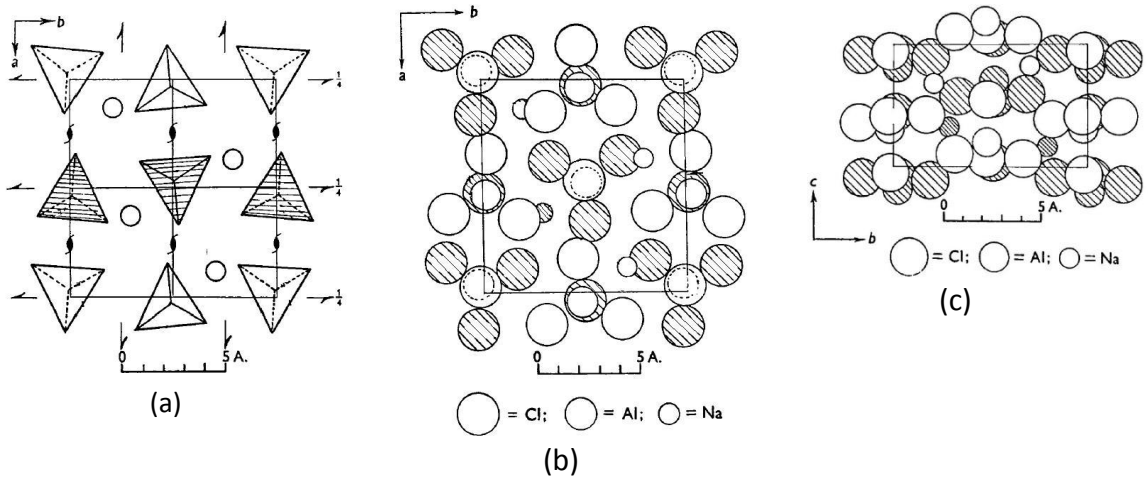

Figure 2.2 a) Projection of $AlCl_4^-$ tetrahedra on (001) plane, b) plane of chlorine layers projected on (001) plane, c) chlorine layers projected on (100) layers [23].

For proper functioning of the ZEBRA cell, it is important to keep the liquid electrolyte in a basic state, i.e., above the 49.75:51.25 $AlCl_3$: NaCl molar ratio at all times

during cycling. A basic melt is maintained by adding an excess amount of NaCl to the Ni electrode.

The solubility of $NiCl_2$ in $NaAlCl_4$ plays an important role, as it has been shown that in acidic melts, a high amount of Ni^{2+} can be exchanged with Na^+ in the ceramic electrolyte, resulting in instability of β"-Al_2O_3 and reducing the conductivity [2]. However, the solubilities of $NiCl_2$, $FeCl_2$, and NaCl inside the $NaAlCl_4$ are very low when the ratio of NaCl: $AlCl_3$ is ≥ 1 and this good property is a characteristic of these cells [15].

The electrical conductivity of mixed solid phase NaCl (s) + $NaAlCl_4$ (s) below the $NaAlCl_4$ melting temperature is higher than $NaAlCl_4$ (s). According to MacMillan, this is attributed to the enhancement of interfacial surface area produced by NaCl crystals which facilitate ionic transport in highly disordered areas [25].

2.2.6 Current collector

While the Ni backbone provides radial conductivity inside the cathode, the hair pin shaped Ni current collector with a highly porous carbon felt sheet in between provides the necessary vertical conduction. The carbon felt keeps the upper part of the cathode wetted by $NaAlCl_4$ [8].

2.2.7 The sealing part

As explained above, due to the presence of different hygroscopic materials within the cell, it is necessary to have a hermetically sealed cell. There are different materials that could be joined to one another, such as two different metals, two different ceramics, and metals to ceramics. In order to join the β”-Al_2O_3 ceramic to a ring of α alumina, a glass paste is applied and heated to melting. In the commercial process, a thermo-compression bonding technique is used to connect a metal collar to the α alumina which is joined to a buss bar by welding [26].

2.3. The electrochemical reactions

2.3.1 Electrochemical reactions under normal operation conditions

The ZEBRA cell reaction occurs through electrochemical oxidation-reduction reactions in electrodes. The electromotive force (EMF) of a cell can be calculated using the difference between the positive and the negative electrode potentials. However, the EMF of a cell depends on the available reactants at the time of reaction. Figure 2.3 shows the possible reactions in a ZEBRA cell [12, 20].

The positive electrode of the ZEBRA cells contains both $NiCl_2$ and $FeCl_2$ as active materials. During normal operating conditions, two discharge reactions can occur. However, the two of them have different EMFs, which limits their stable range of

operation. For instance, at voltages above 2.35 V only $NiCl_2$ reactions take place, whereas below this value both reactions can occur.

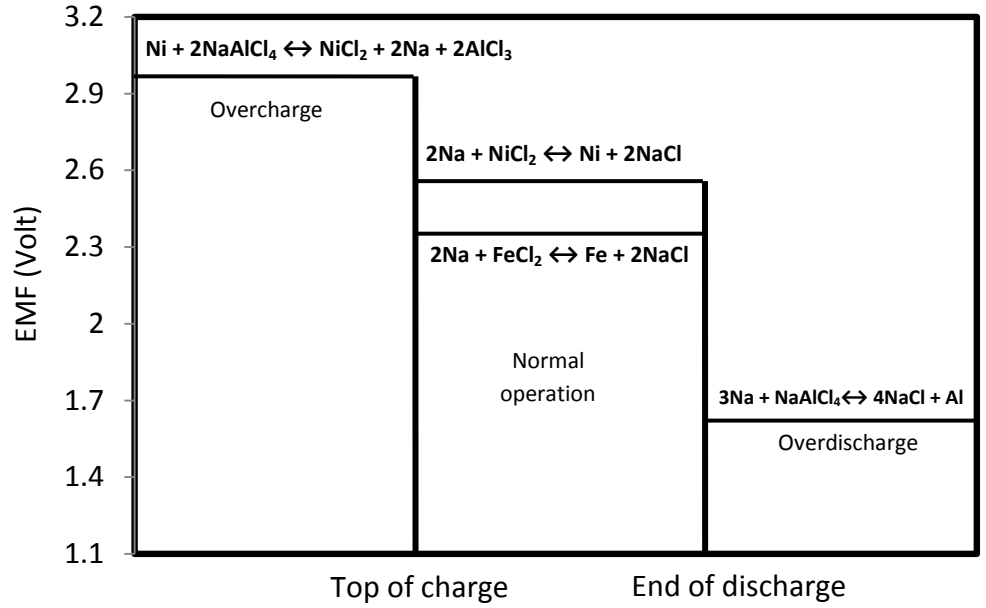

Figure 2.3 Overcharge, normal operation, and overdischarge reactions in ZEBRA cell versus state of charge [12, 20].

During discharge, the following half reactions occur spontaneously:

At the negative electrode:

$$Na \rightarrow Na^{+} + e^{-} \quad (2.1)$$

At the positive electrode:

$$NiCl_2 + 2Na^{+} + 2e^{-} \rightarrow Ni + 2NaCl \quad (2.2)$$

Thus, the net reaction during charging and discharging is:

$$NiCl_2 + 2Na \underset{\text{Charge}}{\overset{\text{Discharge}}{\rightleftharpoons}} Ni + 2NaCl \qquad \text{emf} = +2.58\ \text{V at } 300^{\circ}C \qquad (2.3)$$

During charging, NaCl reacts with Ni metal to form $NiCl_2$ in the cathode while Na ions are removed through ceramic electrolyte and stored as sodium metal. In subsequent discharge, the reverse reaction happens, wherein the Na ions pass through the β"-Al_2O_3 membrane and react with $NiCl_2$ to form NaCl plus Ni metal inside the cathode. This reaction occurs at a potential of 2.58 V at 300˚C [8, 27]. In both charging and discharging directions, the reaction front starts from the inner surface of the ceramic electrolyte and moves toward the current collector [5, 28, 29].

It has been suggested that the formation of Ni from $NiCl_2$ during discharge can proceed via a $Na_xNi_yCl_{2y+x}$ intermediate compound which is kinetically more favorable than direct reduction to Ni. As the Na^+ activity increases at the $NiCl_2/NaAlCl_4$ interface during discharge, the Na^+ rich compounds are stabilized, and therefore, $Na_xNi_yCl_{2y+x}$ may be formed as an intermediate phase [30].

The reaction of $FeCl_2$ as an active material in the cathode occurs as follows during cycling.

$$FeCl_2 + 2Na \underset{\text{Charge}}{\overset{\text{Discharge}}{\rightleftharpoons}} Fe + 2NaCl \qquad \text{emf= } +2.35 \text{ at } 295^{\circ}C \qquad (2.4)$$

Furthermore, XRD data on partially discharged $Na/FeCl_2$ cells also confirmed that NaCl is not formed directly from $FeCl_2$ during discharge. Instead, it happens through an intermediate reaction (equation 2.5).

$$4FeCl_2 + 6Na \rightarrow Na_6FeCl_8 + 3Fe \qquad \text{emf= +2.35 V at 295˚C} \qquad (2.5)$$

Generally, on discharge the Na ions pass across the ceramic electrolyte to react with the $FeCl_2$ and form Na_6FeCl_8 phase on the inner surface of the beta alumina. The continuation of the Na ion insertion leads to further Na_6FeCl_8 formation in the cathode. Finally the activity of Na ions adjacent to the ceramic electrolyte becomes high enough to form NaCl from Na_6FeCl_8 (equation 2.6) [5, 20, 31-32].

$$Na_6FeCl_8 + 2Na \rightarrow 8NaCl + Fe \qquad \text{emf= +2.341 V at 295˚C} \qquad (2.6)$$

An in situ high energy dispersive X-ray diffraction (EDXRD) investigation on the ZEBRA cell during charge revealed that the M (Fe, Ni) Cl_2 phase is mostly generated from Na_6MCl_8 phase rather than NaCl [29].

It is important to charge the cell completely during the first cycle such that all free NaCl is removed. Otherwise, any undissolved NaCl crystals in the middle of the positive electrode can provide nucleation sites for exaggerated growth. In this case, the large NaCl crystals around the current collector can be difficult to dissolve during charging and interrupt the cell performance integrity [8] as Na ions remove from $NaAlCl_4$ instead of NaCl during charging.

On the other hand, the cathode must have a connected pore structure. These pores are needed to provide transport of Na ions through the liquid electrolyte.

Therefore, large NaCl crystals may block the pores, hinder the reaction and increase the resistance of the cathode [33].

2.3.2 Overcharge

When the charge voltage continues to be applied to a fully charged cell, the following reaction occurs at higher voltages and the $NaAlCl_4$ provides a sodium reserve.

$$2NaAlCl_4 + Ni \leftrightarrow 2Na + 2AlCl_3 + NiCl_2 \qquad \text{emf= +3.05V at 295˚C} \qquad (2.7)$$

Although, the overcharge reaction increases the risk of removing Na ions from liquid $NaAlCl_4$, it also has a beneficial consequence. For instance, in case of having failed cells in parallel strings of cells in a battery, the voltage of the failed one can be balanced by overcharging the remaining cells in that string [12].

On the contrary, overcharge in $Na/FeCl_2$ cells results in adverse effects such as increase in cell resistance. The resistance enhancement is due to the presence of Fe in the beta alumina [17] or damage at the beta alumina surface [11]. In fact, iron ions can dissolve into the liquid electrolyte and have access to the ceramic electrolyte by two mechanisms during overcharge.

1) Presence of an acidic melt due to a decrease in the ratio of NaCl in $NaAlCl_4$ to less than 50 mole percent in which the solubility of $FeCl_2$ is increased [11].

2) Formation of $FeCl_3$ due to oxidation of Fe^{2+} to Fe^{3+} under high voltage conditions. The solubility of $FeCl_3$ is high even in a basic melt [16-17].

Therefore, it is possible to say that the overcharge in a $Na/NiCl_2$ battery is more predictable than in a $Na/FeCl_2$ battery [34]. However, the overcharge problem in the $Na/FeCl_2$ battery can be solved by adding a small amount of Ni metal to the cathode to promote the oxidation of Ni to insoluble $NiCl_2$ at high voltages [17].

2.3.2 Overdischarge

During overdischarge, all the nickel chloride has been dechlorinated and any further discharging leads to the following reaction:

$$NaAlCl_4 + 3Na \rightarrow Al + 4NaCl \qquad (2.8)$$

It is possible that the ceramic electrolyte fractures eventually due to further discharging. Since there is no sodium metal left, the ceramic electrolyte can act as a sodium reservoir and this depletes Na from beta alumina, converting it to alpha alumina which is an insulator.

However, during cell fabrication, equation (2.8) applies and therefore, overdischarge capacity can be added to the cell by adding Al to the cathode. During first charge the above equation runs in the reverse direction. The aluminum metal reacts with excess

NaCl and provides extra sodium metal. This increases the overdischarge capacity of the cell which then can help to discharge the cells safely [20, 26].

2.4 ZEBRA properties

The ZEBRA battery has many attractive characteristics that make it a prime candidate for applications such as vehicle propulsion and electricity storage. Some of its desirable features are described below:

1- Cell failure mode [35]:

As the ceramic electrolyte is brittle, there is a risk of a cell crack or seal break during battery operation. In this situation, the liquid salts react with liquid Na (T_m = 97.8˚C) and produce NaCl and aluminum. The reaction is similar to what happens during overdischarge (equation 2.8)

This results in a short circuit with a conductive path through the cell. Therefore, in a 200 cell stack, only one cell is lost and the battery can continue to be operated [12].

2- 100% coulombic efficiency

Besides the charge and discharge reactions during cycling, there are no side reactions in the ZEBRA cell which lead to 100% coulombic efficiency, theoretically [34].

This feature also makes the state of charge estimation simple, i.e. Ah charge in = Ah discharge out [36].

3- Safety

The ZEBRA battery has been tested repeatedly and has passed all the safety tests successfully. The normal operating voltage in a $Na/NiCl_2$ cell is 2.58 V whereas the reversible overcharge reaction occurs at higher voltages; therefore, a specific voltage limit, for instance 3.03 V, is defined by the controller and as the charging voltage reaches the limit, current flow stops and the cells are safe against overcharging. Moreover, in case of cells cracking in an accident, the liquid Na reacts with liquid electrolyte (similar to over discharge reaction) to form solid Al and NaCl as final reaction products [12, 16, 30].

4- Life time

The ZEBRA cell has been operated to a long cycle life of 3500 nameplate cycles [12, 34].

5- Zero maintenance [34]

6- High cell voltage [2, 35]

7- High theoretical specific energy (790 Wh/kg) [2, 35]

8- Broad range in operating temperature (260-350˚C) [2].

2.5 Energy improvement

The ZEBRA battery is well known for its high energy density of approximately 140 Wh/kg per cell [7] and around 90 Wh/kg for a complete battery [1]. Generally, the energy of a cell can improve by increasing its capacity. In the early stages of ZEBRA development, the energy density of a cell was around 94 Wh/kg which improved to 140 Wh/kg by using different additives and changing the chemical composition of the positive electrode. The role of each is considered in turn [7].

2.5.1 Aluminum

Adding a small amount of aluminum powder to react with NaCl during the first charge provides the following useful functions.

$$Al + 4NaCl \rightarrow NaAlCl_4 + 3Na \qquad emf = -1.6\ V \text{ at } 300^{\circ}C \qquad (2.9)$$

- More metallic sodium is produced and stored in the anode side.
- More liquid electrolyte is generated; guarantee better ion conductivity inside the cell.
- The aluminum powder addition provides useful porosity inside the cathode and ensures full charge acceptance on the first charge [7].

2.5.2 Sodium fluoride

In Na/$FeCl_2$ ZEBRA cells, the presence of NaF additive is necessary to prevent an increase in cell resistance. $FeCl_2$ is more soluble in $NaAlCl_4$ than $NiCl_2$ and it has been shown that under extreme conditions, such as high temperature and voltage, the Fe ions can be ion exchanged with beta alumina and consequently, the cell resistance increases [11]. However, it is believed that the solubility of Fe can be suppressed by NaF. Doping the cathode with NaF also increases the tolerance to overcharge [7].

While high energy density was obtained in early stages of ZEBRA development, achieving a reliable power density requires a great deal more effort [1].

2.6 Power improvement

The power density in individual ZEBRA cells is 200 W/kg which is reduced to 150 W/kg at the battery level. Originally, having round tubular β”-Al_2O_3 as the solid electrolyte, yielded about 80 W/kg power density; therefore, several modifications were made to increase this value to 150 W/kg [1].

2.6.1 Geometric factors

One of the main factors which affect the power loss is the increase of cell resistance. Figure 2.4 shows the contribution of different cell components to cell resistance by increasing depth of discharge. The resistance variations of the solid electrolyte, negative electrode, and metallic anode components are constant with DoD (depth of discharge) whereas, the resistance of the positive electrode increases with increasing DoD. As the reaction front starts from the surface of the ceramic electrolyte during both charging and discharging, the ionic resistance of the liquid electrolyte increases due to the larger distance that must be passed between ceramic interface and reaction zone which means increasing resistance with increasing DoD. The most successful aspect of reducing the resistance and increasing the power was changing the shape of the solid electrolyte to clover leaf design. By having a clover leaf shaped cross-section, the thickness of the positive electrode is reduced and the surface area of the ceramic electrolyte is increased which leads to enhanced power density of 115 W/kg. Figure 2.5 shows the cross section of the cylindrical and clover leaf shapes of the β”-Al_2O_3 electrolyte and Figure 2.6 depicts the positive effect of a clover leaf shaped cell in reducing cell resistance [1].

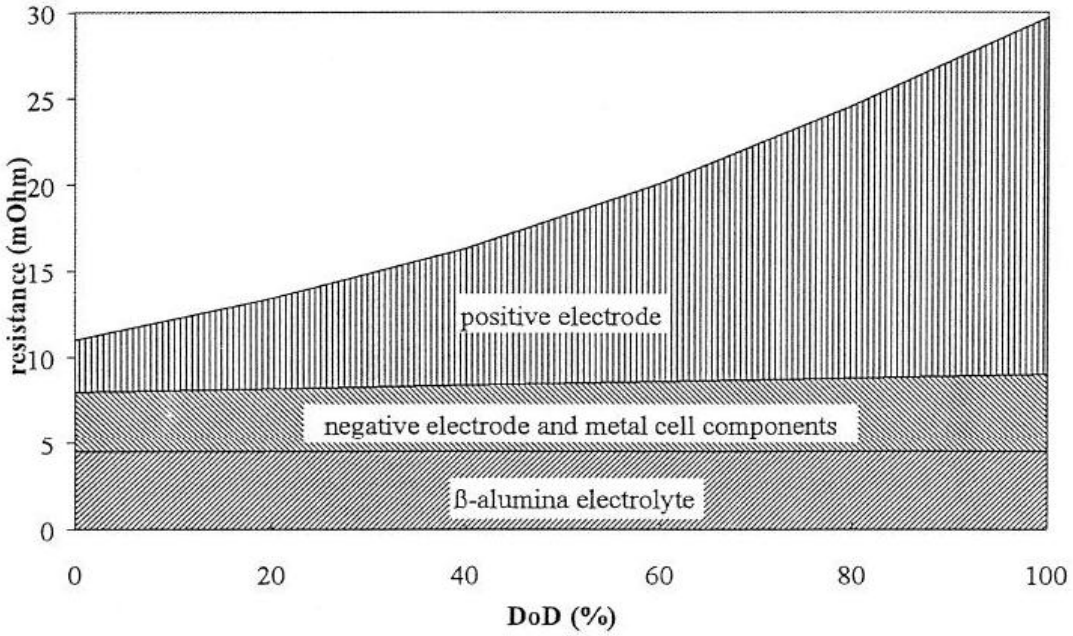

Figure 2.4 Contribution of the cell components to the resistance with DoD [1].

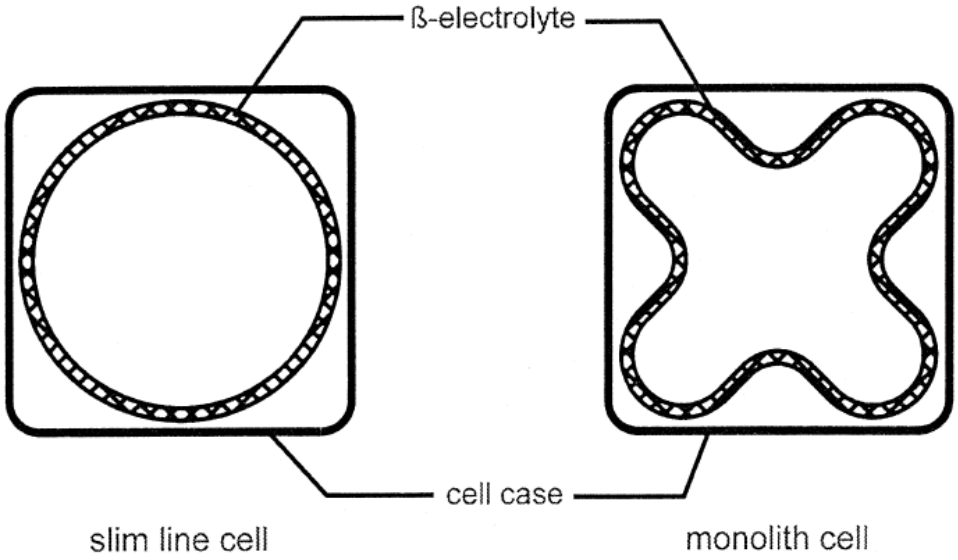

Figure 2.5 Cross-section of the ceramic electrolyte [1].

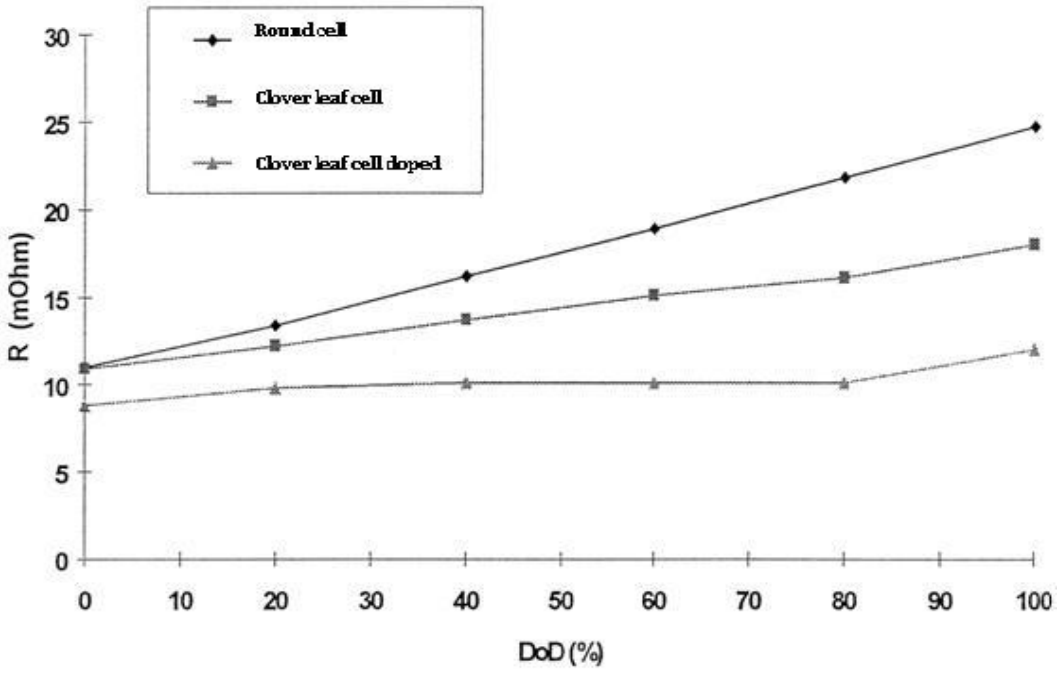

Figure 2.6 The effect of cell geometry in resistance [1].

2.6.2 Doped positive electrode

In order to further increase the power density and reach the 150 W/kg value, the positive electrode was doped with iron.

During regular discharge at 2.58 V, only the $Na/NiCl_2$ reaction occurs and iron remains present as $FeCl_2$. The cell reactions are:

$$NiCl_2 + Na \rightarrow 2\ NaCl + Ni \qquad E= 2.58\ V \text{ at } 295^{\circ}C \qquad (2.10)$$

$$FeCl_2 + Na \rightarrow 2NaCl + Fe \qquad E= 2.35\ V \text{ at } 295^{\circ}C \qquad (2.11)$$

By applying a high current pulse, the working voltage drops below 2.35 V. At this voltage the Na/$FeCl_2$ reaction takes place adjacent to the β"-Al_2O_3 wall which decreases the resistance and reduces the dependence of the pulse power on the DoD of the cell. When the resistance decreases, the working voltage recovers and the $FeCl_2$ forms again by reaction with $NiCl_2$, making the cell ready for the next high current discharge [1, 7-8].

2.6.3 Composite current collector

The resistance of the cell can be decreased further by using a more conductive current collector. The conductivity of copper is 4 times higher than the conductivity of Ni, but copper is more electrochemically active. Therefore, using a nickel coated copper electrode increases both conductivity and electrochemical stability of the current collector. This composite reduces the current collector resistance up to 80% and its contribution to improve cell power is considerable [7-8, 37].

2.7 Capacity improvement

It has been shown that the capacity of the electrode depends on the electrochemical performance and the morphological properties of the cathode. The formation of the poorly conducting $NiCl_2$ layer and the hindering of mass transport by blocking the effective pores inside the cathode led to increased resistance and decreased cell capacity even in the early stage of charge; moreover, the formation of

NaCl crystals during discharge would block the pores with radius smaller than the NaCl crystals. Consequently, it is important to improve the porosity of the cathode to facilitate mass transport during cycling. This improvement is affected by having a distribution of different pore sizes, in which the smaller pores provide higher surface area and the larger ones support the mass transport during cycling [2, 33].

Furthermore, some additives can stabilize cell capacity. It was shown that nickel particle agglomerations cause nearly 50% capacity loss even after 10 cycles. Additions of sulfur to the molten electrolyte prevent Ni grain growth, maintaining a high surface area and stable capacity for many cycles [18, 38-39]. The effect of adding sulfur on Ni morphology was also explained elsewhere [18, 28]. It has been shown that adding 2 wt% sulfur produces large, well defined pores inside the cathode, increasing the material utilization [28]. Moreover, it was shown that adding NaI in combination with sulfur considerably enhances the capacity retention and decreases the cell impedance by two different mechanisms. At voltages lower than the potential for iodine formation (< 2.8 V), the iodine ion improves the capacity and decreases the resistance by modifying the chemistry and morphology of the $NiCl_2$ layer. The second mechanism occurs when the cell voltage reaches potentials higher than 2.8 V. As iodine species have high oxidizing power, their formation at high voltage (>2.8 V) can decrease the $NiCl_2$ layer impedance and produce additional capacity. It has also been shown that further cycling

improves performance, owing to a high solubility of iodine species that can easily reach the intact sites of the cathode and accelerate the reaction kinetics [38].

In addition, the capacity is highly dependent on charge rate. Those cells that are charged rapidly show lower capacity. It seems that the charge kinetics are slower than those for discharge, i.e., the charging rate is more limited than discharging rate, which can be related to the limited amount of NaCl that is able to dissolve and move to the reaction sites during slow charging [28].

This limitation can be amplified in the denser cathode or at low temperatures. Instead, the higher temperatures (260˚C vs. 220˚C) can change viscosity of the electrolyte and facilitate Na^+ ion transport [28].

2.8 Microstructure investigations

The microstructure of the partially charged cathode was investigated ex-situ previously. The different solid phases were identified and the cubic NaCl crystals, lamellar $NiCl_2$ phases along with particulate metallic Ni have been observed. It was also shown that during charging, the NaCl crystals were eroded preferentially at the edges in contact with Ni particles [18]. Furthermore, the Ni particle size was also examined before and after cycling which shows grain growth of Ni particles after several cycles and

capacity loss. However, the growth of Ni particles was controlled by adding additives like sulfur [18] and/or Fe [16].

Moreover, the inner structure of ZEBRA cells has also been investigated by micro-tomography. The two and three dimensional images of the interior ZEBRA cell can be generated by X-ray tomography [40]. However, the low resolution of tomograms has impeded further investigations on details inside the cathode during cycling.

2.9 Electrical conductivity

Electrical conductivity is a measure of the flow of electric current. A high conductivity indicates a material that readily allows the movement of electric charge. The electric charge can be either ions or electrons. In the case of having ions as charge carriers, the conductivity is an ionic type and if electrons are the only responsible charge carriers, the conductivity is an electronic type. The SI unit of electrical conductivity is $(\Omega \cdot m)^{-1}$ but the more common unit is Siemens/cm (S/cm).

2.10 Parameters that influence the electrical conductivity

Ionic conductivity is an intrinsic property of materials that results from movement of ions inside the solution when subjected to an applied electric field. There are different factors such as ionic concentration and mobility that influence the

conductivity of a solution. In order to compare the conductivity values of two different materials, a new term is defined known as molar conductivity (Λ). It can be measured by normalizing the conductivity (σ) using the total concentration (C) [41-42].

$$\Lambda = \frac{\sigma}{C} \tag{2.12}$$

Furthermore, the conductivity of two different materials with the same concentration is not the same, since each ion has a different mobility. Therefore, the mobilities of the ions in solution play an important role in their conductivity. There are different factors that influence the mobility of ions. These factors are related to one another through the following equation.

$$u_i = \frac{|z_i|e}{6\pi\eta R_i} \tag{2.13}$$

In this equation u_i, z_i, R_i , and η are the mobility of the ion "i", charge of the ion, solvated radius, and the solvent viscosity, respectively. "e" is the elementary charge constant.

Therefore, the total conductivity of a solution represents the contribution of ions that can conduct current. The total conductivity can be calculated using equation (2.14) which includes the mobility and concentration of each ion.

$$k = \sum_i |z_i| u_i C_i = F \sum_i |_{z_i}| (\frac{|z_i|e}{6\pi\eta R_i}) C_i \tag{2.14}$$

F is Faraday constant (96,485 C/mol), and C_i is the concentration of ion "i" in mol/cm^3 [42].

2.11 Electrical conductivity of molten salts

The high ionic conductivity and a wide range of stability to oxidation-reduction reactions make molten salts applicable for different chemical and electrochemical studies such as

1- Electrolytes in primary and secondary batteries [24].

2- Nonaqueous electrolytes at room temperature [24].

3- Excellent solvent medium for high temperature chemistry studies [43].

Therefore, different physical properties of these materials such as electrical conductivity have been studied by many investigators [44]. The electrical conductivity of different pure molten salts and binary and ternary molten salt mixtures has been measured [24, 43-53].

As the specific conductance of most molten salts is high (on the order of 1 to 10 S.cm^{-1}), the accurate measurement of conductance of molten salts is difficult. In general, conductivity is measured using following equations:

$$\sigma = \frac{1}{\mathrm{R}} \times \frac{\mathrm{L}}{\mathrm{A}} \qquad (2.15)$$

Where $\frac{L}{A}$ is the cell constant and R is the electrical resistance. The accurate measurement of σ needs high cell constants (between 100 and 1000 cm^{-1}). Capillary type cells fulfill this need. These cells are made of a high melting temperature glass, e.g., quartz or Pyrex and the electrodes can be platinum, molybdenum, tungsten, or graphite [21, 50, 52].

In the following sections, the electrical conductivity of different molten salts is examined.

2.11.1 Electrical conductivity of molten rare earth trichlorides

The molar conductivity of the rare earth trichlorides have been measured using U-shaped conductivity cells and ac measurements. Results show that the formation of polymeric complex anions composed of $GdCl_6^{3-}$ -type octahedra increased by increasing the mole percent of $GdCl_3$ in the mixture which led to a decrease in the molar conductivity of the $GdCl_3$-NaCl and $GdCl_3$-KCl systems. However, at low concentrations of $GdCl_3$, the concentrations of free Na^+, K^+ and Cl^- increased which consequently increased the conductivity of the system.

Comparing the conductivity values of the rare earth trichlorides shows that they are affected by the cation radii and the type of bonding, forming either corner-shared dimeric species or edge-shared species [53].

2.11.2 Electrical conductivity of molten bismuth halides

The electrical conductivity of bismuth halides ($BiCl_3$, $BiBr_3$, BiI_3) has been measured over a wide temperature range. The conductivity values increase with temperature near the melting point, but they decrease at sufficiently high temperatures. Moreover, the negative temperature coefficients of electrical conductivity have been reported for other molten salts such as, $HgCl_2$, $SnCl_2$, CuCl, and ZnI_2 [51]. It is suggested that this behavior is general to most molten salts at high temperatures.

2.11.2.1 The negative temperature coefficients of electrical conductivity in molten salts

Electrical conductivity measurements of molten salts over a wide range of temperatures show that conductivity maxima were observed in numerous systems [51-52, 54-55]. In fact, this behaviour has been reported in different solutions if the conductivities were measured over a very wide temperature range. It was assumed that this behaviour is due to two opposing effects which were occurring simultaneously. On the one hand, an increase in temperature decreases viscosity and enhances the mobility of the ions which increases the conductivity. On the other hand, this temperature increase expands the volume of the solution and decreases the density which leads to increased ionic association and decreased conductivity [51-52]. The higher the ionic character, the lower the decrease in ionization with temperature.

Increasing temperature leads to increased volume. The increase in volume results in increase in void space which has two effects on electrical conductivity of molten salts at high temperature. The presence of these voids at lower temperatures decreases the viscosity and thus increases the conductivity. However, at very high temperatures and low densities, the formation of cation-anion complexes becomes more favourable. In fact, by decreasing density, the average coordination number of the ions decreases [56] which ultimately favours the association with small groups of oppositely charged ions. Indeed at high temperatures, the bonding energy between associated ions becomes larger (covalent bond) which leads to formation of neutral entities which can not contribute to electrical conductivity of the molten salts [51].

Spedding in 1973 [55] attributed the maxima in conductivity of melts to the differences in the basic mechanisms controlling diffusion and conduction in melts.
These two different transport modes (diffusion and conduction) were examined in TlCl within a wide temperature range. It was shown that diffusion increases with temperature, whereas the specific conductivity shows a maximum. Diffusion can occur through movement of individual ions or agglomerated ions. Because of the smaller size of the individual ions compared to agglomerated ones, the individual ions move faster. By increasing temperature not only the movement of the ions becomes faster but also the ionic agglomerates are thermally broken down into individual ions which are capable of moving faster.

Generally, conduction can occur through a combination of diffusion of individual ions and a Grotthus-type mechanism of charge transfer which happens within and between agglomerated ions.

Increased temperature enhances the movement of both individual ions and charges which leads to an increase in conduction. A further increase in temperature causes a formation of individual ions by thermally breaking down the ionic agglomerates. Although the number of individual ions increases, the conduction decreases because the Grotthus mechanism is only effective within agglomerated ions. When the melt reaches the critical point, all individual ions tend to acquire molecular character which cannot contribute to conduction [55].

In order to prove the Grantham and Yosim theory about the increased covalency and ionic association of molten salts at high temperature, Darnell et al. [52], conducted conductivity measurements at high pressure. From the principle of Le Chatelier, applying high external pressure can decrease the ionic association and therefore, the conductivity of the molten salt increases with temperature. Although the increase in pressure can increase ionic dissociation, one should expect an increase in viscosity too. The conductivity measurements of bismuth trihalides at high pressure show the effect of both viscosity and ionic dissociation on conductivity. At low temperatures the effect of pressure on increasing viscosity is predominant; thus, the conductivity decreases.

However, at high temperatures the effect of ionic dissociation dominates and the conductivity increases [52].

2.11.3 Electrical conductivity of chloroaluminate molten salts

The electrical conductivities of chloroaluminate molten salts ($LiCl\text{-}AlCl_3$, $NaCl\text{-}AlCl_3$, $KCl\text{-}AlCl_3$) are more than 0.1 $S.cm^{-1}$ [24]. The conductivity of $NaCl\text{-}AlCl_3$ molten salt has been reported by several investigators [49, 57-58]. Howie and Macmillan determined the conductivity of the $NaCl\text{-}AlCl_3$ binary molten salt within the composition range of 15-30 wt% NaCl at 155-195˚C. Equation (2.16) was derived from experimental data. This equation shows the variation of conductivity of $NaCl\text{-}AlCl_3$ molten salt with temperature and composition within the range of the experiment, where W is weight percent of sodium chloride and T is temperature in degrees Celsius [49].

$$\sigma\ (S.cm^{-1}) = (-0.1594+0.207\times10^{-2}T)-(-0.1475\times10^{-3}T)\ W+\ (-0.4022\times10^{-3}+0.548\times10^{-5}T)\ W^2 \quad (2.16)$$

A thorough study has been done by Janz et al. regarding measurement of physical properties of different molten salts including electrical conductivity of $NaCl\text{-}AlCl_3$. The electrical conductivity of the molten $NaAlCl_4$ (50 mol % $AlCl_3$) is defined by the following equation in the temperature range 187-267˚C [42].

$$\sigma\ (S.cm^{-1}) = -0.0508 + 0.0027\ T - 3\times10^{-8}\ T^2 \quad (2.17)$$

Kryagova [47, 58] in 1939 measured the conductivity of NaCl-50.3 mol % $AlCl_3$ in the 190-270˚C temperature range. The conductivity of the acidic NaCl-$AlCl_3$ mixture was also investigated by Moss in 1955 [47, 59] with higher precision compared to older measurements [57-58]. Moss also studied the conductivity of other alkali metal chloroaluminates such as LiCl-$AlCl_3$, KCl-$AlCl_3$, and RbCl-$AlCl_3$ and compared their electrical conductivities with NaCl-$AlCl_3$. The results show that the conductivity of the melts decreases in a following order:

NaCl-$AlCl_3$ > LiCl-$AlCl_3$ > KCl-$AlCl_3$ > RbCl-$AlCl_3$

In fact, the anomalous behaviour of LiCl-$AlCl_3$ is explained by the high interactions between small Li ions and high polarisable $AlCl_4^-$ which adds partial covalent character to $LiAlCl_4$ and decreases its conductivity compared to $NaAlCl_4$ [50].

Mohandas et al. [50] measured the conductivity of $NaAlCl_4$, $LiAlCl_4$, and $KAlCl_4$ in a higher temperature range. The conductivity data for $NaAlCl_4$ was fitted to the following equation between 160 and 520˚C. T in this equation is in Kelvin:

$$\sigma\ (\mathrm{S.cm^{-1}}) = -1.7262 + (6.36\times10^{-3})\,T - (3.471\times10^{-6})\,T^2 \qquad (2.18)$$

Midorikawa [47, 60] measured the conductivity of NaCl-52.3 mol % $AlCl_3$ and reported the following equation for the conductivity:

$$\sigma\ (\mathrm{S.cm^{-1}}) = 0.408 + 2.35 \times 10^{-3}\,(T - 170) \qquad (2.19)$$

where T is in degree Celsius in the range 170-202˚C.

An excess of $AlCl_3$ in the two-phase mixture $NaAlCl_4$-$AlCl_3$ in its solid state results in a drop in the electrical conductivity value. However, addition of a small amount of $CaSO_4$ significantly improves the electrical conductivity of the mixture [24, 61].

Weppner and Huggins [24], compared the electrical conductivity of different alkali metal chloroaluminates from room temperature to above the melting point. The values at 25˚C are 1.2 $x10^{-6}$, 3.5 $x10^{-7}$, and 3.2 $x10^{-9}$ $S.cm^{-1}$ for $LiAlCl_4$, $NaAlCl_4$ and $KAlCl_4$, respectively. It is reported that the specific electric conductivities at 25˚C decrease significantly with increasing ionic radius of the alkali metal ions due to the size dependent mobility of the alkali metal ions. However, this trend is not confirmed by experiments done by Moss [47, 59] or Mohandas [50].

Matiasovsky [47, 62] calculated the conductivity of $NaAlCl_4$ at high temperature to be 1.27 $S.cm^{-1}$ at 700˚C.

The effect of additional $AlCl_3$ on equivalent conductivity of $LiAlCl_4$ and $NaAlCl_4$ has been investigated by Carpio et al. [48]. The equivalent conductivity of $NaAlCl_4$-$AlCl_3$, $LiAlCl_4$-$AlCl_3$, and $KAlCl_4$-$AlCl_3$ binary systems at $X_{AlCl3}>0.5$ was explained using $2Al_2Cl_7^- \leftrightarrow 2AlCl_4^- + Al_2Cl_6$ equilibrium. This equilibrium has a tendency to shift to the right as the size of the cations decreases. Moreover, the interaction between Li^+ ions and $AlCl_4^-$ is stronger than Na^+ ions and $AlCl_4^-$ which led to formation of more molecular species in $LiAlCl_4$-$AlCl_3$. For the Li^+ containing system, the addition of $AlCl_3$ will shift the above equilibrium to the right and form more neutral Al_2Cl_6 which decreases the

equivalent conductivity of this system, whereas, this is not the case for the $NaAlCl_4$-$AlCl_3$ system [48].

2.11.4 Electrical conductivity of ternary molten salt systems

2.11.4.1 NaCl-CsCl-$MnCl_2$

The conductivity of ternary NaCl-CsCl-$MnCl_2$ mixtures has been studied within the whole range of ternary composition and high temperature range. In order to simplify the composition selection two following parameters were defined:

$$y = 1 - X_{MnCl2} = X_{NaCl} + X_{CsCl} \quad (2.20)$$

and

$$t = \frac{X_{CsCl}}{X_{NaCl}+X_{CsCl}} \quad (2.21)$$

The conductivity measurements were done in a capillary U-shaped cell and the results are shown in Figure 2.7 [44]. It is clear that the conductivity decreases as the amount of CsCl increases. Moreover, a distinct minimum forms at around X_{MnCl2} = 0.33 when t increases. As an alternative, Carmichael et al. plotted the results as molar conductivity (Λ) values (Figure 2.8). It is seen that there is a minimum in molar conductivity of the mixtures at around y=0.6 for t≥0.25. This decrease is attributed to the formation of complex species, such as $MnCl_4^{-2}$, especially in CsCl-rich mixtures which reduce the mobilities of ions within melt [44].

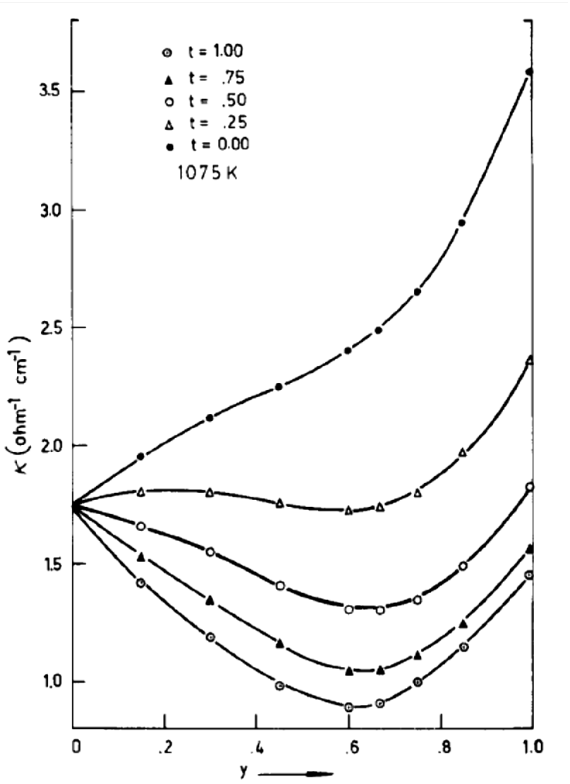

Figure 2.7 Electrical conductivities of NaCl-CsCl-$MnCl_2$ ternary system at 802˚C versus $\mathbf{y = 1 - X_{MnCl2}}$ at constant t [44].

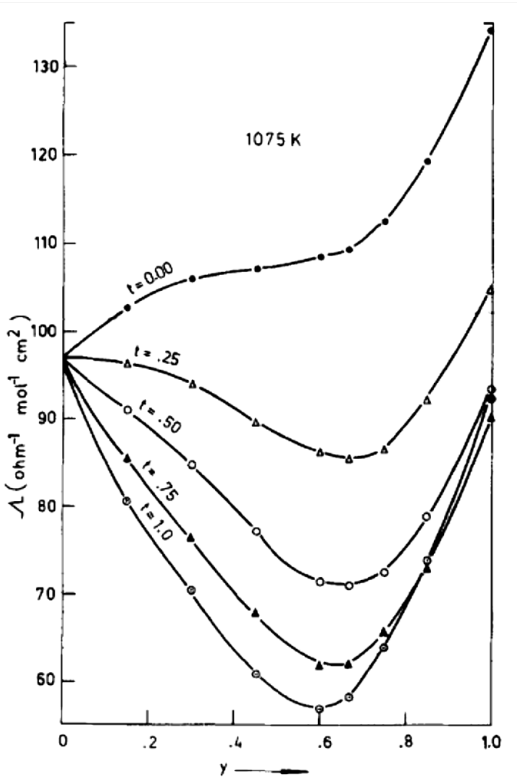

Figure 2.8 Molar conductivities of NaCl-CsCl-$MnCl_2$ ternary system at 802˚C versus $\mathbf{y = 1 - X_{MnCl2}}$ at constant t [44].

2.11.4.2 NaCl-$AlCl_3$-Al_2S_3

The presence of aluminum and sulfur in some galvanic cells such as Na/S batteries provided motivation for studying their electrolyte chemistry. Generally, aluminum metal and sulfur with the Al:S= 2:3 ratio react with alkali tetrachloroaluminate molten salt and form aluminum chlorosulfides.

$2Al + 3S \rightarrow Al_2S_3$ (2.22)

$$Al_2S_3 + NaAlCl_4 + 2NaCl \rightarrow 3NaAlSCl_2 \quad (2.23)$$

The $NaAlSCl_2$ is a highly polymerized compound which can dissolve in equimolar NaCl-$AlCl_3$ molten salt. The specific conductivity measurements reveal that the conductivity decreases with an increasing amount of Al_2S_3 and increases with temperature. The decrease in conductivity with increasing Al_2S_3 is attributed to the formation of highly viscous $NaAlSCl_2$ [47].

2.12 Electronic conductivity of molten salts

Although the ionic conductivity of electrolytes is usually more pronounced, electron transfer plays an important role in electrochemical procedures. In general, the electronic conductivity can be classified into several mechanisms. Besides the most well-known one which is electronic conduction in metals, there are two other electronic conduction mechanisms, namely, the one that happens in semiconductors such as Si doped with impurities, and electron hopping or electron transfer which occurs in compounds containing cations or anions with different valence states.

Generally, few attempts have been made to explain the electronic conductivity of liquid electrolytes compared to electrode materials due to their complexity. Moreover, the energy band is typically defined for solid materials. However, there are some investigations trying to present an electronic band structure for molten salts [63-

65]. Frequency Energy Level (FEL) [66] and Molten Salt Bands [64] are examples of such models. In the FEL model, an electron with specific energy ϵ_+ (ϵ_-) is localized on an individual positive (negative) ion within an electrolyte. Due to thermal fluctuations a Gaussian broadening happens for each ionic level in a way that their energy level can cover one another partially. Figure 2.9 a and c illustrate this model [64], where in the molten salt band model, the molten salt is considered an ionic crystal which is highly disordered in which each type of ion has a chance to locate in any specific site. Figure 2.9 b and d show the electronic band structure for ionic crystals and the effect of spatial disordering on its configuration. In Figure 2.9 b, the conduction and valence bands are being expanded due to electronic interaction between the ions. Figure 2.9 d reveals that the randomness in molten salt broadens the bands and also shifts them so as to have a distinct level of ϵ_+ (ϵ_-) energy in between. Comparing the two models shows that in the second one, there is no overlapping and there is still a wide gap in between bands. Based on the situation, either of these models can be used [64-66].

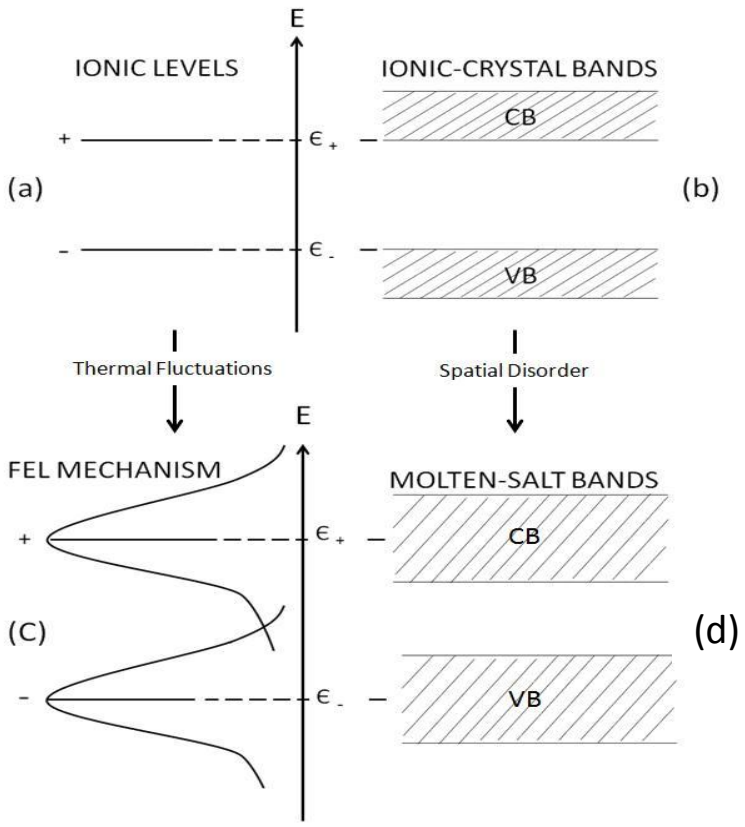

Figure 2.9 Frequency energy level mechanism (a, c) versus molten-salt model (b, d) [64].

2.12.1 Mechanism of electronic conductivity in ionic liquids

The electron-transfer mechanism in the ionic liquid is affected by the ionic atmosphere that surrounds the metal ions [67]. Any ions or molecules that bind to the metal ions form a coordination complex known as a ligand. The reactivity of the central metal ions is influenced by these ligands [68]. Generally, there are two types of electron-transfer mechanisms, e.g. outer-sphere and inner-sphere (or bridged). In the first

mechanism, the electron transfers between metal ions with no interruption in their first shell of the ionic atmosphere. In the second one, the electron transfers through the intermediate bridging ligand that links both metal ions [69].

The mechanism of electron-transfer can be simplified into the three following stages:

1- Optimum intermolecular distance between reactants is reached,

2- The Franck-Condon barrier condition is fulfilled,

3- The electron transfers

The electron transfer occurs when the reactants are close enough to each other. In case of having one or more uncharged species, the optimum distance is reached by a diffusion mechanism. However, in most cases, we are dealing with pairs of charged species with the same sign. Therefore, the electrostatic repulsion determines the minimum distance between the same charged species [67].

Based on the Franck-Condon principle, it is impossible for a molecule to have a new configuration within the electron-transfer occurrence. Physically, this is because the fast movement of the electrons does not allow the molecules enough time for a new configuration. Different configurations of ionic compounds act as barriers to electron transfer; therefore, direct electron transfer between ionic compounds, while they are in their equilibrium states, needs electronic activation energy to overcome this barrier. However, there is an indirect way in which the electron can transfer without such

barriers. By using the internal vibrational energy, the two ionic compound configurations can become symmetrical and have an intermediate configuration in between their equilibrium configurations. In this rearrangement, the degree of mismatch between the ligands of the two ionic compounds decreases and as the vibrational energy which is also known as Franck-Condon rearrangement energy is less than the electronic activation energy, the indirect electron-transfer is more probable to happen [67].

Evidently, the Franck-Condon barrier becomes important only when we deal with species that have high mismatch in their molecular configuration. This is usually observed in aqueous systems [67, 70-71].

As mentioned before, the electron transfer can take place either through an outer sphere or inner sphere mechanism. However, the electron transfer between metal ions is more probable through an intervening molecule or ligand (inner sphere mechanism). The electrons of a metal ion are delocalized on to the bridging ligands [64, 72], and if the complexes contain unsaturated ligands [64], this can facilitate the electron transfer.

2.12.2 Electronic conductivity in metal-metal halide melts

The conductivity behavior of Bi-$BiCl_3$ [73-74] and Cd-$CdCl_2$ [73, 75] systems in the salt region are different from the conductivity of Bi-BiI_3 [73]. Increasing the amount of metal in salt region of the Bi-$BiCl_3$ and the Cd-$CdCl_3$ systems decreases the conductivity.

However, Bi-BiI_3 system behaves like alkali-alkali halide [76-77], the Ce-$CeCl_3$ [78], and the Sr-$SrCl_2$ [79] systems in which the specific conductivities increase with increasing metal composition. Grantham et al. [73] assumed that polymeric configurations of atoms or ions in Bi-$BiCl_3$ and Cd-$CdCl_2$ systems present some difficulties in the electron transfer in comparison with Bi-BiI_3 system.

In fact, adding bismuth metal to the salt changes the conductivity mechanism to an electronic one. In case of adding high amounts of bismuth metal, the conductivity behavior is similar to those metals containing scattering ionic sites [65, 73]. However, in the salt rich region of Bi-BiI_3 mixtures (0-50 mole % Bi), the conductivity pattern is consistent with the electronic conduction in ionic liquids that was discussed in the previous section. In addition, adding 10-50 mole % Bi provides a very large amount of charge carriers (10^{21}-10^{22} cm^{-3}), and therefore, one expects a high electronic conductivity in the metallic range. However, the moderate amount of conductivity is attributed to the low mobility of electrons during the jumping process [65].

Generally, the activation energy for conduction can be determined from an Arrhenius-type plot of the specific conductivity measurements close to the melting point of the mixtures. Using the activation energy values, one can determine the conduction type (ionic or semiconductor) or the nature of molten salts (ionic or molecular). Table 2.1 shows the activation energy values for different types of molten salts and conduction mechanisms [80].

The activation energy of the Bi-BiI_3 conductivity increased with the amount of metal to approximately 84 kJ/mole at 40 mole % Bi, which based on the above explanation, put this system into the semiconducting molten metal salt category [80]. The conductivity values for semiconducting molten metal salts are usually higher than 100 $\Omega^{-1}cm^{-1}$ [80] and it is in consistent with the values of the Bi-BiI_3 system conductivity [73].

Table 2.1 Activation energy for conductivity of different types of molten salts [80].

Molten salt type	Activation energy (KJ/mole)	Example
Molten ionic salts	8.4- 12.6	Alkali halides
Molecular liquids	25.12- 29.3	H_2O, $AlCl_3$, $HgCl_2$
Semiconducting molten metal salts	~ 84	Bi-BiI_3

Grantham [80], measured the conductivity of mercuric-mercurous chloride and mercuric-mercurous iodide systems. The activation energy of the $HgCl_2$-Hg_2Cl_2 system dropped from 29.3 kJ/mol for $HgCl_2$ to 16.75 kJ/mol for Hg_2Cl_2. This can indicate the transition from covalent $HgCl_2$ to ionic Hg_2Cl_2. Moreover, the activation energy of HgI_2-Hg_2I_2 increased with temperature but never exceeded the 8.4- 12.6 kJ/mol which keeps them in the ionic salt category.

2.13 Electrical measurements of electrolytes

2.13.1 Ionic conductivity measurement techniques

Electrical conductivity measurements consist of the application of a voltage across a cell containing an electrolyte. The electrolyte can be either liquid or solid and the voltage may be either constant or fluctuate in a controlled manner. The response current that is passing through the cell and the electrolyte is then measured. It is also possible to apply a constant or variable current through the cell and determine the resultant voltage. Therefore, the electrical conductivity of an electrolyte can be measured using the following two techniques:

1- Direct current (DC) measurements

2- Alternating current (AC) measurements

2.13.1.1 Direct current measurements

One of the most straightforward methods to measure the ionic conductivity of electrolytes is direct current techniques. In this method the electrolyte is located between two non-blocking electrodes and then on the application of a stable dc voltage, a constant current passes through the circuit and the cell. Due to the electric field, the ions migrate within the electrolyte and produce a constant current between electrodes [81].

In electrochemistry, the electrical behavior of a given cell is represented by an equivalent electrical circuit, for instance, the resistance to the ions migration within the electrolyte can be represented by a resistor. The applied potential, V, and the current, I, through the cell is measured and the resistance of the electrolyte (R_b) can be calculated from Ohm's law, $R_b=\frac{V}{I}$ [82].The resistance value is highly dependent on the dimensions of the cell and the electrolyte within it; therefore, the other term known as resistivity which is an intrinsic property of a material is defined as follows:

$$\rho = \frac{R_b A}{l} \qquad (2.24)$$

In this equation, ρ is the resistivity of the material, l is the distance between the electrodes and A is the area [82].

Although this method seems straightforward, we should consider the effect of the electrode/electrolyte interface. When the current is passing through the cell, it also flows across the electrode/electrolyte interface. The flow of the current through the interface is controlled by the electrode reaction rate and therefore, this impedance to the current flow is shown by a resistor, R_e, in an electrical circuit.

Generally, the necessary condition for using a simple two terminal measurement is fulfilled when R_e is quite negligible in comparison with R_b. However, this is not always the case. In this regard, a new set up is designed in which another two electrodes are added. The four electrode cell is capable of eliminating the influence of the electrode/electrolyte interface on the measurements and can determine the electrolyte

conductivity directly. Another advantage of the four-terminal dc measurement is its simplicity and that it requires inexpensive equipment. However, constructing four terminal cells is more difficult than two terminal cells. Furthermore, it is difficult to find completely reversible electrodes that remain stable over a wide temperature range. Therefore, due to above disadvantages, there is a tendency to determine the electrolyte conductivities by ac techniques [81].

2.13.1.2 Alternating current measurements

One of the most popular methods to determine electrical properties of materials is the alternating current method. In this technique, a very simple cell equipped with inert ionically blocking electrodes is capable of determining the bulk electrolyte properties as well as polarisation phenomena occurring within the cell. However, the equipment required and the theory behind the interpretation of measurements is very complicated compared with the dc method [81].

In an ac experiment, an alternate voltage is applied to a conductance cell and as a result of this perturbation, an alternate current that passed through the cell is measured. Therefore, two parameters relate the current to the applied potential. One is the resistance to the flow of charge which is defined through Ohm's law, $(\frac{V_{max}}{I_{max}})$, and the other is the difference between the voltage and current phase, Θ (Figure 2.10). The combination of the magnitude, $\left(\frac{V_{max}}{I_{max}}\right)$, and the phase angle, Θ, represents the

impedance (Z) of the electrochemical cell which is a function of the applied frequency [81].

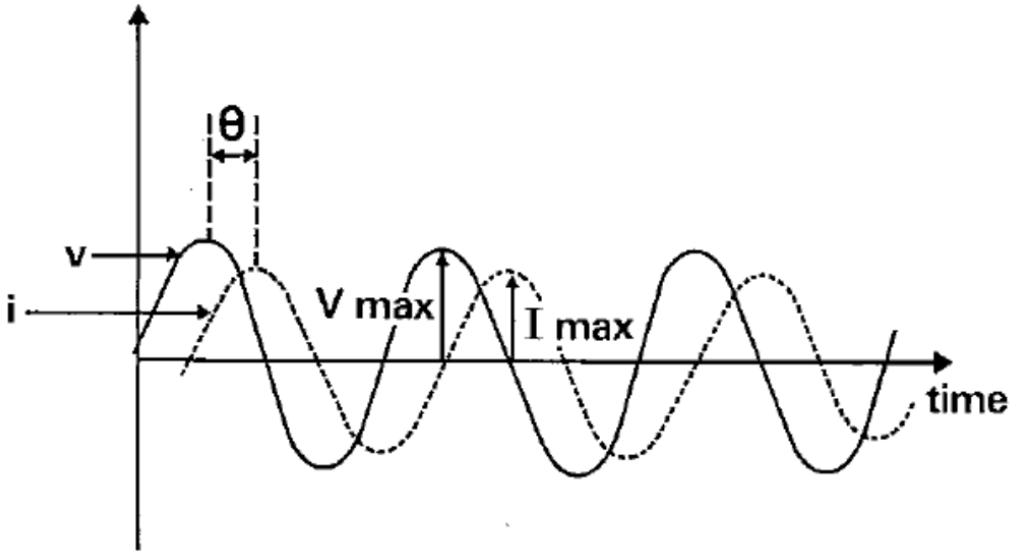

Figure 2.10 The sinusoidal voltage and current at a given frequency [81].

Therefore, the impedance of the cell can be shown as a point in a vector diagram (Figure 2.11) [81]. The distance of the point from the origin and the angle between the vector and the x-axis represent the magnitude and the phase difference between the current and the voltage, respectively. In fact the impedance (Z) can be shown by real (Z') and imaginary (Z") parts of a complex number, i.e.,

$$Z = Z' - iZ'' \quad (2.25)$$

where i is the complex number operator, $\sqrt{-1}$.

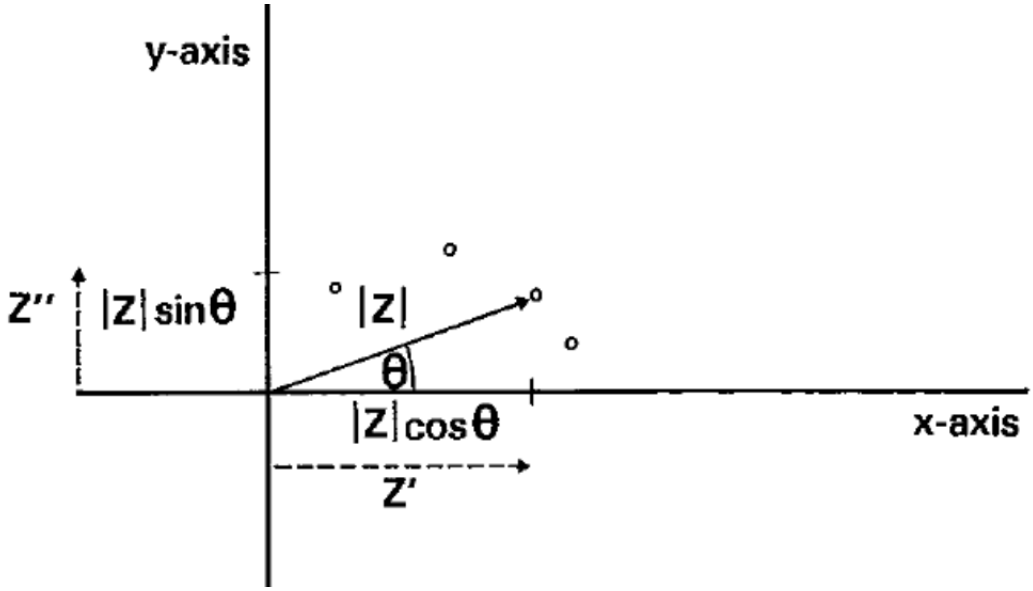

Figure 2.11 The impedance, Z, of a cell on a vector diagram. Z' and Z'' are the real and imaginary components of the impedance, respectively [81].

2.13.1.2.1 Electrochemical impedance spectroscopy technique (EIS)

Generally, when the electric field is applied to the electrolyte, the ionic species move through the electrolyte and accumulate at barriers such as the solid electrodes. Due to this polarization, the ionic current drops to zero after a while. To avoid the polarization the electrolyte should be subjected to time-dependent currents [70]. Therefore, measuring the impedance of a given electrolyte as a function of frequency over a wide range of frequency, typically 1 mHz to 1 MHz, can help us to interpret various electrical properties of the cell [81].

As just mentioned, the impedance of the cell components can be represented by complex numbers. In the EIS method, the complex impedance of the cell is determined

as a function of frequency and the results are shown as a Nyquist plot or complex impedance plot. The Nyquist plot can be interpreted by finding a suitable equivalent electrical circuit that closely represents the individual components of the cell. For example, capacitors and resistors can model polarisation and charge migration within the cell, respectively. Figure 2.12 shows the common Nyquist plot and its equivalent electrical circuit [81].

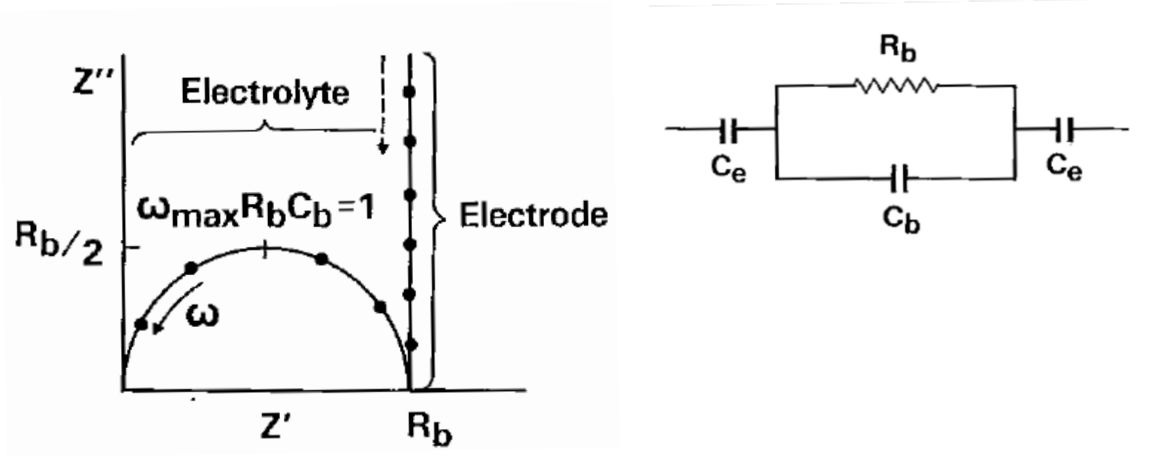

Figure 2.12 Common impedance plot and its equivalent circuit [81].

2.13.1.2.1.2 Experimental considerations

There are some experimental parameters such as frequency range and potential amplitude that are influenced by both the material under study and the equipment capabilities. In order to maximize the amount of information that is extracted from the impedance plot and to minimize the possible errors, special considerations should be applied to choosing a frequency range and potential amplitude. For instance, the

measured frequency range should cover both sufficiently large and small values in a way that the imaginary part of the impedance inclines toward zero. Although the instrument limitations usually define the frequency range especially for high frequencies, it is important to select a frequency range that can represent the behavior of the system appropriately [83].

The optimum potential amplitude depends on the polarization curve of the system under study which shows the linearity of that system. Applying high amplitude potential helps to minimize the level of noise in impedance response. However, using low amplitude potential minimizes the non-linearity. Therefore, there is a compromise between choosing the level of potential amplitude. For example, in the case of a system with a linear current-voltage curve, a potential with high amplitude can be applied [83].

2.13.2 Electronic conductivity measurements technique

2.13.2.1 DC measurements

In order to measure the electronic conductivity of an electrolyte, a dc technique can be used. In this method, the electrolyte is fixed between two ionically blocking electrodes and a constant voltage is applied across the cell. The applying voltage should be below the thermodynamically expected decomposition voltage. The resulting current for each voltage is then measured and a graph of voltage versus current is plotted. Based on Ohm's law, the bulk electrolyte resistance can be measured from the slope of

this curve. As the electrodes are not participating in the reaction ionically, the electrical current is due only to the transport of electrons and holes [24, 81, 84].

2.14 Conductivity measurement techniques

There are several techniques that have been used to determine electrical conductivity of different materials. In general, these techniques can be divided into two groups; low accuracy technique and high accuracy technique.

- Low accuracy technique:

Two-wire, four-wire, crucible, ring, and two toroid techniques are different methods of measuring electrical conductivity. In all the above methods, the current is not limited between electrodes and spreads out in different directions which causes a lack of accuracy in cell constant measurements.

- High accuracy technique:

There are four high accuracy designs that can be used in measuring electrical conductivities of materials; 1- meandering winding, 2- interdigitated, 3- coaxial cylinders, and 4- capillary design. Figure 2.13 shows the schematic design of the above techniques [85].

The capillary design itself is also classified into the following two designs:

1- The U-shaped capillary design which contains liquid inside and two electrodes.

2- The dip-type capillary design which has either a single capillary or twin capillaries. The capillaries are soaked inside the liquid; therefore, the outside surface of the cell is in direct contact with the melt [86].

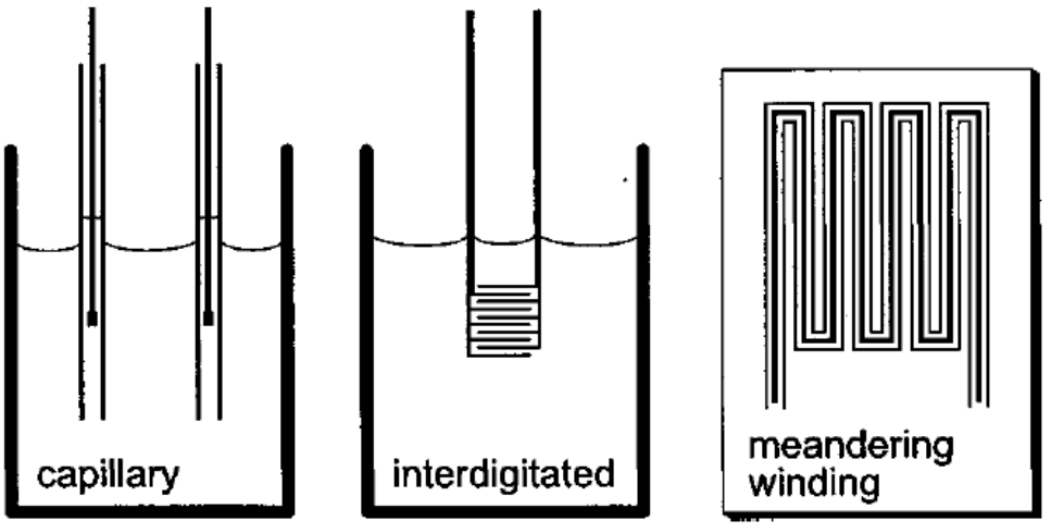

Figure 2. 13 Schematic design of the high accuracy technique for measuring electrical conductivity [85].

Moreover, there are three factors that should be considered before choosing the best design. The factors are:

1- the range limits available to the impedance measuring instruments;

2- the chemical compatibility between the cell materials and the materials under investigation;

3- the conductivity of the material under investigation [85].

For instance, there is a possibility of parasitic conductance during measurements using a dip-type capillary design. In general, the conductivity of quartz at high temperatures (1000˚C) is insignificant; however, in the case of using the dip-type capillary design where the outer surface of the quartz cell is in direct contact with molten salts (different ions, i.e. Na^+, K^+, Li^+), diffusion can occur and parasitic conductance can be seen. Comparing conductivity values obtained from two different cell designs (U-shaped and dip-type capillary design) confirms the presence of parasitic conductance in the dip-type capillary design at high temperatures [45].

Furthermore, some characteristics of molten salts such as high volatility and corrosiveness constrain the conductance cell construction and design. In addition, molten salts have large conductivities, falling in the range of 1-5 $S \cdot cm^{-1}$ for alkali halides near their melting points [87]; therefore, capillary cell design with high cell constant of at least 200 cm^{-1} is suggested by different investigators [45, 85, 87-88], while for low conductive liquids, the interdigitated electrode design with relatively short current paths is suitable [85].

2.14.1 Conductance cell calibration

Kohlrausch in 1898 reported the first calibration quality data set for aqueous KCl solutions in the normality scale [89-90]. Parker et al. determined the absolute

conductance of the "kohlrausch standard" in the demal concentration scale [90-91]. 1 demal is an absolute unit of concentration in chemistry which is equal to 1.000028 molar. 1 demal is equal to the concentration of a solution in which 1 mole of solute is dissolved in 1 cubic decimeter of solvent. The data set that has been generally accepted today as the reference for conductance cell calibration was established by Jones and Bradshaw in 1933 [90, 92].

The Jones and Bradshaw values are given in following table.

Table 2.2 Conductivity of three different concentrations of aqueous KCl solution in three different temperatures [90, 92].

KCl concentration (demality) / Temperature	σ (S. cm^{-1})		
	0˚C	18˚C	25˚C
1	0.06517	0.09783	0.1113
0.1	0.007137	0.011166	0.012856
0.01	0.0007736	0.0012205	0.0014087

There were several investigations to determine the cell constants of molten salts at "working temperature" [90, 93-94]. In this regard, a variety of molten salts such as $NaNO_3$, KCl, and NaCl, etc., were used as high temperature calibrants. However, the results were not consistent with each other especially at high temperatures. The

conductance cell configuration also has an effect on the discrepancy of results. The presence of stray capacitance shunts, in capillary dip cells at high temperatures is responsible for resultant deviations between different experiments [86]. Therefore, the calibration of molten salt conductance cells can be done using aqueous KCl demal values and consideration given to the thermal expansion of cell materials at high temperatures. For capillary design, as the diameter is small compared to the length, the linear expansion of the material can be considered which is around 0.5 x 10^{-6}°C^{-1} for quartz. Therefore, the thermal expansivity corrections for quartz and Pyrex cells between 300-1000˚C are 0.05% and 0.1-0.2 %, respectively. These values are quite negligible for most practical purposes [90].

3. RESEARCH OBJECTIVES

In spite of all the improvements in ZEBRA technology, intermittent degradation persists which limits the long term operation of ZEBRA cells. The graph in Figure 3.1 shows the change of cell voltage versus number of cycles for 10 cells in series. The lower plot shows cells that were cycled to 80% depth of discharge, whereas the upper one shows those which were cycled to 70% depth of discharge. It is apparent that increasing depth of discharge leads to shorter life (degradation after 300 cycles).

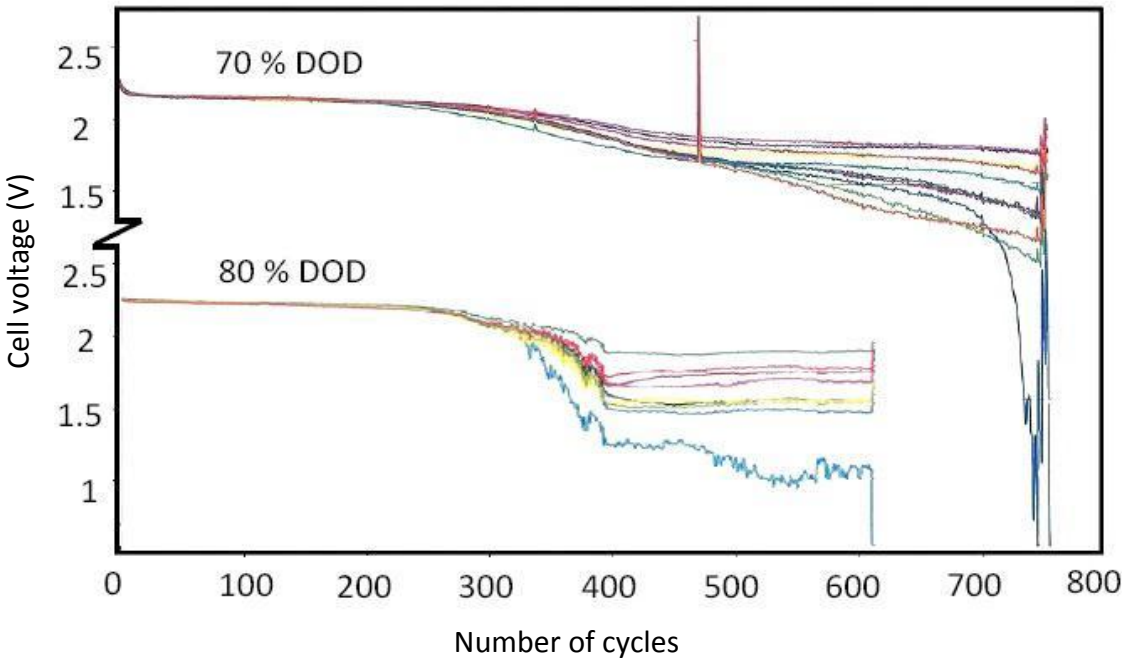

Figure 3.1 Effect of DoD percentage on cell voltage in high number of cycles.

As shown in Figure 2.4, the decrease in cell voltage can be related to increasing cell resistance with depth of discharge. The major part of this increased resistance is attributed to the positive electrode; therefore, one of the principle objectives of this project was to identify the microstructural changes of the cathode during high number of cycles and at various stages of discharge to determine its relation to cell degradation.

Microstructural investigations reveal the presence of isolated Ni particles which are not active in the cell reaction since they are surrounded with phases that are only ionic conductor. Consequently, another objective of this research was to make the intact Ni particles to participate into the reaction by having a mixed ionic-electronic conductive electrolyte. Therefore, the effect of additives on the conductivity of the liquid electrolyte, particularly with respect to mixed ionic-electronic conduction was studied.

In the ZEBRA cell chemistry, several additives are added to improve capacity, energy density, and power density. However, their effect on conductivity of the liquid electrolyte has not been reported. Therefore, the objective was to determine the effect of some of these additives on the conductivity of the liquid electrolyte ($NaAlCl_4$).

4. EXPERIMENTAL METHOD

Experiments were focused on two major areas: 1) analysis of the microstructure at different positions within the ZEBRA cathode and at different cycle life, 2) analysis of the electrical conductivity of the liquid electrolyte to determine the effect of different additives.

Moreover, thermodynamic modeling was conducted to identify the phases as a function of temperature and depth of discharge during different cycling programs. The FactSage software and database provide useful tools for modeling ZEBRA cathode chemistry. It also helps to identify the possible stable phases when various additives were added to the liquid electrolyte.

4.1 Cycling program of as received ZEBRA cells

Microstructural investigation of the $Na/NiCl_2$ cathode was carried out on three cells with three different numbers of cycles. All cells were charged at a constant current of 10 A until 2.67 V was reached and then maintained at this voltage until the current dropped to 0.5 A. Subsequently, each cell was discharged by 26.6 Ah (70% depth of discharge or DoD) or 38 Ah (100% DoD) at 295˚C and then examined at the end of their discharge cycle. In order to investigate the microstructure of the cathode in the charged state, one of the cells with 100% DoD was recharged completely. All cells were supplied

by Fiamm SoNick Company, Stabio, Switzerland. Table 4.1, 4.2, and 4.3 show the cycling program of these cells.

Table 4.1 Cycling program of cell with one cycle, C1.

Name	Number of Cycles	Cycling program
C1	1	Charge 2.75A to 48.3 Ah, 325˚C - Discharge 12A to 40.8 Ah 295˚C

Table 4.2 Cycling program of cell with three cycles, C3.

Name	Number of Cycles	Cycling program
C3	3	Charge 2.75A to 48.3 Ah, 325˚C - Discharge 12A to 40.8 Ah 295˚C
		Charge 10A to 2.67V to 0.5A, 295˚C – Discharge 19 A to 38 Ah 295˚C
		Charge 10A to 2.67V to 0.5A, 295˚C – Discharge 19A to 38 Ah 295˚C

Table 4.3 Cycling program of cell with 763 numbers of cycles, C763.

Name	Number of Cycles	Cycling program
C763	1	Charge 2.75A to 48.3 Ah, 325˚C – Discharge 19A to 40.8 Ah, 295˚C
	11 (cycle 2-12)	Charge 10A to 2.67V to 0.5A, 295˚C – Discharge 19 A to 38 Ah 295˚C
	751 (cycle 13-763)	Charge 10A to 2.67V to 0.5A, 295˚C – Discharge to 26.6 Ah, 295˚C

The number in front of the cells name indicates the number of cycles they have gone through. For example, C763 refers to cell which has undergone 763 cycles.

All the cells are loaded in discharged state; therefore, the formation of charged species during first cycle is guaranteed by having them charged at higher temperature and higher capacity. Moreover, the nickel backbone structure forms during the first 10 to 12 cycles [20].

4.2 Sample preparation

As most components of the ZEBRA cell are hygroscopic materials, all sample preparations were carried out inside an argon atmosphere glove box used for handling liquid sodium metal. The purity of the glove box atmosphere was less than 2 ppm oxygen.

The steel case and wicks were removed inside the glove box followed by the sodium metal. Figure 4.1 and 4.2 show the cell before and after opening, respectively. The black color of the surface of the β”- Alumina is due to a thin layer of carbon which is used to wet the surface of the ceramic electrolyte. The cross section of the cell is shown in Figure 4.3. After breaking the ceramic electrolyte tube, different sections of the cathode were obtained by using a hacksaw. The rough surface of the samples was then polished using different grades of SiC polishing paper for examination by SEM. The

residue on the surface resulting from dry polishing was removed by high pressure argon gas.

Figure 4.4 shows the cathode compartment of the ZEBRA cell after the ceramic electrolyte is removed.

The SEM samples were fixed on appropriate stubs using carbon tape and silver paste. Covering the edge of samples with silver paste prevents charge accumulation and therefore, there is no need to coat samples with conductive materials. After preparation, all samples were stored in a desiccator inside the argon atmosphere glove box.

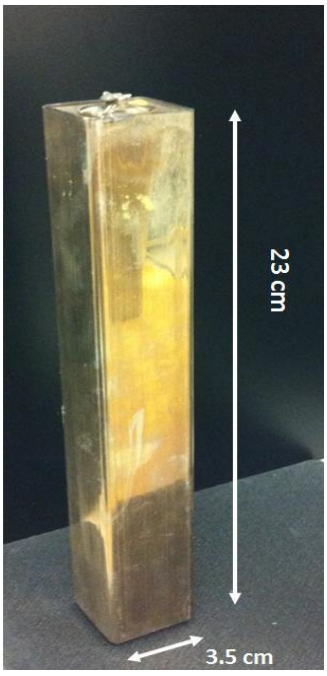

Figure 4.1 ZEBRA cell before opening.

Figure 4.2 ZEBRA cell after opening.

Figure 4.3 Clover leaf shape of the cross section.

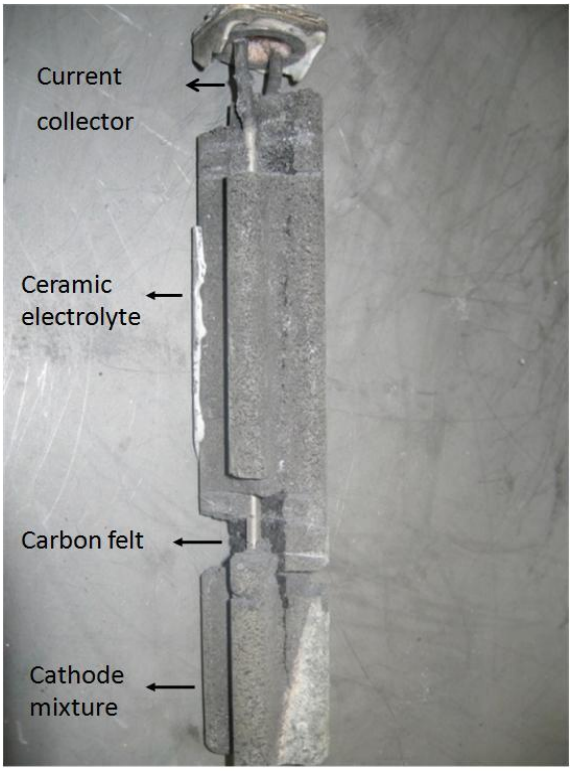

Figure 4.4 Different parts of the ZEBRA cell with ceramic electrolyte removed.

4.2.1 Vacuum distillation technique

SEM micrographs of the cathode from the as opened cell could not be clearly resolved as the frozen $NaAlCl_4$ covered features of the microstructures. To overcome this, a vacuum distillation technique was used to remove some of the liquid electrolyte and bring out the phases distinctly.

In this technique, after the steel case, wicks, and sodium metal were removed, the top part of the electrolyte tube was cut off and the cell was positioned upside-down in a vacuum furnace inside the glove box. Then the cell was heated for 4 hours at 450˚C. This procedure removed some of the liquid electrolyte by both liquid drainage and evaporation and exposed more features of the cathode microstructure.

4.3 Analysis of the cathode microstructure

The microstructure of the cathode has been studied using scanning electron microscopy (SEM), focused ion beam (FIB), energy dispersive spectroscopy (EDS), and X-ray diffraction (XRD). Moreover, the nickel particle size was measured using Image analysis. The following sections explain each in detail.

4.3.1 Scanning electron microscopy and energy dispersive x-ray analysis of the cathode microstructure

Scanning electron microscopy (SEM) was performed using a JEOL 7000F field emission SEM. The accelerating voltage was usually set as 10-15 Kv. The SEM micrographs were taken from following sections:

1- The surface of the cathode before vacuum distillation technique is conducted.
2- The surface of the cathode after vacuum distillation technique is conducted.
3- The surface of the cathode in contact with the ceramic electrolyte.
4- The horizontal cross section of the cathode to reveal variations in composition across its diameter.
5- The vertical cross section of the cathode to reveal variations in composition along its length.
6- The cathode of the cell in charged state.

The SEM is equipped with energy dispersive spectroscopy; therefore, the elemental analysis of the samples was done by EDS.

4.3.2 Focused ion beam analysis of the cathode microstructure

The cross section of the cathode in different stages of cycling was studied using a ZEISS NVision 40, FIB/FE-SEM. In this procedure, a protective layer of graphite was

deposited on the surface of the sample, and then the cathode was initially milled with a 30 kV: 13 nA probe of gallium ions. Finally, the surface was cleaned with a 30 KV: 3 nA probe to smooth out the surface. The FIB device is equipped with SEM. Therefore, the subsurface is revealed through back scatter mode of the SEM.

4.3.3 X-Ray diffraction

Phase analysis was carried out using Bruker D8 Advance, X-ray diffraction with Cu $k_{\alpha 1}$. All samples were prepared inside the glove box and were handled in a desiccator. The XRD analysis was performed immediately after preparation to minimize exposure to air.

4.3.4 Image analysis

The size of the Ni particles was measured all around the cathode using Clemex Image Analysis.

4.3.5 In-situ SEM analysis of the cathode microstructure

In all of the above techniques, the microstructure of the cathode was studied at room temperature, but the ZEBRA cell works at high temperature (300˚C). In this regard, in-situ SEM analysis was attempted in order to investigate the mechanism of cycling and microstructural evolution.

The in-situ investigation was performed at Hydro Quebec Canada by using vacuum scanning electron microscope. The SEM was equipped with a small furnace attached to the bottom of the sample holder inside the vacuum chamber. The size of the chamber was 2.5 X 2.5 cm (Figure 4.5).

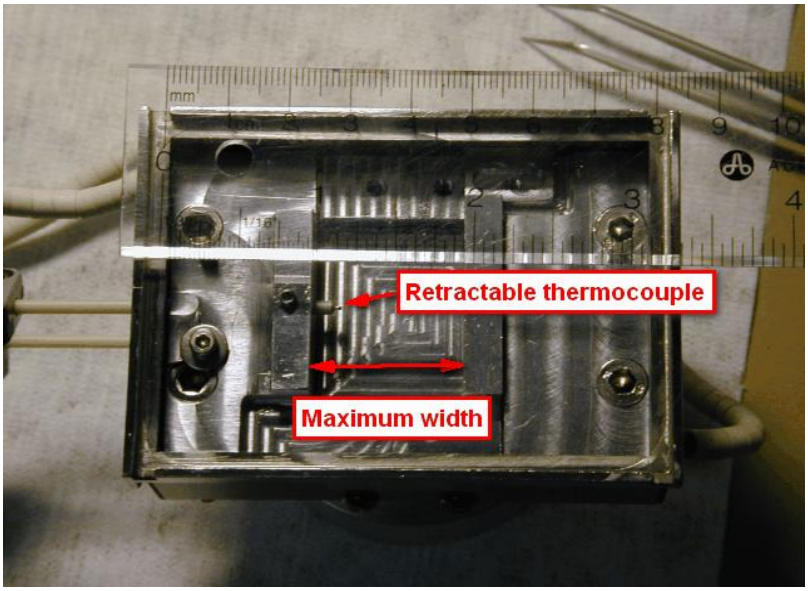

Figure 4.5 In-situ SEM sample holder.

4.3.5.1 Cell design for in-situ SEM analysis

In order to use the in-situ SEM, a special cell was designed, compatible with the working conditions of the SEM. Figure 4.6 shows a schematic view of the cell comprising two containers which are sealed to an α-alumina lid. The inner container is made of β”-alumina and acts as a ceramic electrolyte, while the outer container is made of

α-alumina and contains sodium metal. The upper part of the positive electrode is left open to permit electron travel between cathode and detector. The size of the whole cell had to be less than 2.5X 2.5X 2.5 cm to fit in the microscope. The anode was metallic sodium and the cathode was a mixture of NaCl, Ni, and $NaAlCl_4$. In order to ensure electronic conductivity inside the cathode, Ni mesh was also added.

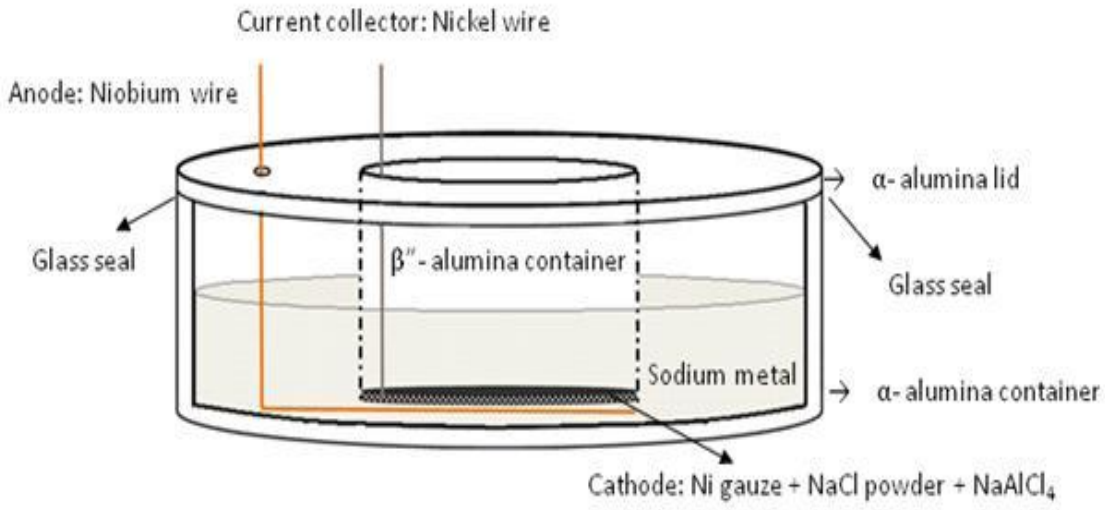

Figure 4.6 Schematic view of the in-situ SEM cell.

Figure 4.7 shows the components of the cell. In order to make the β"-alumina electrolyte, slip casting method was used. The slip was made by mixing 40:60 weight ratio of powder: water and ball milling for 24 hours. The slip was poured into a plaster mould and held until the thickness of the tube wall reached approximately 1 mm. The excess slip was then poured out. In order to prevent sodium loss, the sintering process

was carried out in a buffer mixture made of β-alumina and 2 wt. % Na_2CO_3. The samples were heated to 1650˚C at a rate of 5˚C/min and kept at this temperature for 30 minutes then cooled and homogenized at 1475˚C for 45 minutes [95].

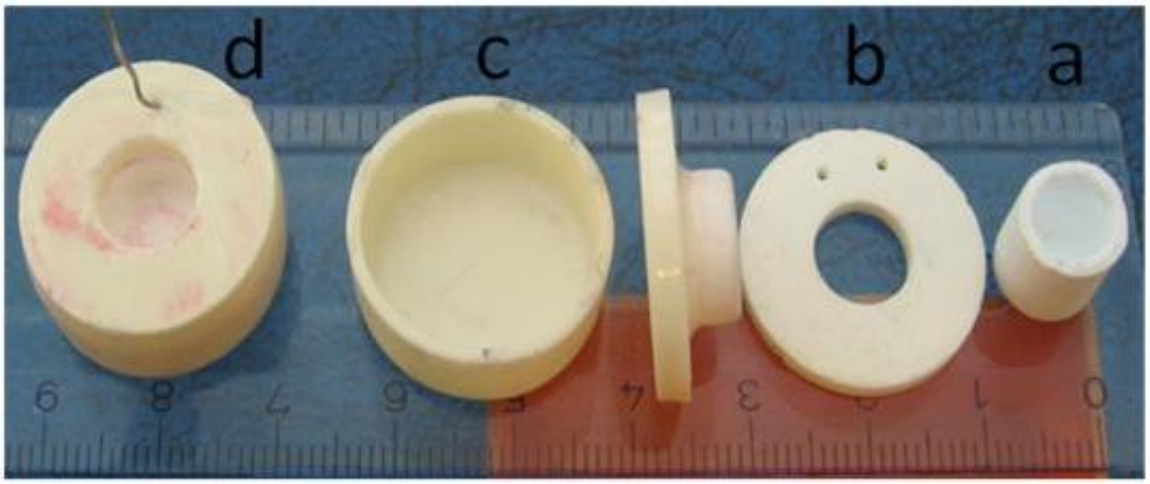

Figure 4.7 Different components of the in-situ SEM cell, a) β”-alumina, b) α-alumina lid, c) α-alumina container, d) fully assembled cell.

The α-alumina lid was made by pressing α-alumina powder + 5 wt. % ethylene glycol mixture and sintered in two steps. After pressing, the disk was pre-sintered at 1200˚C for 2 hours. This step makes the α-alumina disk sufficiently rigid for drilling. After drilling the holes, the disk was completely sintered at 1550˚C for 2 hours.

The β”- alumina tube was joined to α-alumina lid using a glass seal. The glass seal is the mixture of aluminosilicate glass frit and 40 wt. % printing oil which forms a viscous paste. After applying the glass paste, the assembly were heated to 1350˚C for 30 minutes and then annealed at 700˚C for 1 hour.

A high temperature resin (Duralco 4703) was used to seal the α- alumina lid to α- alumina container. Then the sodium metal was injected through the drilled hole with a syringe inside the glovebox.

Figure 4.8 shows the loaded cell fixed inside the SEM sample holder. The SEM micrographs in Figure 4.9 show liquid $NaAlCl_4$ (A), Ni particles (B), Ni gauze (C), and NaCl (D) at 300˚C. Unfortunately, the cell cycling experiment was not successful as the resistance of the cell was too high. The high resistance is hypothesized to be due to the small size of the cell and high evaporation of $NaAlCl_4$ inside the SEM chamber.

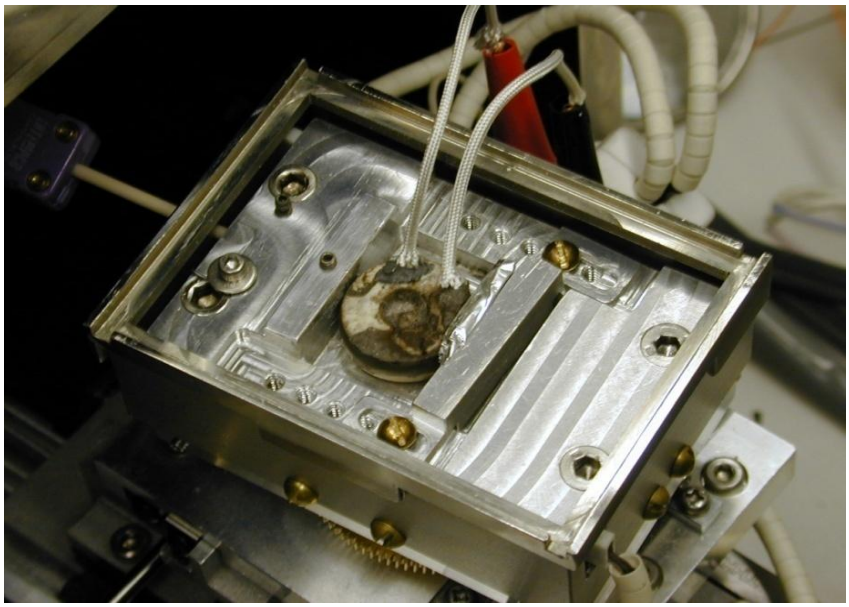

Figure 4.8 The loaded cell fixed inside the SEM sample holder.

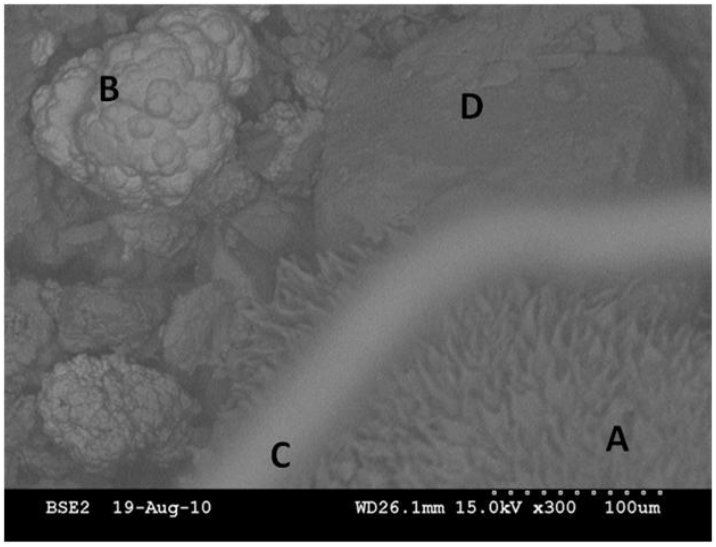

Figure 4.9 SEM micrograph of the cathode heated to the operating temperature of 300˚C. (A) Liquid $NaAlCl_4$, (B) Ni particles, (C) Ni gauze, and (D) NaCl crystals.

4-4 Analysis of the molten salts electrical conductivity at high temperatures

The electrical conductivity of $NaAlCl_4$ was measured at high temperature and the effect of different additives on its conductivity was examined. In order to measure the conductivity, a special cell had to be designed. Section 2.14 explained the considerations in conductance cell design. However, designing a conductance cell for measuring the conductivity of $NaAlCl_4$ at high temperatures is more complicated as it is a hygroscopic and volatile molten salt that is highly corrosive and has relatively high conductivity. Therefore, these properties constrain the conductance cell construction and design.

4-4-1 Conductivity cell design

Among various designs, the capillary U-shaped cell is the one that can provide a high cell constant. Moreover, the purpose of this research was to measure the conductivity at high temperatures; therefore, besides a cell with high constant, it must be an electrical insulator that can tolerate high temperatures and not react with $NaAlCl_4$. Therefore, among different materials, Pyrex and quartz were the best candidates.

In addition, another factor that should be considered during cell design is that the $NaAlCl_4$ is a volatile and hygroscopic material which means that the measurements must be done in a controlled atmosphere.

During conductivity measurements, the $NaAlCl_4$ should be placed between two ionically blocking electrodes and the electrode tips on both sides of the conductivity cells should be fixed at the same distance above the capillary tube openings. The best candidate for the electrode is tungsten which is not reactive with $NaAlCl_4$ and can be sealed to Pyrex glass which guarantees the construction of a closed volume cell. However, Pyrex has a limited temperature range and it has higher thermal expansion than quartz which makes it more prone to thermal shock. Therefore, quartz is the better candidate. There are some reports on sealing tungsten wire to quartz using a GSC#3 glass bead [51, 73, 96]; however, this type of glass is no longer available. As a result, considering all the above limitations led to a two part cell design in which, the capillary

U-shaped part (Figure 4.10) which goes inside the furnace is made from a thick walled quartz (2mm) and the two tungsten electrodes (1 mm diameter) were sealed off to Pyrex tubes with uranium glass. The Pyrex and quartz tubes were joined by O-ring clamps.

In order to protect the joint parts from breakage, two constrictions are made at the ends of the Pyrex tubes. These constrictions prevent the tungsten electrodes from tilting during cleaning the cell and reduce the amount of load that is applied to the sealing parts. They also constrain the tungsten electrode movement and keep them straight in the middle of the cell during experiment.

Figure 4.10 Capillary U-shaped quartz tube.

The quartz arms of the cell are around 30 cm long and 12 mm outer diameter. The two ends were connected with a cross-member above the U-shaped capillary. The inner diameter of this bridge is around 8 mm and it helps to equalize the pressure inside the capillary and to support limbs and prevent them from bending and breaking. The U-shaped capillary is approximately 6 cm long and the outer and inner diameters are 6 mm and 2 mm, respectively.

During the experiments, the U-shaped capillary tube was loaded with salt powders and then the two Pyrex tubes with tungsten electrodes attached joined to the quartz tube using O-rings clamps (Figure 4.11). It is important that the electrode tips on both sides of the conductivity cells be kept at the same distance above the capillary tube openings during measurements. Necessary provisions are also made in the design of the cell to enable its cleaning.

In addition, an inlet and outlet valve were also attached to the Pyrex limbs which provide conditions in which the cell can be worked outside of the controlled atmosphere of the glove box. In this case the cell can be loaded inside the glove box and evacuated and backfilled while it is outside of the glove box.

The temperature of the cell was measured using two calibrated chromel-alumel thermocouples which were attached to two sides of the U-shaped capillary tube. The schematic design of the cell is shown in Figure 4.12.

Figure 4.11 Conductance cell set up inside a glove box.

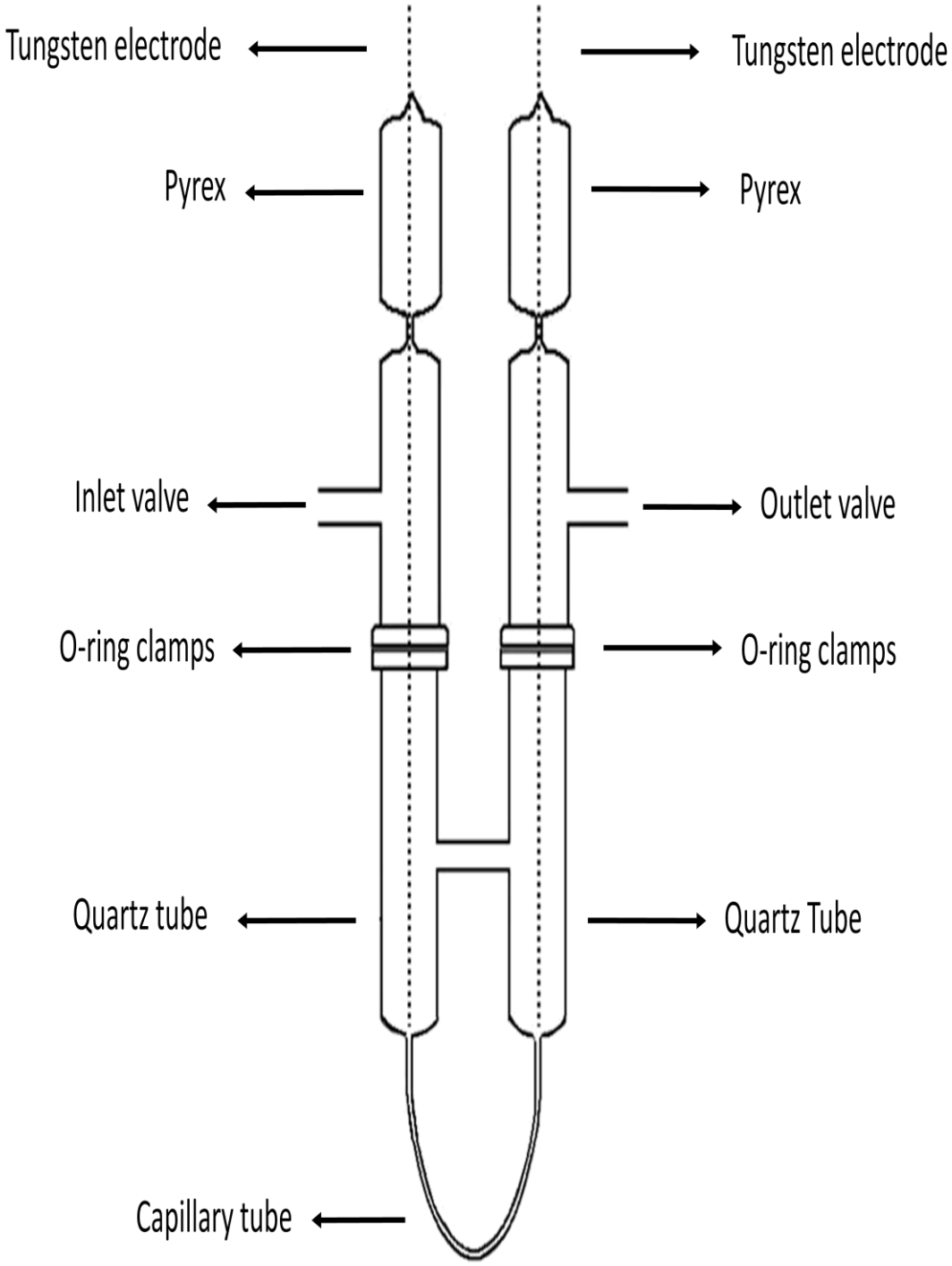

Figure 4.12 Schematic design of the conductance cell.

4-4-2 Conductance cell calibration

Calibration consists of measuring the cell resistance when the cell contains a liquid of known specific resistivity and then calculation using equation (2.15) to determine the cell constant ($\frac{L}{A}$).

The details of calibration are explained in Section 2.14.1. The Jones and Bradshaw data set [90, 92] has been used in the above conductance cell calibration.

The calibration was done at three different temperatures (0, 18, and 25˚C) and three different concentrations of aqueous KCl solutions (1, 0.1, and 0.01 demal). 1 demal is equal to the concentration of a solution in which 1 mole of solute is dissolved in 1 cubic decimeter of solvent.

The cell constant was near 400 cm^{-1} which is within the ranges that are suggested by other investigators [45, 85, 87-88].

4-4-3 Cell loading

$NaAlCl_4$, $NbCl_5$, Bi, Cu and Sn were used in conductivity measurements. These chemicals were initially weighed inside the glove box and mixed in different ratios.

During a typical experiment, the cell was loaded with the powder mixture inside the glove box and then the electrodes were placed in position and fixed with O-ring

clamps. Finally, the loaded cell was located vertically inside the resistance furnace well which is attached to the glove box. After the salts had melted, the cell was shaken manually to remove possible gas bubbles that adhere to the wall of the capillary tube.

4-4-4 EIS measurements

The conductance measurements were carried out with a frequency response analyzer (Model SI 1260) equipped with a potentiostat/galvanostat (Model EG&G 273) in the frequency range 1 Hz- 1 MHz.

In this experiment a sinusoidal voltage is applied to a cell and the sinusoidal current passing through the cell as a result of this perturbation is determined. In fact, by applying an alternating voltage within a wide frequency range, the impedance can be measured as a function of the frequency. The result can be represented by complex numbers and shown by Nyquist plot in the complex plane. In addition, the information about the different electrical properties of the cell can be extracted from this Nyquist plot. The details were explained in section 2.13.1.2.

All the conductivity measurements were made in the direction of both increasing and decreasing temperatures. Heating and cooling results were in good agreement with one another.

The conductivity of pure $NaAlCl_4$ has been measured from room temperature up to 500˚C. Moreover, the effect of adding different concentration of $NbCl_5$ on conductivity of pure $NaAlCl_4$ was studied.

In addition, various reducing agents (Cu, Sn, and Bi) were used to reduce the chlorine pressure of $NbCl_5$ in the molten salt mixtures and improve its conductivity. The conductivity of the mixtures was measured up to 500˚C.

4-4-5 DC measurement

The electronic portion of the total conductivity was measured using a dc polarization method. In this technique a potential bias (0-0.2 V) is applied with a potentiostat/galvanostat (Model EG&G 273) across the ionically blocking electrodes within 1 mV/s scan rate and the current between the two electrodes is measured at each potential. The electronic conductivity was determined for pure $NaAlCl_4$ as well as other mixtures at 300˚C.

4-5 Thermodynamic modeling of the cycling

FactSage is a thermochemic software which provides the appropriate database for ZEBRA battery chemistry. As the ZEBRA battery works at high temperatures, room temperature analysis may not reveal the phases present during operation and may contain artifacts. In this regard, the behavior of the ZEBRA cell has been modeled using

FactSage software. This modeling helps to predict any deviations that may occur at different points in the cycling program and also during sample preparation.

Furthermore, the effect of various additives (Cu, Sn, and Bi) on reducing the chlorine pressure of $NbCl_5$ in the mixtures was predicted by equilibrium graphs obtained from FactSage software.

5. RESULTS AND DISCUSSION

ZEBRA cathode consists of NaCl, Ni particles, and $NaAlCl_4$ in discharged state. The NaCl crystals are being replaced by $NiCl_2$ during charging. The microstructure of the all above phases was shown in this chapter. Moreover, the presence of Na_6FeCl_8 intermediate phase was also confirmed by XRD, SEM, and FIB. The micrographs were taken from the cathode of three different cells with three different numbers of cycles. One of each cell was provided by Fiamm SoNick Company in Stabio, Switzerland.

The cycling behavior of the ZEBRA cell at high temperature was also studied by FactSage software.

Finally, the electrical conductivity of the pure $NaAlCl_4$ was studied and the effect of additives on its conductivity was examined.

5.1 Electro optic analysis

The study of the cathode began by examination of the surface of the cathode in contact with the ceramic electrolyte without any pre-treatment (Figure 5.1). However, limited information could be obtained because the frozen $NaAlCl_4$ obscured the microstructure of other cathode components. To remedy this, a vacuum distillation technique was used. This technique removed some of the liquid electrolyte by both

liquid drainage and evaporation and exposed more features of the cathode microstructure. All phases are identified by contrast mode of back scatter electrons.

The SEM microstructure of the surface of the cathode in contact with ceramic electrolyte for cells C1, C3, and C763 is shown in Figure 5.2. The numbers in front of the cells name indicate the number of charge/discharge cycles. All three cells are in the discharged state and therefore, the discharged species such as cubic NaCl crystals (A) and Ni particles (B) as well as $NaAlCl_4$ electrolyte (C) are evident in the micrographs.

Moreover, the nickel backbone structure, which is the percolating network of Ni particles responsible for providing radial conductivity within the cathode, is shown in Figure 5.3. Figure 5.4 shows the lamellar structure of $NiCl_2$ crystals in a charged cell.

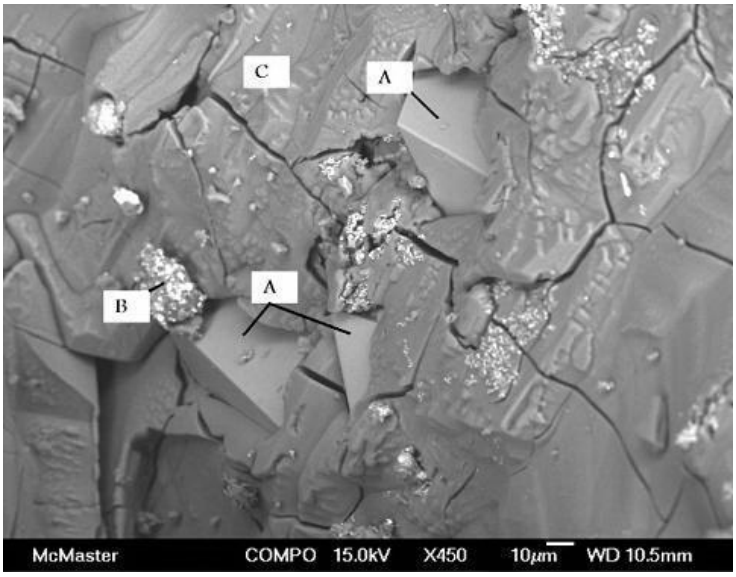

Figure 5.1 Microstructure of ZEBRA cathode with no pre-treatment. A, B, and C refer to NaCl, Ni and $NaAlCl_4$, respectively.

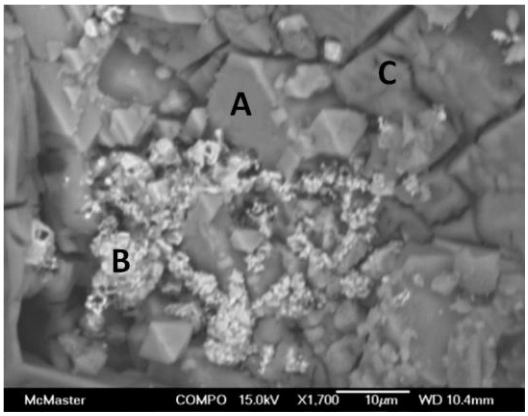

(a)

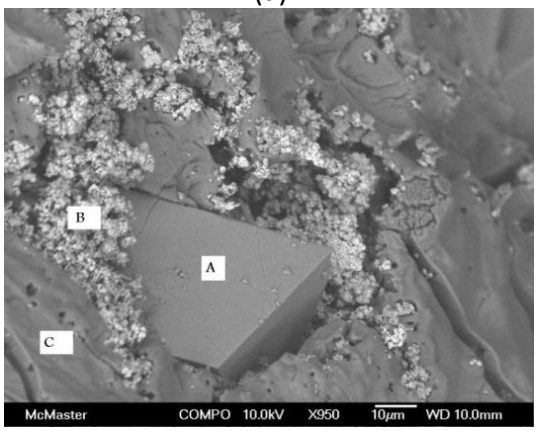

(b)

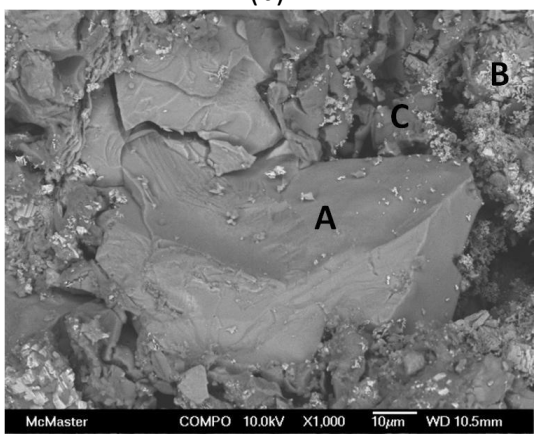

(c)

Figure 5.2 NaCl (A), Ni (B), and $NaAlCl_4$(C) phases in C1 (a), C3 (b), and C763 (c) after vacuum distillation. The sample number indicates the number of charge/discharge cycles.

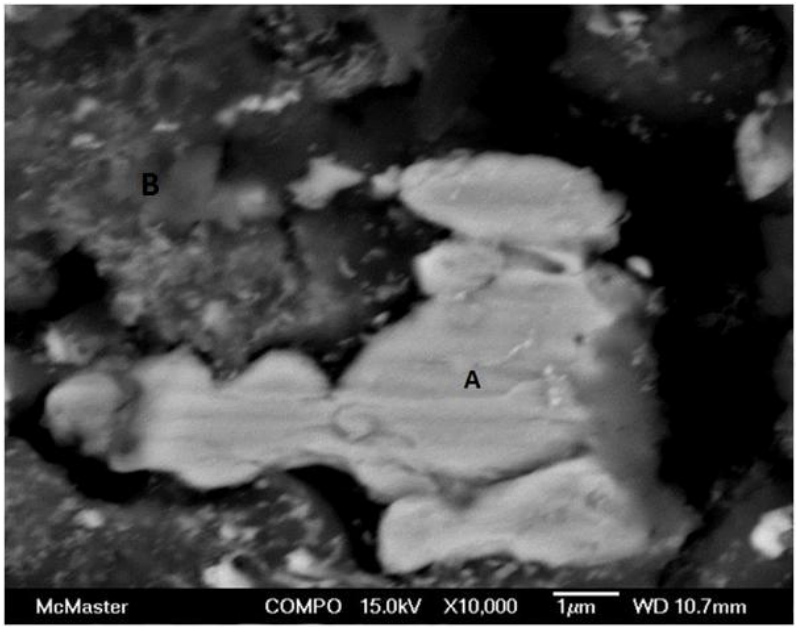

Figure 5. 3 Ni backbone (A) and $NaAlCl_4$ (B) in the cathode of C3 cell.

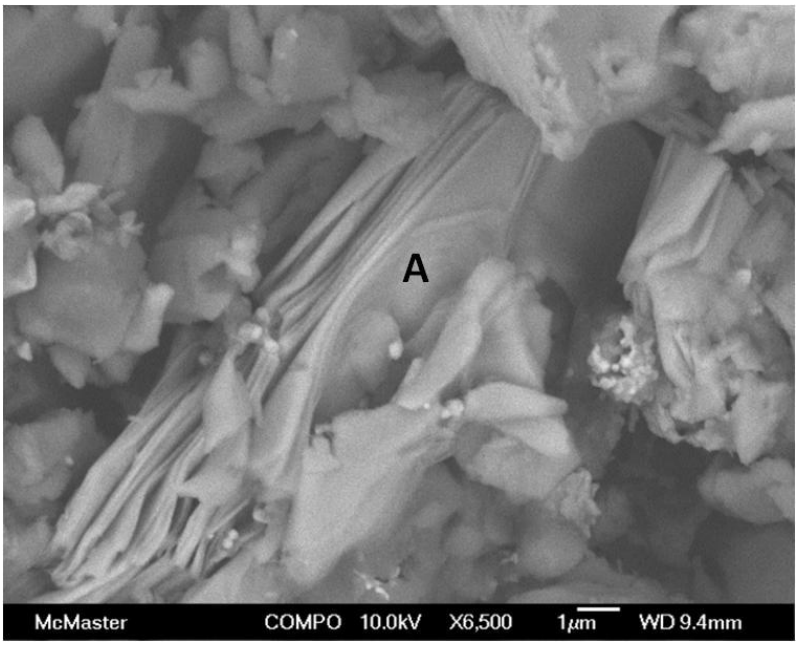

Figure 5. 4 Lamellar structure of $NiCl_2$ crystals (A) in charged cell.

In addition to above phases, the less common constituents like Fe, FeS, $FeNi_3$ (a non-stoichiometric low temperature phase), NiS and $FeCl_2$ were also revealed by SEM. Figure 5.5 and Figure 5.6 show the micrographs of $FeNi_3$ and the needle-like $FeCl_2$ phase, respectively. Moreover, XRD (Figure 5.7) and EDS results confirm the composition of all the above phases.

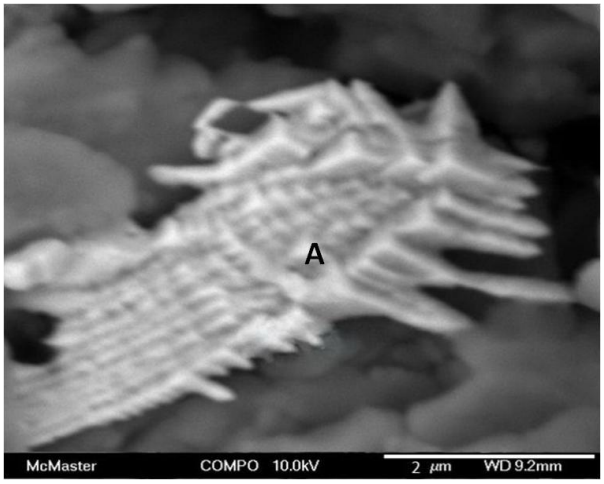

Figure 5.5 $FeNi_3$ phase (A).

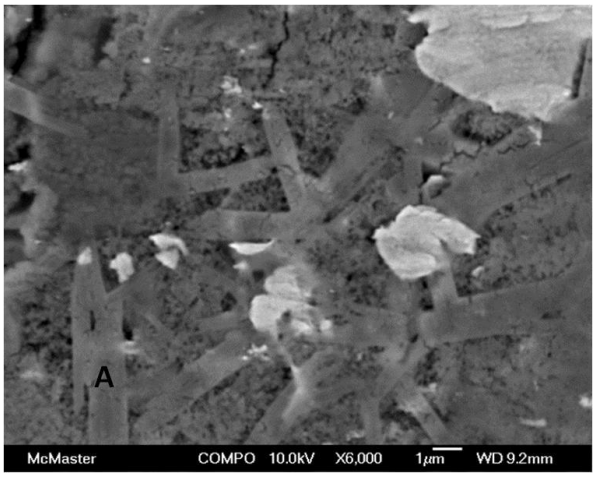

Figure 5.6 Needle-like $FeCl_2$ crystals (A).

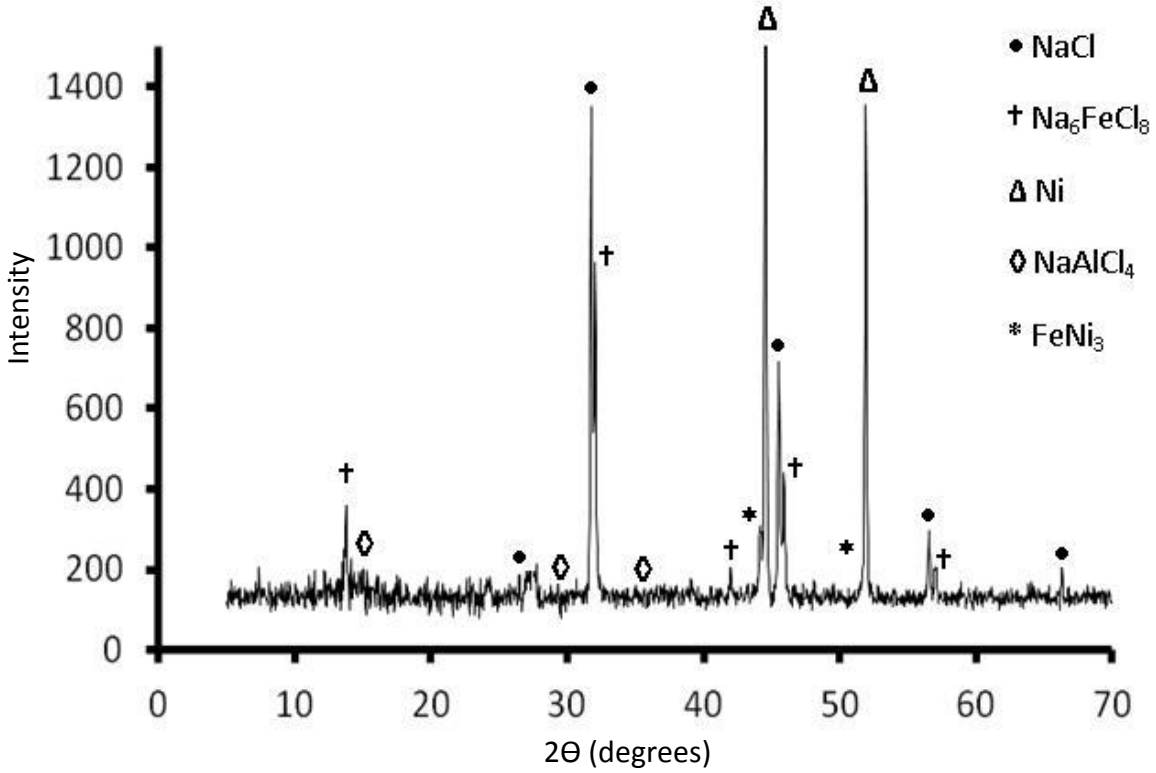

Figure 5.7 XRD pattern of discharged cell cathode.

Figure 5.8 (a) shows the micrograph of the NiS phase that was taken from the middle part of the C763 cathode. The EDS mapping data also confirm its formation; (Figure 5.8).

Figure 5.9 compares the nickel particle size in cells C1, C3 and C763. Image analysis results taken from different parts of the cathode reveal that Ni particles grow larger (5-10 μm) with number of cycles and then stabilize. The Ni particle size in Figure 5.9 (c) shows that the growth of Ni grains is attenuated with age.

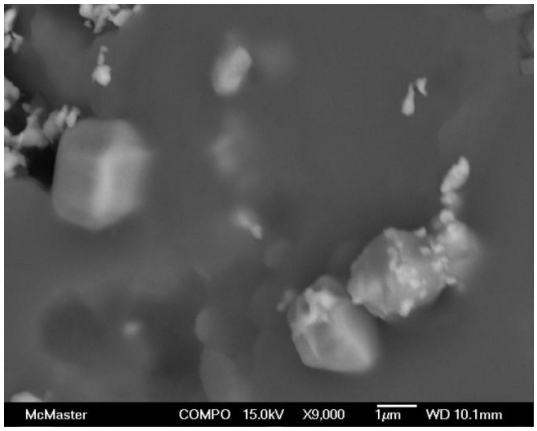

(a)

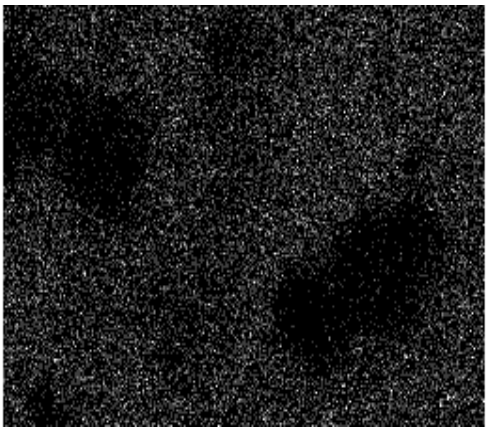

(b) Na $K\alpha_1$

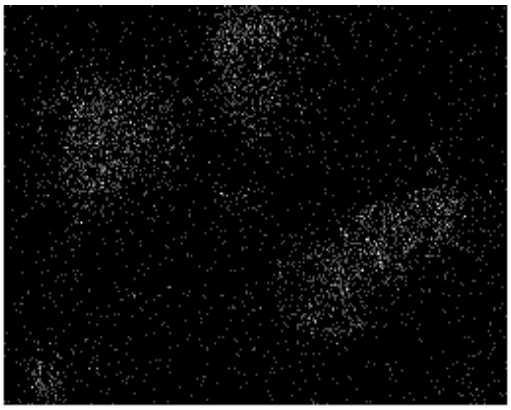

(c) S $K\alpha_1$

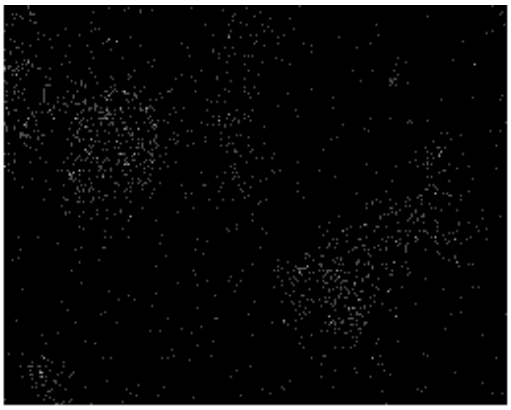

(d) Ni $K\alpha_1$

(e) Fe $K\alpha_1$

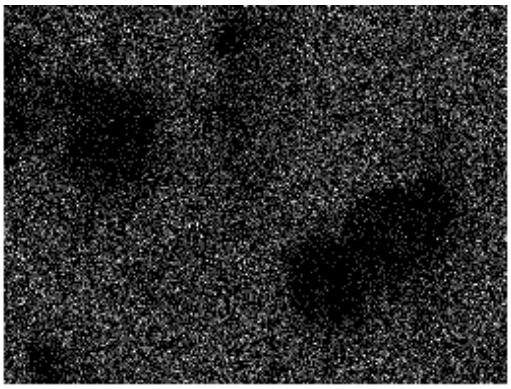

(f) Cl $K\alpha_1$

Figure 5.8 SEM image of NiS crystals in the middle of the C763 cathode and EDS maps for Na, S, Ni, Fe, and Cl.

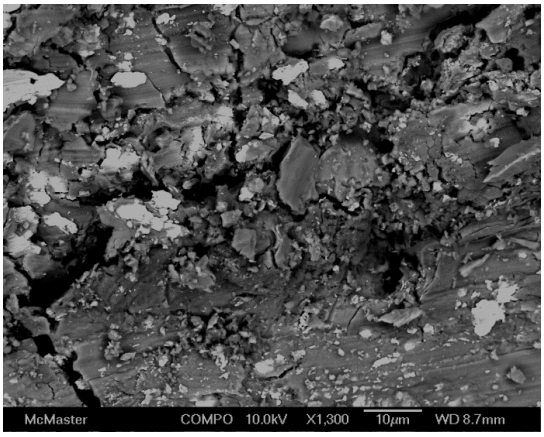

(a)

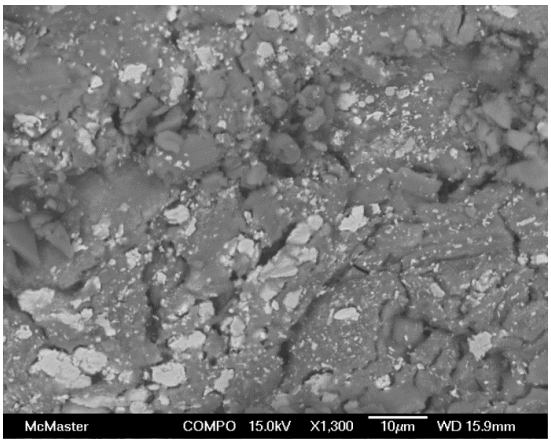

(b)

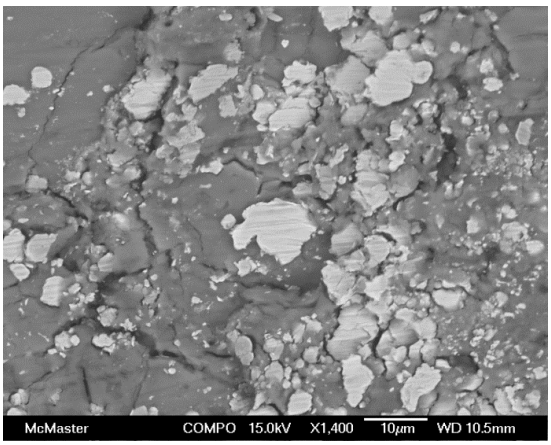

(c)

Figure 5.9 Ni particles in a) C1 after 1 cycle, b) C3 after 3 cycles, and c) C763 after 763 cycles.

Cubic NaCl crystals were found throughout the cathode, even near the cathode current collector (Figure 5.10) in cells with 70% DoD or in a completely charged cell (charge 10 A to 2.67 V to 0.5 A) (Figure 5.11).

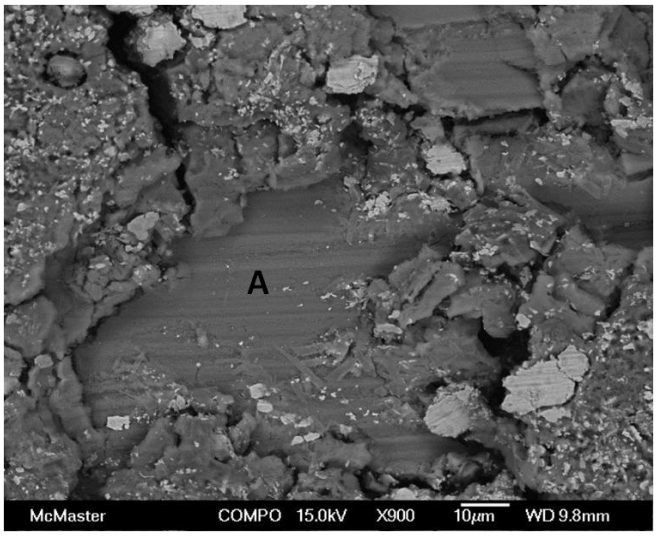

Figure 5.10 Presence of NaCl crystals (A) near current collector in C763.

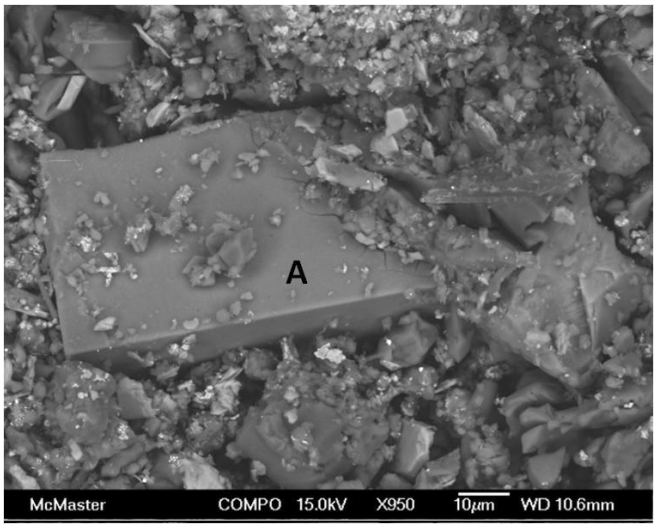

Figure 5.11 NaCl crystal (A) in fully charged cell.

The NaCl formation in the region near current collector can be explained in different ways. We can consider two types of reaction fronts, i.e., diffuse or narrow. In the former, the cycling reaction occurs in a wide reaction band. In this case the presence of NaCl around the current collector can be attributed to Na^+ reaction with $NiCl_2$ over a range of several millimetres. In the latter, the reaction front is confined to a narrow reaction band. The cell reaction ($Na + NiCl_2 = NaCl + Ni$) is expected to proceed from the beta electrolyte toward the center but since the DoD is only 70% of cell capacity, the reaction will affect only the outer half of the cathode, leaving the inner half in its original charged state. Therefore, the presence of NaCl crystals near the current collector would be abnormal and needs to be accounted for by a different mechanism.

Since the vacuum distillation procedure can significantly alter the cathode composition and microstructure from its normal operating state, one aged cell with 763 cycles was examined for comparison without the vacuum treatment. Again, NaCl was found near the current collector with crystals over 100 µm in size (Figure 5.12). This long life cell had shown normal operating behavior with the usual fade in capacity.

In addition, there was evidence of $NiAl_2Cl_8$ found by XRD (Figure 5.13), which was also found by Fiamm SoNick near the beta electrolyte in a fully charged cell.

Figure 5.14 shows a focused ion beam (FIB) cross-section of the cathode. The Na_6FeCl_8 phase (E) is found adjacent to the NaCl (B), Ni particles (D), and layered $NiCl_2$ (A). The presence of Na_6FeCl_8 was also confirmed by XRD as seen in Figure 5.7.

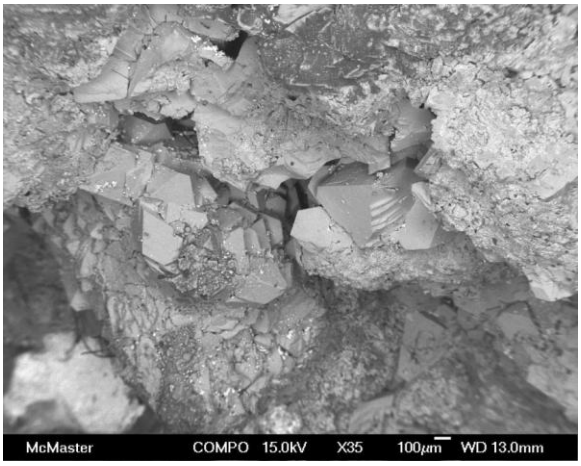

Figure 5.12 NaCl crystals several hundred microns in size near the current collector after 763 cycles (without vacuum distillation procedure).

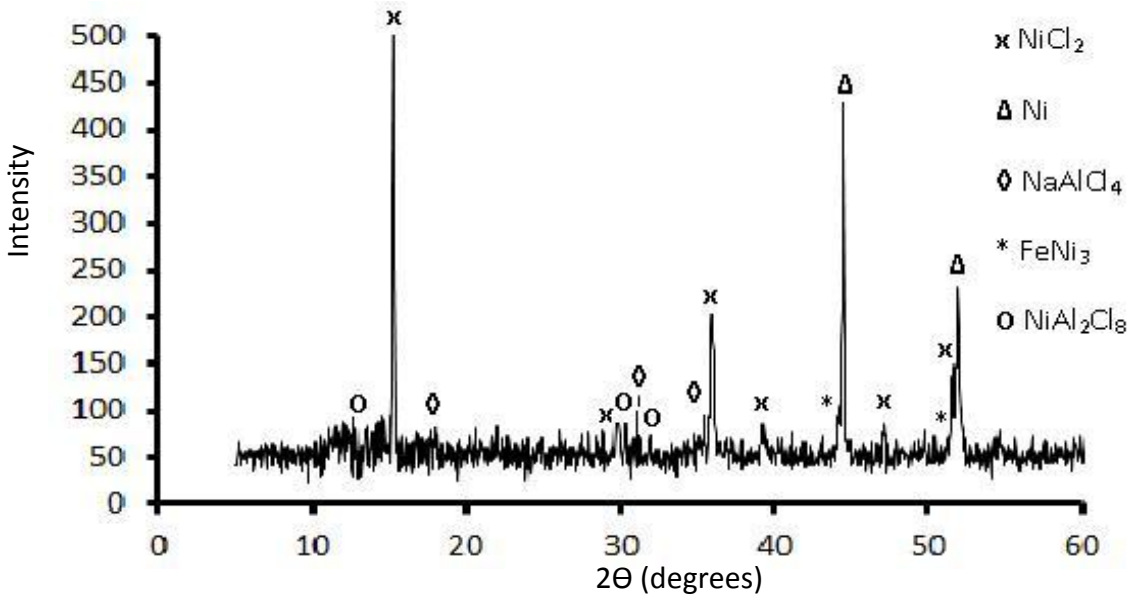

Figure 5.13 XRD pattern of cathode near the beta electrolyte in a fully charged cell.

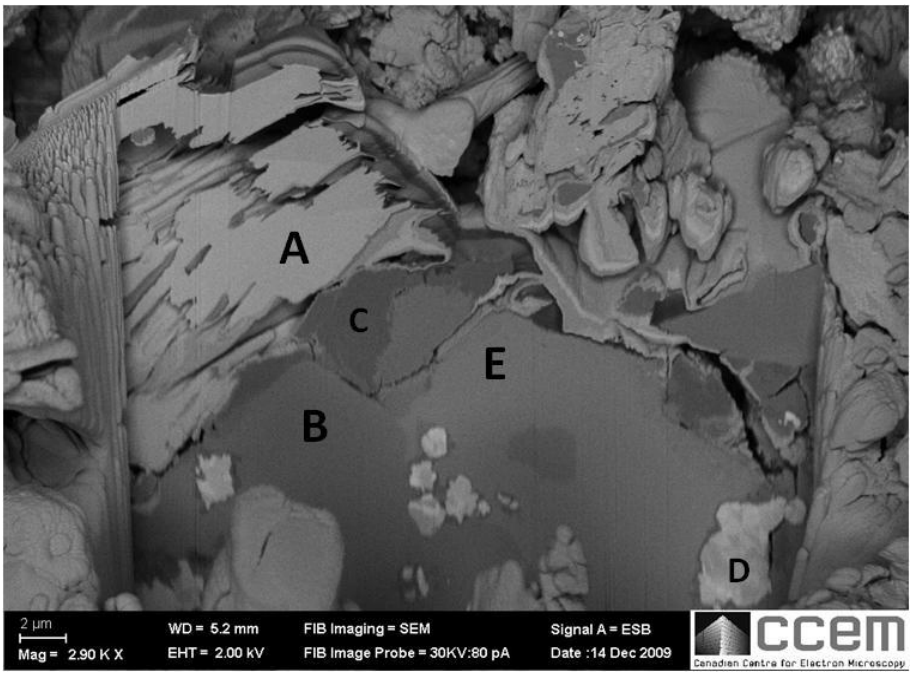

Figure 5.14 Image of sample from charged cell prepared by FIB: (A) $NiCl_2$, (B) NaCl, (C) $NaAlCl_4$, (D) Ni, (E) Na_6FeCl_8.

5.2 Thermodynamic modeling

To determine the potential changes of vacuum treatment at 450˚C on subsequent SEM examination at room temperature, calculations were performed with FactSage software.

First, the vapor pressures of all possible cathode species were determined as a function of temperature. The most volatile species in the $NiCl_2$-NaCl-$NaAlCl_4$ mixture are $AlCl_3$ and $NaAlCl_4$, followed by Al_2Cl_6 and $Na_2Al_2Cl_8$ (Figure 5.15). Moreover, the vapor

pressure increases from 10^{-6} atm at 300˚C to 10^{-4} atm at 450˚C. Therefore, heating under vacuum at 450˚C will evaporate some liquid $NaAlCl_4$ but most will decompose to solid NaCl and $AlCl_3$ gas. The consequence is that crystalline NaCl artifacts may be left that are not indicative of the true equilibrium state of the operating cell. However, such artifacts would occur mainly at the evaporating surface, normally the opening at the top of the cell.

Moreover, an additional thermodynamic calculation showed that the presence of $Fe/FeCl_2$ does not significantly alter the vapor composition of the cell and $FeCl_2$ would account for less than 1% of what is removed during vacuum distillation (Figure 5.15). $FeCl_3$ pressure is much lower still because of its lower stability relative to that of $NiCl_2$.

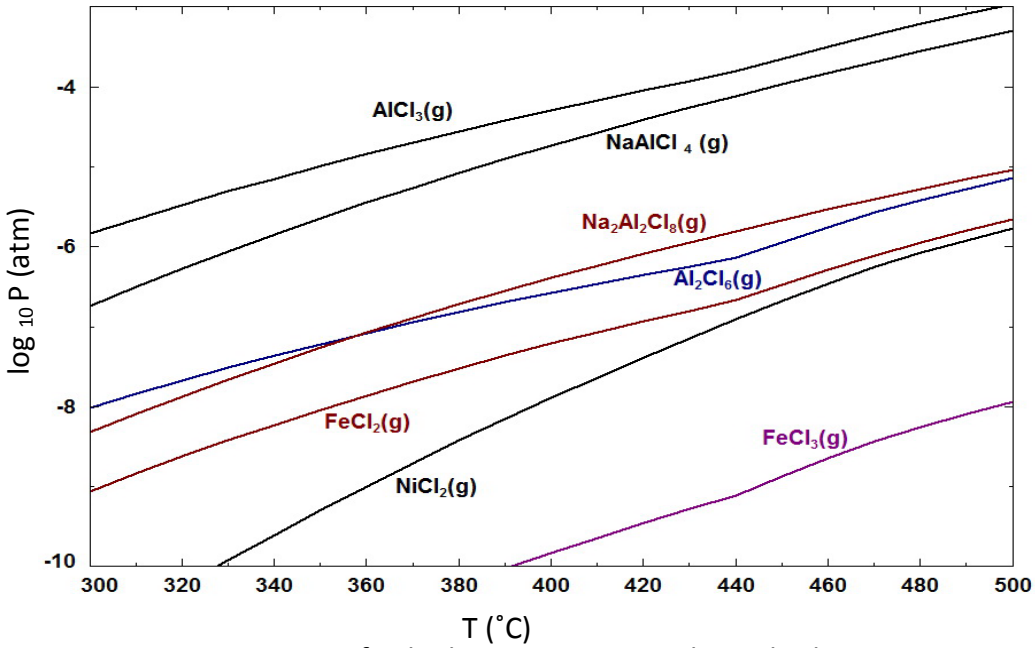

Figure 5.15 Vapor pressures of volatile components in the cathode versus temperature determined by FactSage calculation.

A thorough examination of cell reactions during cycling and phase changes that occur during cooling can be modeled by FactSage. The key reactions in the cathode can be depicted by the $(NaCl)_2$-$NiCl_2$-$AlCl_3$ ternary phase diagram. The temperature was arbitrarily set at 300˚C as a representative temperature for the normal 260-350˚C operating range (Figure 5.16).

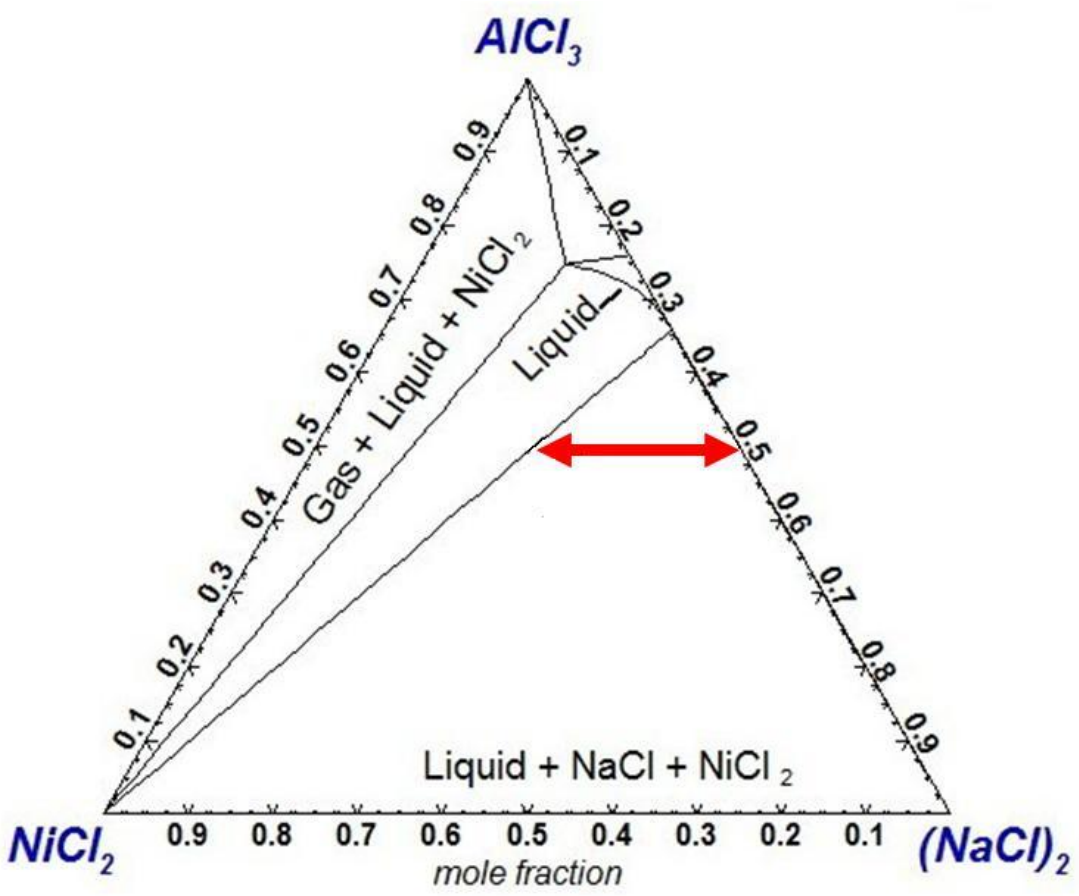

Figure 5.16 Ternary diagram of $(NaCl)_2$-$NiCl_2$-$AlCl_3$ at 300˚C with cell reaction range indicated for a cell filled with 50% solids (half Ni, half NaCl) and 50% liquid $NaAlCl_4$, all on a molar basis.

This diagram contains one non-stoichiometric phase (the liquid $NaAlCl_X$ binary compound containing dissolved $NiCl_2$) in addition to the three (virtually pure) end components. The liquid solution phase is surrounded by 2-phase and 3-phase regions. The region most relevant to the ZEBRA cell is the one containing the three phases, liquid + $NiCl_2$ + NaCl. The cell reaction can be considered as a back and forth shuttle of Cl between Na and Ni. Since neither metal has appreciable solubility in the three chloride phases nor in each other, the pure metals may be omitted from the phase diagram without sacrificing any detail of the mechanism.

Since the cell reaction involves the formation/disappearance of NaCl and $NiCl_2$ and no change in the amount of $NaAlCl_X$ liquid, it can be represented by a horizontal line on the ternary diagram (Figure 5.16). The location of the line depends on the ratio of solid to liquid components in the cell. We have arbitrarily set the line at 50% $AlCl_3$ on the $(NaCl)_2$-$NiCl_2$-$AlCl_3$ diagram, or a 1:2 ratio of $AlCl_3$ to NaCl. This is equivalent to filling the cell with 25% Ni, 25% NaCl and 50% $NaAlCl_4$ on a molar basis, but Ni is omitted from the diagram.

The right end of this line corresponds to the state where the cell is fully discharged and contains NaCl but no $NiCl_2$ (composition of 33% $AlCl_3$, 0% $NiCl_2$, 67% NaCl). Moving along the line to the left is equivalent to charging the cell until the 2-phase $NiCl_2$+L region is encountered and no crystalline NaCl remains. This point represents the normal 100% charged state.

Overcharging will push the cell composition further left, and conceivably such overcharging could continue until all the NaCl is removed from the cathode (the composition point 50% $AlCl_3$, 50% $NiCl_2$, 0% NaCl), although this condition would be impossible to reach in a real cell.

The cell reaction can be illustrated in a different way with the use of a temperature-composition diagram (Figure 5.17). The endpoints of this isoplethal section are $AlCl_3$+$NiCl_2$ and $AlCl_3$+$(NaCl)_2$. The isoplethal section has the features of a normal binary diagram except that the various regions contain an additional component, consistent with the Gibbs phase rule. Note that this diagram is consistent with the reaction line on the ternary diagram in Figure 5.16.

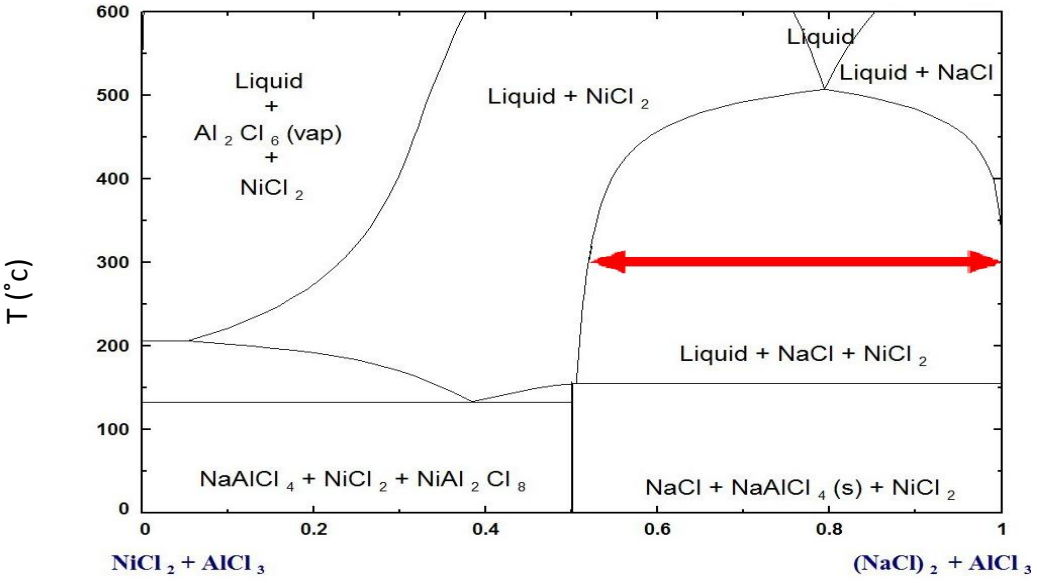

Figure 5.17 Vertical section through the $(NaCl)_2$-$NiCl_2$-$AlCl_3$ ternary diagram at constant $AlCl_3$ equal to 50 %.

The normal operating range of the ZEBRA cell at 300˚C is in the 3-phase region, L+$NiCl_2$+NaCl, on the right hand side of the diagram. If the cell is cooled below 155˚C, the liquid undergoes a eutectic reaction and solidifies into a mixture of $NaAlCl_4$ + excess NaCl because the liquid is slightly rich in NaCl. Thus, even if the cell is fully charged, NaCl precipitates will appear everywhere in the cathode when it is examined at room temperature. In order to completely eliminate NaCl from the frozen cathode (assuming equilibrium at 300˚C), it is necessary to charge the cell to the stoichiometric ratio of 50:50 NaCl/$AlCl_3$. If the cell is charged beyond this point, then the phase diagram shows that $NiAl_2Cl_8$ is expected to be stable at room temperature as seen in Figure 5.18.

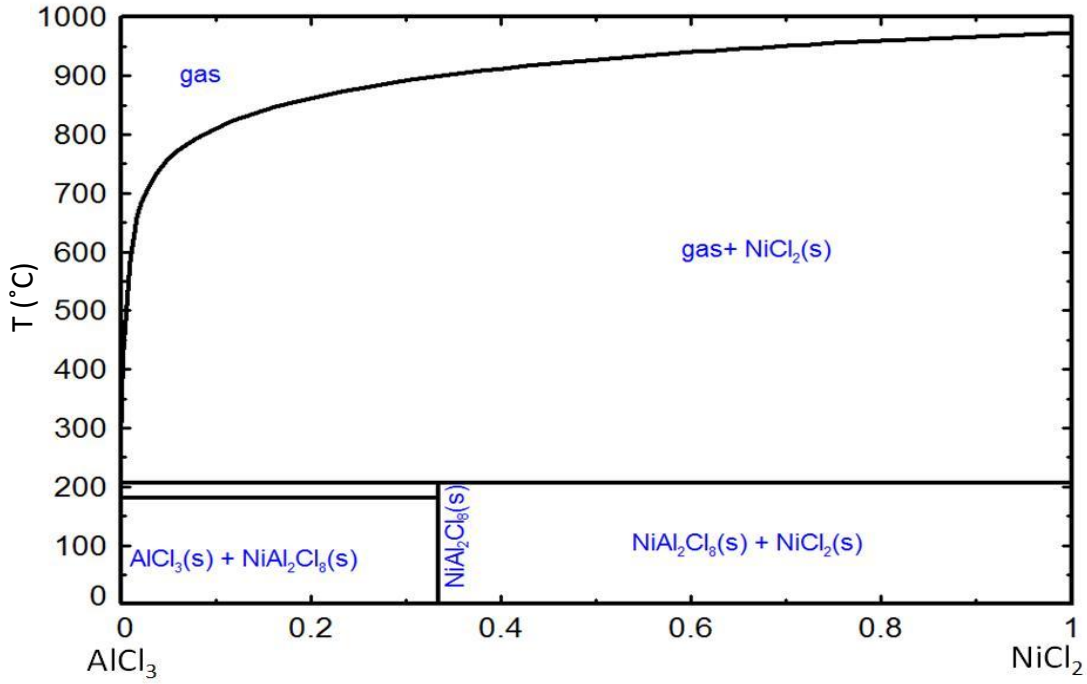

Figure 5.18 The binary $AlCl_3$- $NiCl_2$ diagram from FactSage.

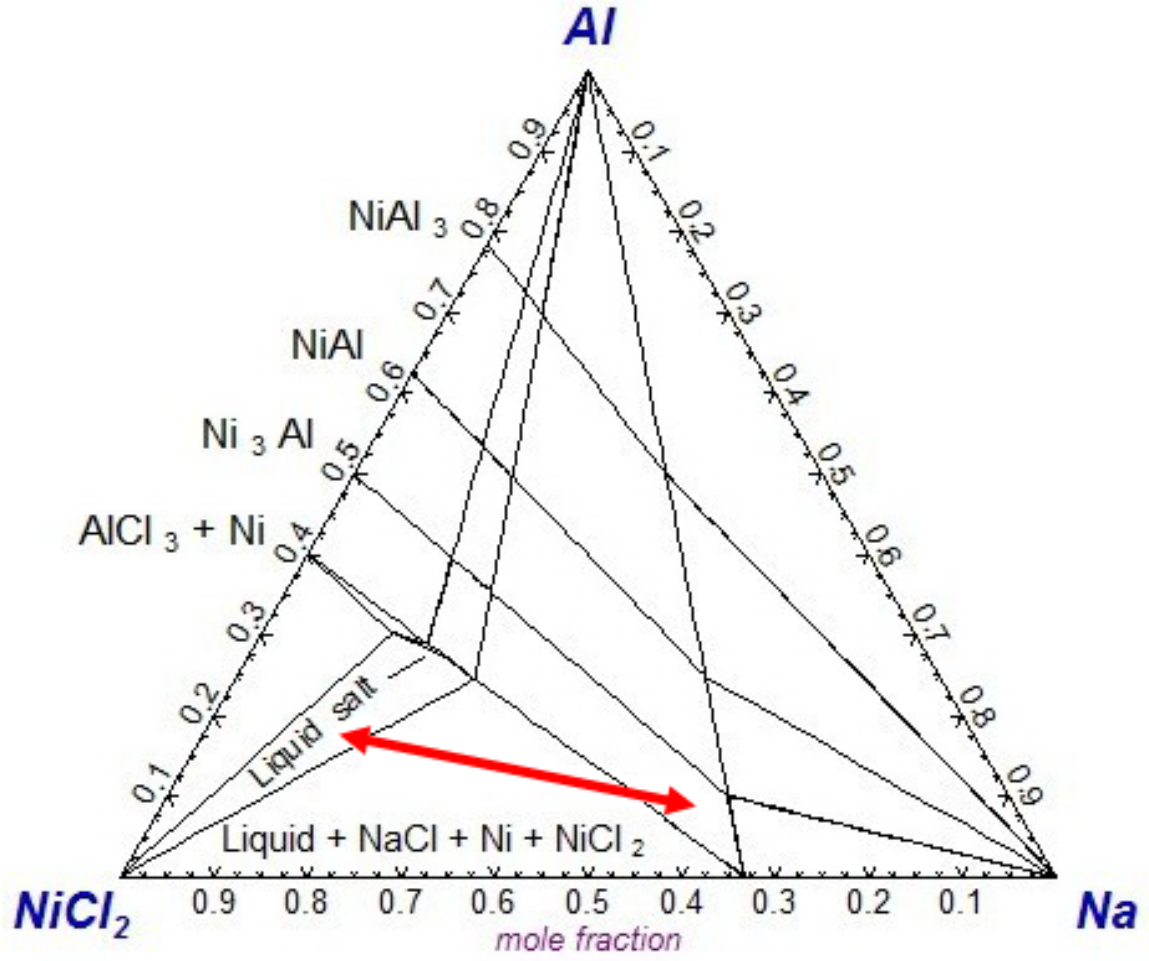

Figure 5.19 Extended ternary diagram showing stability of Ni_3Al phase at the right end of the arrow.

Under actual operating conditions with occasional cooling of the battery to room temperature, crystalline NaCl that precipitates will be difficult to remove from the centre of the cathode because of the long diffusion distance and associated high transport resistance. Residual NaCl crystals remaining after charging will act as nuclei during discharge, and these crystals may be expected to grow with cycling. Larger

crystals will take longer to dissolve and become permanent during routine cycling. Thus the cell is not in its equilibrium state and when connected in series in a battery, a cell with large residual NaCl crystals could be pushed to overcharge, represented by the L+$NiCl_2$ region on the phase diagram. One may note that the solubility of $NiCl_2$ beyond 50% $AlCl_3$ increases with depth of overcharge which could result in Ni grain growth.

Alternatively, if a cell is over discharged, thermodynamic analysis shows that Ni_3Al will form. This is explained by the fact that all the $NiCl_2$ has been converted to Ni and additional Na will displace the Al from liquid $NaAlCl_X$ to form NaCl + Al; under equilibrium conditions, the free Al can react with Ni to form Ni_3Al (Figure 5.19). This intermetallic phase has been identified by XRD analysis in a failed Fiamm SoNick cell.

5.3 Electrical conductivity

Figure 5.20 shows the FIB cross section of a cathode in the charged state. An isolated Ni particle (A), which is surrounded by $NaAlCl_4$ (B) can be seen. As the $NaAlCl_4$ is an ionic conductor, these isolated Ni particles cannot contribute to the electronic conductivity path and the capacity of the cell decreases. One way to avoid this loss of capacity would be to use a mixed conducting molten salt. Therefore, the conductivity of $NaAlCl_4$ was measured and several additives were used in an effort to improve the electronic component of conductivity.

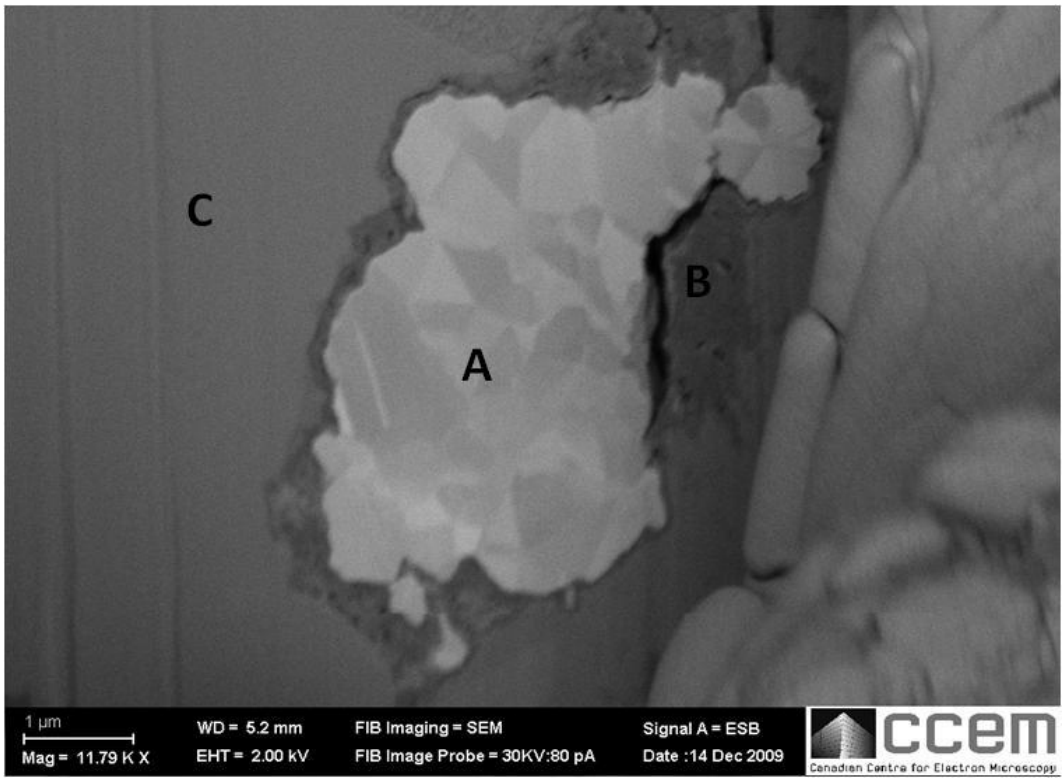

Figure 5.20 Isolated Ni particle (A) in charged cell is surrounded by ionic conductor phases; (B) $NaAlCl_4$, (C) NaCl.

In addition, Figure 5.20 shows channeling contrast for the polycrystalline nickel particle. The observed varying contrast in the secondary electron image for polycrystalline nickel particles is due to the ion channeling effect [97-98]. The channeling contrast occurs because secondary electron yield depends on the crystallographic orientation of the sample. When a grain of polycrystalline material is aligned to a high index plane (hkl), based on equation 5.1 [82] the magnitude of the interplanar spacing

(d_{hkl}) is small and thus, the number of emitted secondary electrons increases which indeed causes the grain to appear lighter.

$$d_{hkl} = \frac{a}{\sqrt{h^2+k^2+l^2}} \quad (5.1)$$

In general, the ion channeling is considerable in materials that have higher atomic densities and closed packed crystal structure, such as, Ni, Cu, Al, etc. [98].

The conductivity data were fitted to a second order polynomial equation. Table 5.1 shows the parameters of the conductivity equation. Moreover, the polynomial conductivity equation of $NaAlCl_4$ in degree Celsius and Kelvin is shown in equation (5.2, and (5.3), respectively.

Table 5.1 Parameters of conductivity equations of $NaAlCl_4$.

Conductivity, $\sigma\ (S.cm^{-1}) = a + bT + cT^2$					
Electrolyte	Temperature (˚C)	-a	b X 10^{-3}	-c X 10^{-6}	Standard deviation
$NaAlCl_4$	160 - 400	0.1511	4	4	0.004

$$\sigma\ (S.cm^{-1}) = -0.1511 + 0.004T - 4 \times 10^{-6}T^2 \quad (T˚C) \quad (5.2)$$

$$\sigma\ (S.cm^{-1}) = -1.558 + 0.0063T - 4 \times 10^{-6}T^2 \quad (T/K) \quad (5.3)$$

Figure 5.21 shows the electrical conductivity of pure $NaAlCl_4$ with temperature. It is shown that the conductivity of $NaAlCl_4$ increases with temperature and its temperature dependence trend follows the form suggested by Yaffe and Van Artsdalen [99].

The trend of the conductivity curve versus temperature suggests a maximum at a high temperature similar to those observed for other alkali compounds [51]. Beyond that high temperature the conductivity will decrease with increasing temperature. However, the present measurements are below the maximum temperature but the increasing trend to reach a maximum can be seen.

Furthermore, the sudden increase in electrical conductivity at 160˚C corresponds to the melting temperature of $NaAlCl_4$.

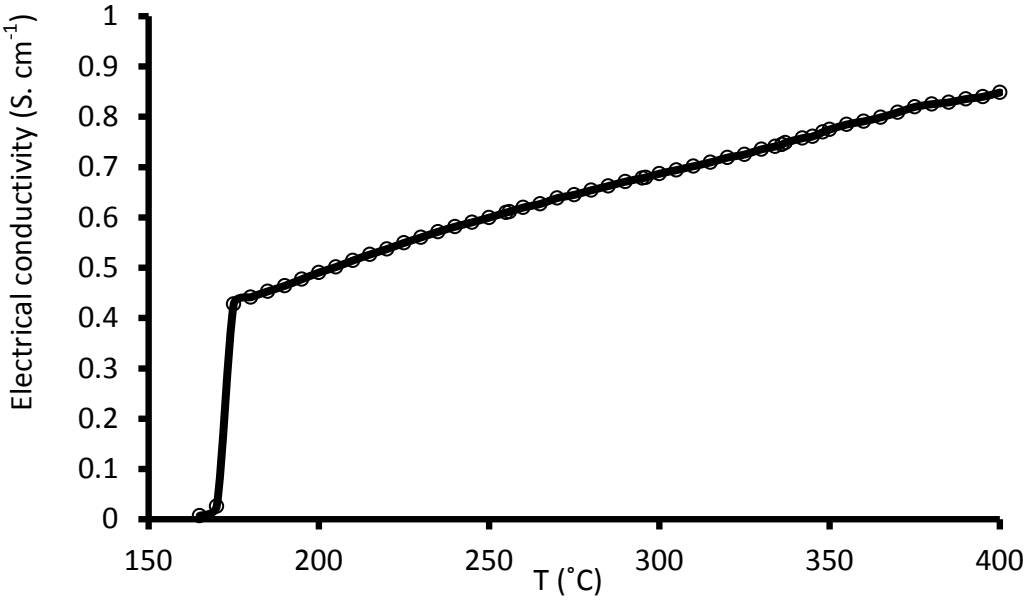

Figure 5.21 Electrical conductivity of $NaAlCl_4$ as function of temperature.

Figure 5.22 shows the above equation of the fitted data against the results of Mohandas et al [50] and Janz et al [45]. The present equation is within 10 % of previous measurements.

The above measurement represents the total conductivity of $NaAlCl_4$ molten salt which is essentially ionic. In order to find the electronic component of the total conductivity, DC measurement techniques were applied.

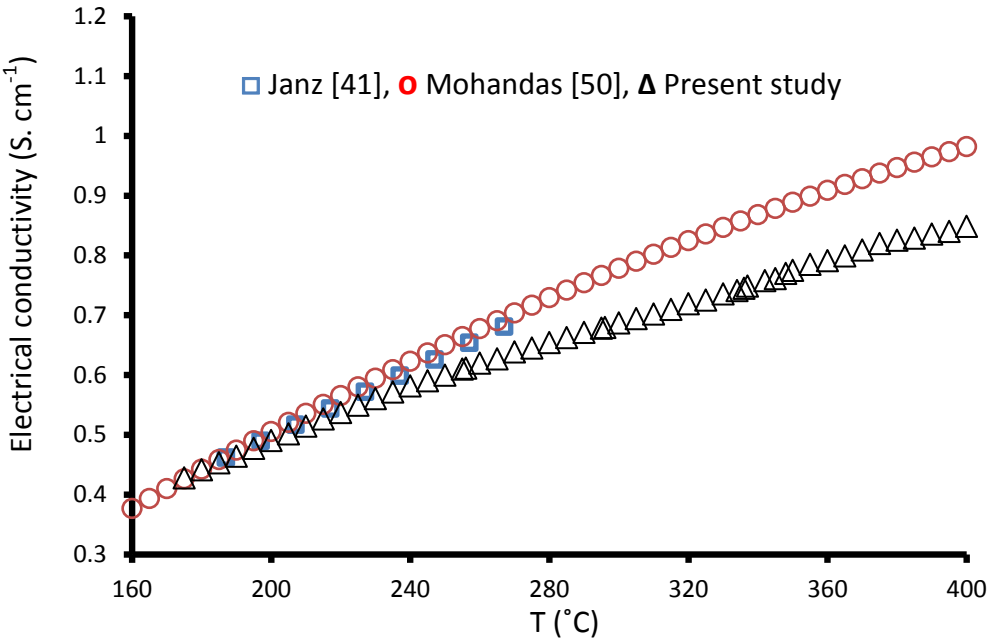

Figure 5.22 The electrical conductivity of $NaAlCl_4$ versus temperature in 3 different studies.

$NaAlCl_4$ contains sodium cations (Na^+) and large tetrachloroaluminate anions ($AlCl4^-$). Howie and McMillan observed that the charge carriers are Na^+ ions as they are more mobile species compared to large $AlCl_4^-$ anions [49-50]. Moreover, the transport number of Na^+ ion is greater than 0.9 [50, 100] which means that the main portion of the current is carried by Na^+ ion species. Other investigations on $LiAlCl_4$ also confirm that Li^+ ions are responsible for electrical conduction. Therefore, in alkali chloroaluminate melts such as $NaAlCl_4$, the alkali metal cations are the main charge carriers [50, 101].

The ionic conductivity of the liquid electrolyte ($NaAlCl_4$) at operating temperature of the ZEBRA battery (300˚C) is around 0.68 S/cm. In order to have the cell working properly, the electronic conductivity should not be less than the above value. In present ZEBRA cell, the electronic conductivity is provided through nickel backbone structure which is well beyond the requirements. In order to ensure the backbone structure formation, excess nickel particles are added in the cathode mixture. Nickel metal has high density and thus, the major portion of the ZEBRA cell weight is attributed to the excess nickel metal.

The purpose of this research is to improve the cell kinetics by increasing the electronic conductivity of the molten salt. In case of having a mixed conductive electrolyte, the ZEBRA cell can be made much lighter while having enough electronic conductivity. Moreover, the mixed conductive electrolyte makes the isolated Ni particles participate in the cell reaction and prevents the possible capacity loss in ZEBRA cells.

In this regard, the effects of adding different concentrations of $NbCl_5$ to $NaAlCl_4$ at 300˚C were investigated. Niobium has different valence states (Nb^{2+}, Nb^{3+}, Nb^{4+}, …) which are stable at the chlorine partial pressure of a Ni-$NiCl_2$ mixture (P_{Cl2} = 1.48 x 10^{-20} atm) and can change from one to other to provide electronic conduction. Moreover, it does not react with the other components of the ZEBRA cell cathode which makes it a suitable candidate for providing electronic conductivity within the cell.

The effect of adding different concentrations of $NbCl_5$ to $NaAlCl_4$ conductivity as function of temperature is shown in Figure 5.23.

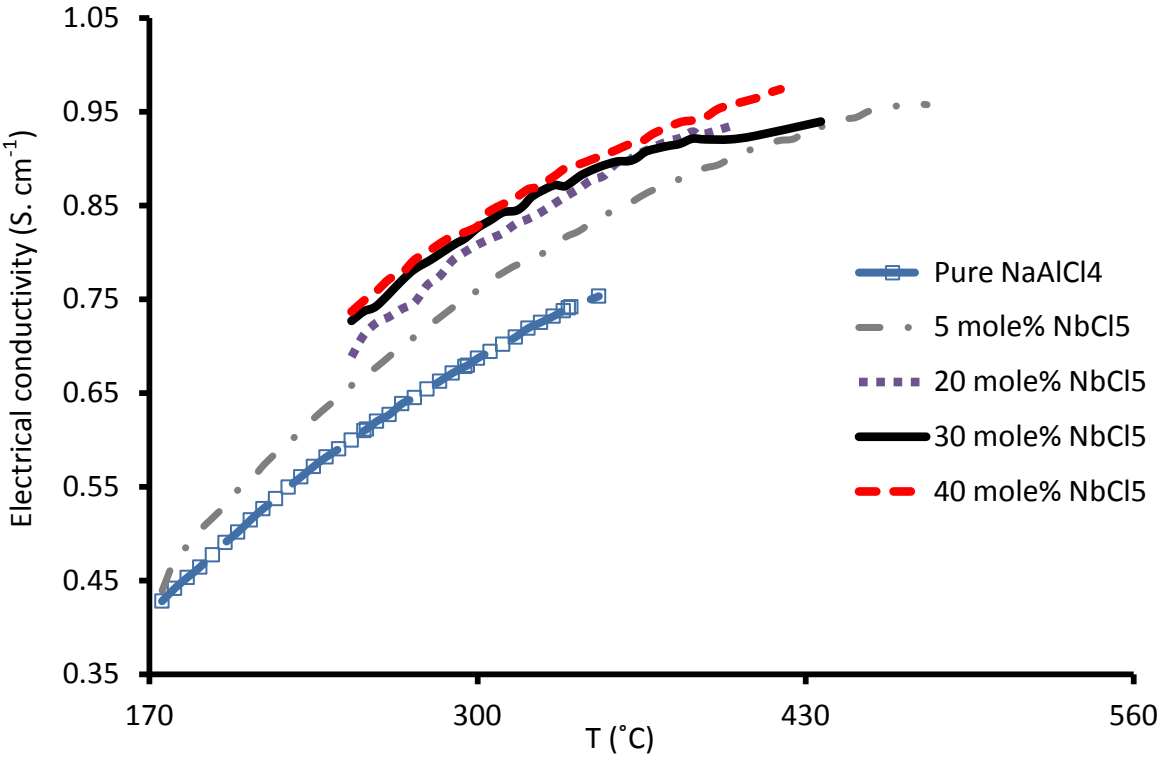

Figure 5.23 The effect of $NbCl_5$ addition to $NaAlCl_4$ on conductivity.

Table 5.2 shows the parameters of conductivity equations of different mole percent $NbCl_5$ + $NaAlCl_4$ mixtures. In order to simplify the samples name, the mole percent ratio of $NbCl_5$:$NaAlCl_4$ is shown as Nb:Na=mole percent ratio.

Table 5.2 Parameters of conductivity equations and standard deviations of different concentrations of $NbCl_5$+ $NaAlCl_4$ mixtures.

Conductivity, $\sigma\ (\mathrm{S.cm^{-1}}) = a + \mathrm{bT} + \mathrm{cT}^2$					
Electrolyte	Temperature (˚C)	-a	b X 10^{-3}	-c X 10^{-6}	Standard deviation
$NaAlCl_4$	160 - 400	0.1511	4	4	0.004
Nb:Na=0.05	150-478	0.176	4.4	4	0.0038
Nb:Na= 0.2	250-400	0.254	5.2	5	0.0031
Nb:Na= 0.3	250-436	0.2275	5.4	6	0.0029
Nb:Na=0.4	250-420	0.0465	4.2	4	0.0043

Figure 5.23 shows that the conductivity of $NaAlCl_4$ increases by adding $NbCl_5$ up to 40 mole %. However, measuring the conductivity of 50 mole % $NbCl_5$ or over has some technical problems due to vaporization of $NbCl_5$ which leads to formation of bubbles inside the capillary cell, disrupting the electrical path inside the U-tube cell. Therefore, the values above 50% are less reliable.

Figure 5.24 shows the conductivity of different mixtures of $NbCl_5$ and $NaAlCl_4$ at 300˚C. The conductivity of 30 mole % and 40 mole % are quite similar. Moreover, the conductivity decreases as the concentration of $NbCl_5$ increases more than 40%. This can be related to high evaporation of $NbCl_5$. The 30 mole % $NbCl_5$ is selected for further experiments and the $NbCl_5$:$NaAlCl_4$ ratio was shown as Nb:Na=0.3.

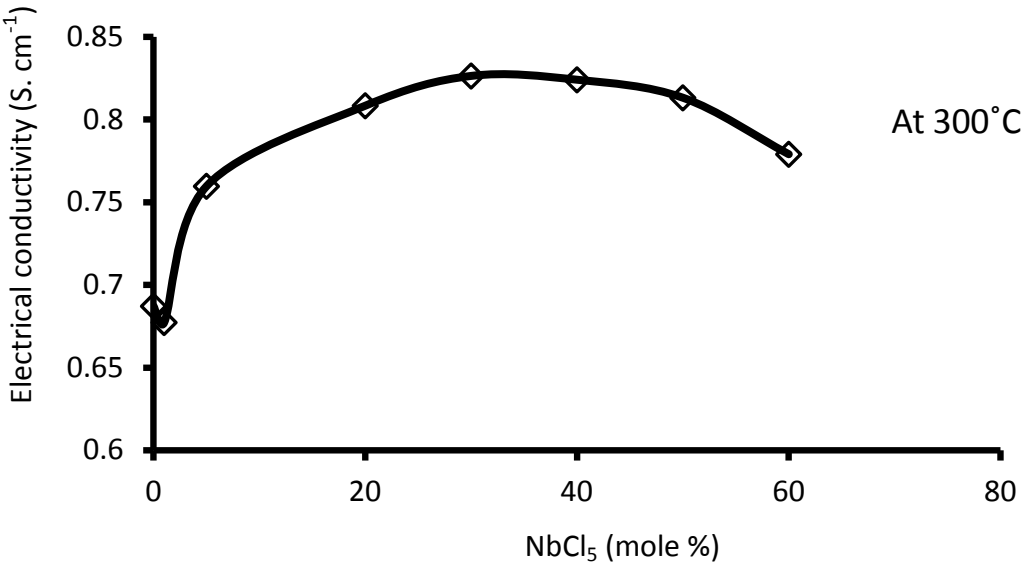

Figure 5.24 The electrical conductivity of the different mixtures of $NbCl_5$ and $NaAlCl_4$ at 300˚C.

Electrical conductivity of molten salt with added $NbCl_5$ shows a slightly higher conductivity than pure $NaAlCl_4$. This increase can be attributed to decreased viscosity of the molten salt, judging from observed fluidity.

As $NbCl_5$ is a fully saturated compound with all electrons stripped to the krypton shell, additives were added to effectively decrease the chlorine pressure and reduce $NbCl_5$ to $NbCl_4$, $NbCl_3$, and $NbCl_2$. In this case, different valence states of Nb may be able to provide a mixed conductive electrolyte.

Different additives were used to reduce $NbCl_5$ such as Ni, Bi, Cu, and Sn, and their reducing behavior were predicted by FactSage software (Figure 5.25).

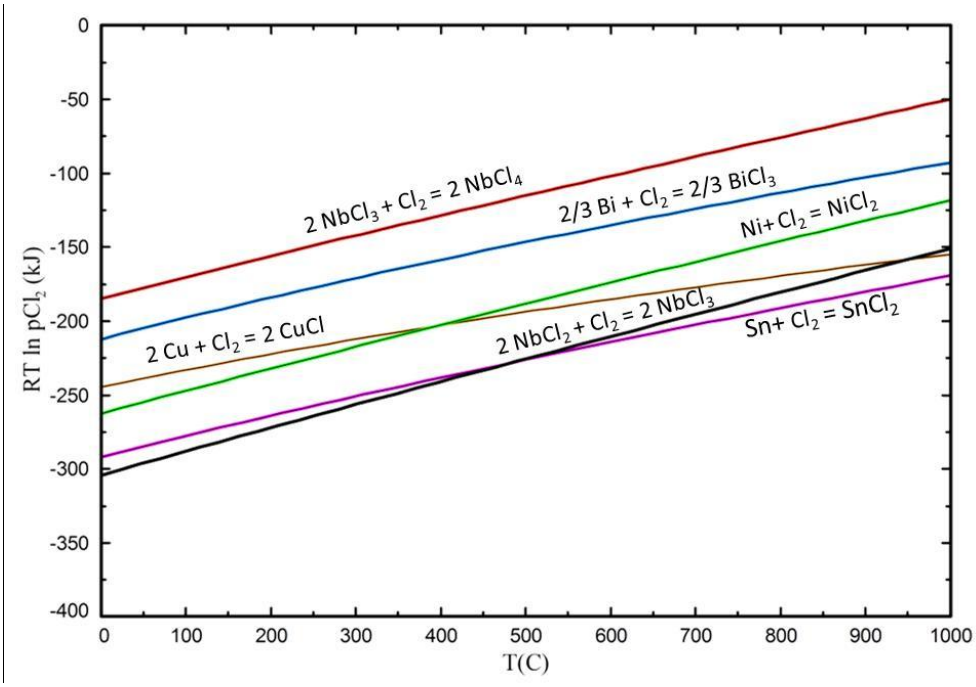

Figure 5.25 The Ellingham diagram for the chlorination of Nb, Ni, Cu, Bi, and Sn.

ΔG° for chlorination of Ni-$NiCl_2$, Cu-CuCl, Bi-$BiCl_3$, and Sn-$SnCl_2$ reactions are less than ΔG° for chlorination of $NbCl_3$-$NbCl_4$. Therefore, Ni, Cu, Sn, and Bi can act as reducing agents.

It is worth mentioning that as the presence of Nb ions in $NaAlCl_4$ solution is considered, the stoichiometric Nb_3Cl_8 and Nb_3Cl_7 compounds were removed from the calculations since these phases are stabilized only if the conditions for having a crystal structure are provided.

The thermodynamic behavior of the above mixtures was studied by FactSage software. It should be mentioned that FactSage has data for solid niobium chlorides and

the only liquid data is for $NbCl_5$. Figure 5.26 shows the stable species of niobium chloride in Nb-Cl_2 binary phase diagram. All niobium chloride species except $NbCl_5$ are in solid state. The liquid $NbCl_5$ evaporates at temperatures higher than 250˚C. Therefore, at operating temperature of the ZEBRA cell only solid niobium chloride compounds are present. This binary diagram is in consistence with the binary diagram of similar elements such as Mo-Cl_2. Therefore, the solid database that is provided by FactSage is reliable and can be used in the calculations.

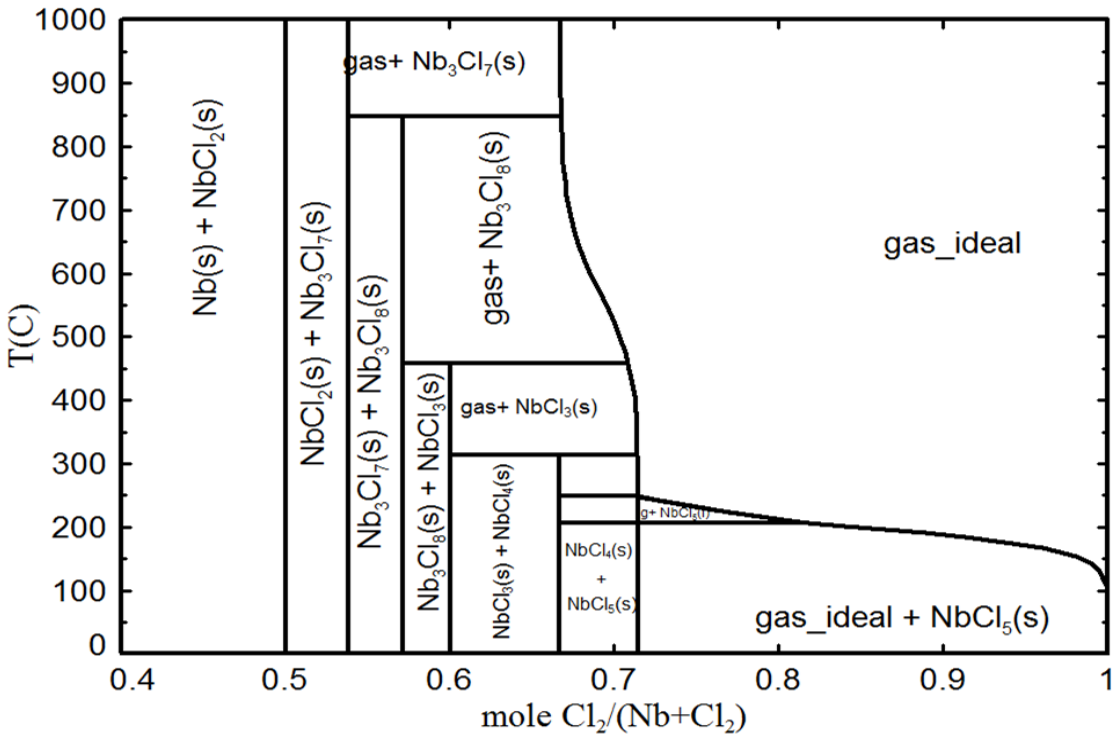

Figure 5.26 Nb-Cl_2 binary phase diagram.

Thermodynamic calculations show the possible phases present in the mixture of $NbCl_5$ and various reducing agents.

Figure 5.27 shows the thermodynamic equilibria obtained by adding different mole fractions of Ni to 1 mole $NbCl_5$ at 300˚C.

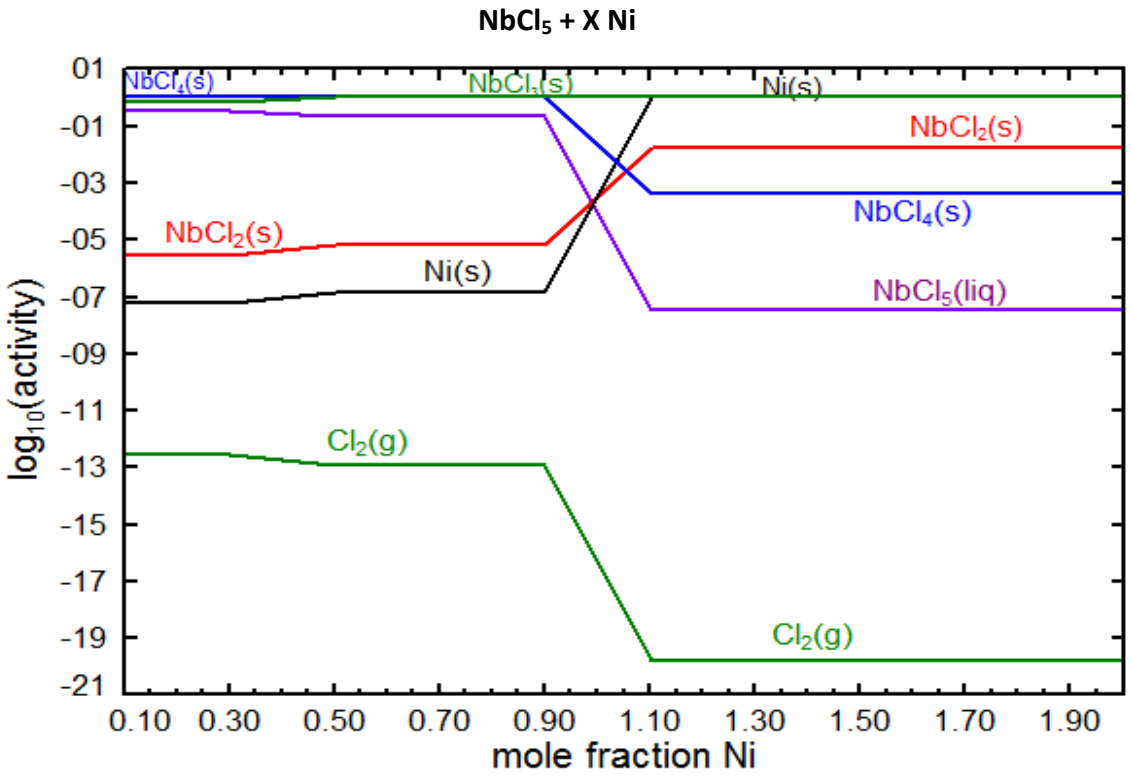

Figure 5.27 Thermodynamic calculations of adding different mole fractions of Ni to $NbCl_5$.

From the thermodynamic point of view, condensed species are stable when their activity is unity or the logarithm of their activity is equal to zero. Figure 5.27 shows that the chlorine pressure is continuously decreasing by adding more Ni as reducing agent and different stable phases form (log_{10}(activity)=0) in the mixture. In the ZEBRA cell the

chlorine pressure is fixed by Ni-$NiCl_2$ reaction at $P_{Cl2} = 1.48 \times 10^{-20}$ atm. Figure 5.27 shows that at this pressure the stable phase is $NbCl_3$ and solid Ni. Moreover, the activity of $NbCl_2$ increases at Ni concentrations more than 1.1 mole fraction. This means the fraction of Nb^{2+} in the solution increases and therefore, the possibility for electron hopping between Nb^{3+} and Nb^{2+} increases. Moreover, at Ni concentrations up to 0.9 mole fraction the $NbCl_4$ and $NbCl_3$ phases are formed simultaneously in the mixtures which increase the electronic conduction between Nb^{4+} and Nb^{3+}. Based on the above calculations (Figure 5.25 and Figure 5.27), Ni is a good candidate for reducing chlorine pressure of $NbCl_5$ and forming $NbCl_4$, $NbCl_3$ and $NbCl_2$. However, Ni metal is solid at operating temperature (300˚C) and it blocks the current path inside the capillary U-shaped cell and therefore, the effect of this metal on conductivity of mixture is not easily measured.

However, the effect of adding other reducing agents on the electrical conductivity of $NaAlCl_4$ + $NbCl_5$ mixture has been measured and the results are shown in Figure 5.28. The mole fraction ratio of $NbCl_5$:$NaAlCl_4$ and M (reducing agent):$NbCl_5$ mixtures are shown as Nb:Na and M (Sn, Cu, Bi):Nb, respectively.

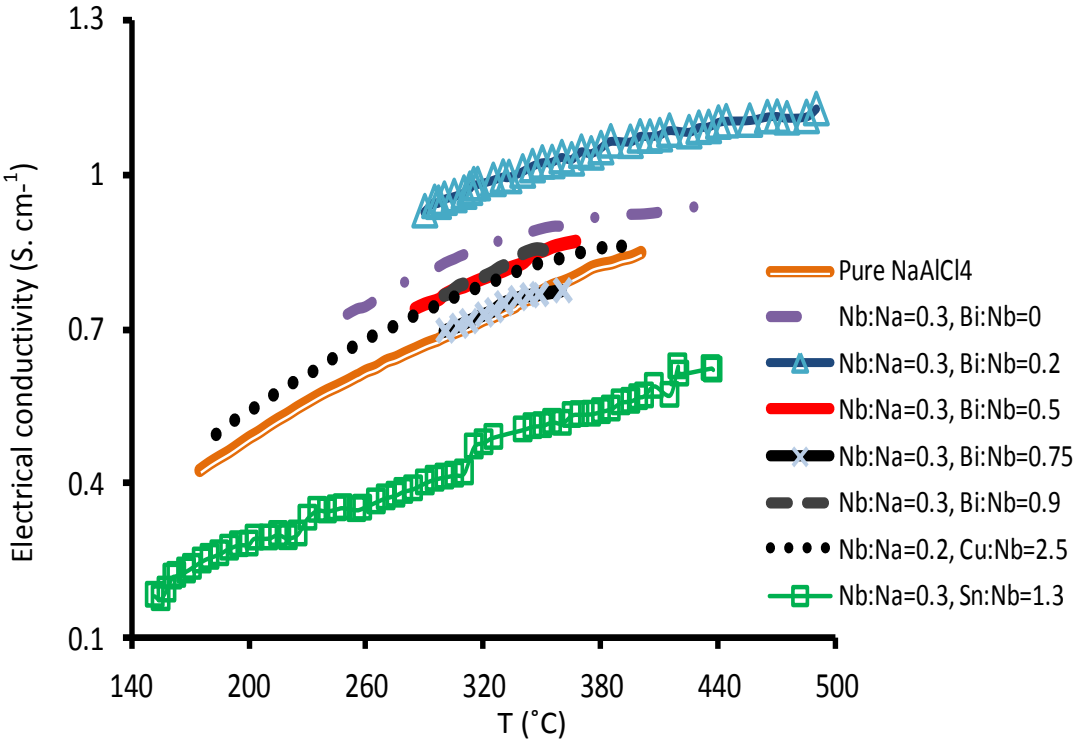

Figure 5.28 Electrical conductivity of $NaAlCl_4$ molten salt versus temperature and the effect of additives. The ratios are in mole fraction.

In general copper and tin decrease the total conductivity of the $NbCl_5$ and $NaAlCl_4$ mixtures and among these additives Bi is most promising.

Table 5.3 shows the parameters of conductivity equations of different reducing agents addition to Nb:Na=0.3.

Table 5.3 Standard deviations and parameters of conductivity equations of adding reducing agents to $NaAlCl_4$+$NbCl_5$ mixtures

Conductivity, $\sigma\ (\mathrm{S.cm^{-1}}) = a + \mathrm{bT} + \mathrm{cT^2}$					
Electrolyte	Temperature (˚C)	-a	b X 10^{-3}	-c X 10^{-6}	Standard deviation
$NaAlCl_4$	160 - 400	0.1511	4	4	0.004
Nb:Na= 0.3	250-436	0.2275	5.4	6	0.0029
Nb:Na=0.2, Cu:Nb=2.5	183-395	0.1739	4.5	5	0.028
Nb:Na= 0.3, Sn:Nb=1.3	152-437	0.0474	1.7	0.3	0.023
Nb:Na=0.3, Bi:Nb=0.2	290-490	-0.1863	3.6	3	0.008
Nb:Na=0.3, Bi:Nb=0.5	285-367	-0.1043	2.6	1	0.027
Nb:Na=0.3, Bi:Nb=0.75	300-360	1.1411	10	10	0.032

Figure 5.29 (a) shows the possible stable phases that form when different mole fractions of Sn is added to 1 mole $NbCl_5$ at 300˚C. Figure 5.29 (b) shows the upper portion of the graph at higher magnification.

We can see that there is a decrease in chlorine pressure by increasing the amount of Sn. Moreover, different species of niobium are stable at different chlorine pressures. Up to 0.9 mole fraction Sn the more stable species are $NbCl_3$ and $NbCl_4$. At concentrations more than 1.1 mole Sn, the chlorine pressure reaches 10^{-23} atm which is close to the chlorine pressure of the ZEBRA cell and both $NbCl_3$ and $NbCl_2$ are formed as stable species in the mixture.

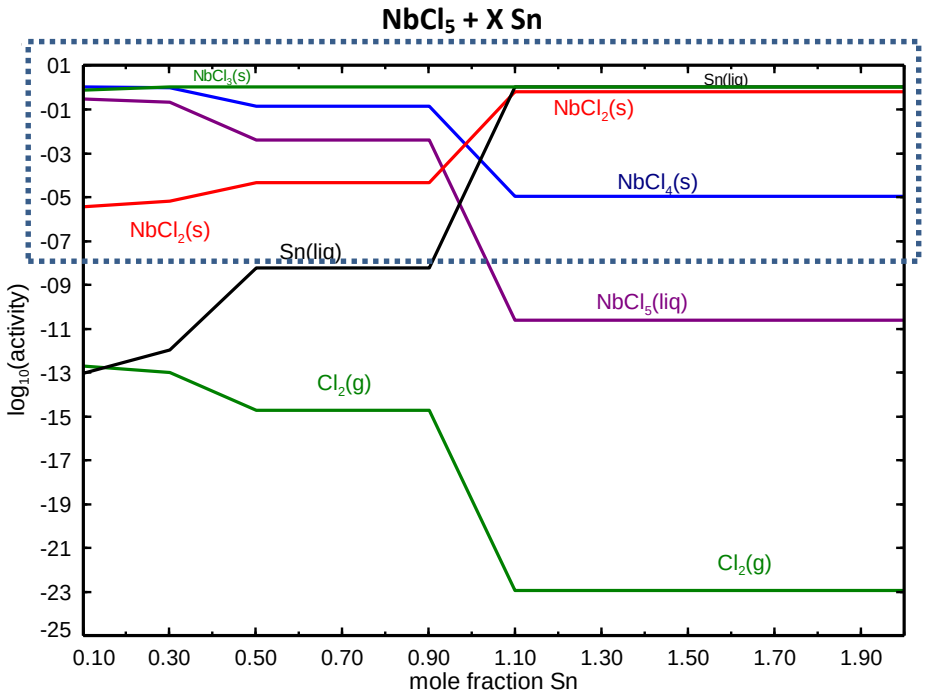

(a)

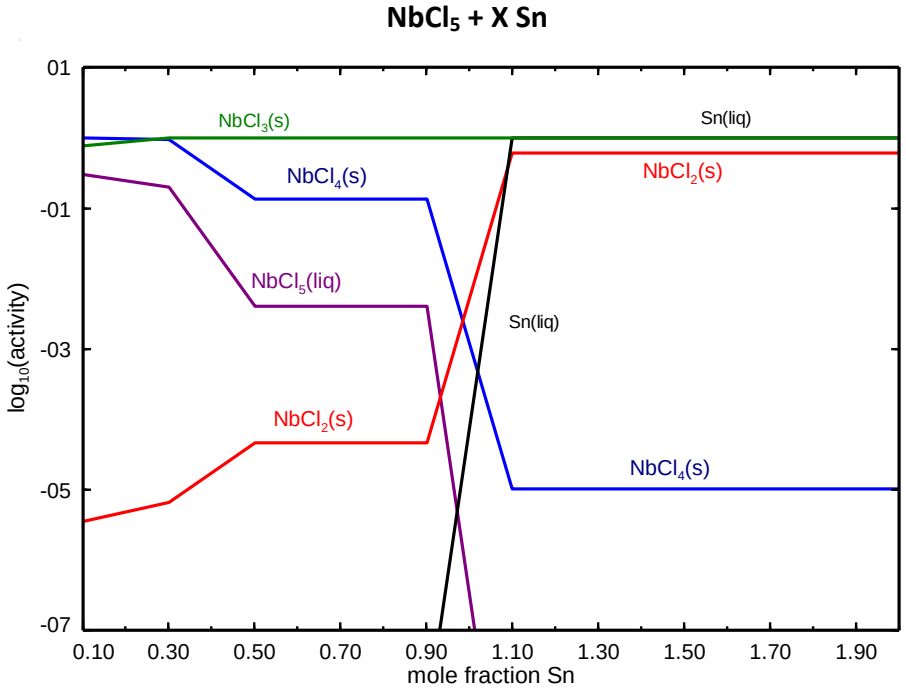

(b)

Figure 5.29 (a) Thermodynamic calculations of adding different mole fractions of Sn to $NbCl_5$ at 300˚C, (b) Higher magnification of (a).

Figure 5.25 shows that the Sn-$SnCl_2$ curve intersects the $NbCl_2$-$NbCl_3$ curve at 450˚C. Therefore, there are equal amounts of $NbCl_2$ and $NbCl_3$ in the mixtures at this temperature. In addition, Figure 5.29 (b) shows that the stable phases are $NbCl_3$ and $NbCl_2$ for 1.3 mole fraction Sn. Therefore, it is expected that this mixture have high electrical conductivity. However, the electrical conductivity of the mixtures at 1.3 mole fraction Sn (Figure 5.28) shows that Sn decreases the conductivity of the $NbCl_5$ and $NaAlCl_4$ mixtures. In fact, this discrepancy can be due to any small deviation in FactSage database.

Another reducing agent that is examined is copper. Figure 5.25 shows that ΔG° for chlorination of Cu is small enough to reduce $NbCl_5$. The effect on electrical conductivity of adding 2.5 moles Cu to one mole of the $NbCl_5$ salt while the $NbCl_5$:$NaAlCl_4$ ratio is equal to 0.3 was measured (Figure 5.28). In order to simplify, the above mixture is defined as Nb:Na=0.3, Cu:Nb=2.5 in this figure. The results show that Cu decreases the conductivity of the $NbCl_5$ and $NaAlCl_4$ mixtures and it slightly increases the conductivity of pure $NaAlCl_4$.

Figure 5.30 shows the trend for phase stability with addition of copper to $NbCl_5$ at 300˚C. The mixtures contain $NbCl_3$ and $NbCl_4$ for Cu concentrations up to 2 mole fraction. By increasing the amount of copper the chlorine pressure decreases to 10^{-19} atm and the activity of $NbCl_4$ decreases. Therefore, the amount of available Nb^{4+} in the solution decreases which reduces the electron hopping probability.

Moreover, copper is solid at 300˚C and does not dissolve in the salt; therefore, it blocks the capillary U-shaped cell and makes the conductivity measurements not reliable.

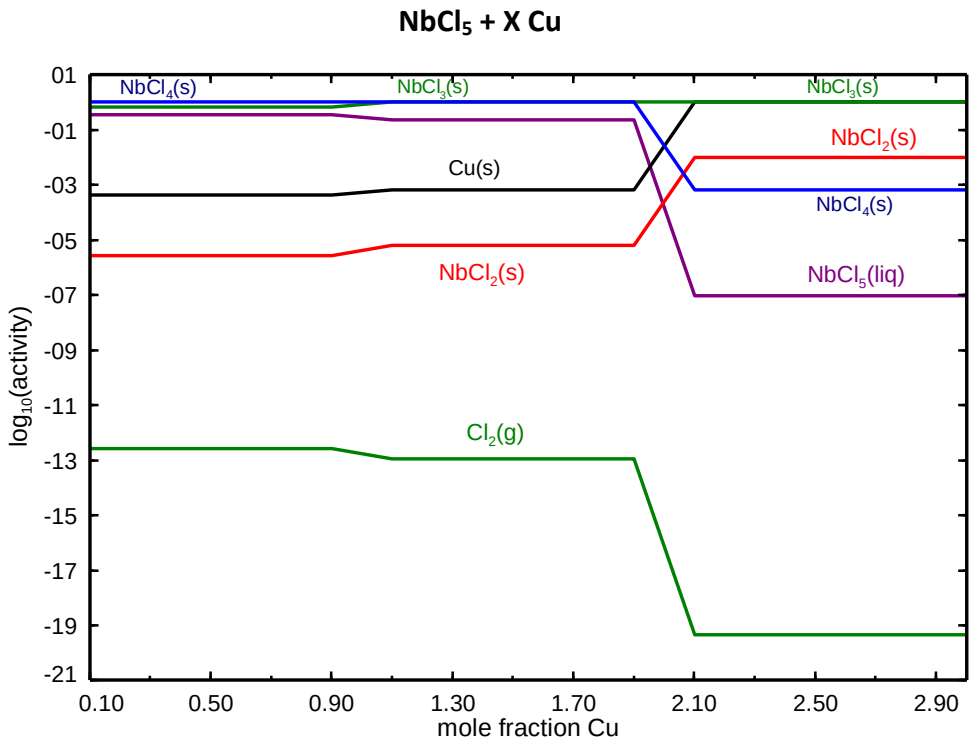

Figure 5.30 Calculated activities of various species when Cu is added to $NbCl_5$ at 300˚C.

Unlike copper, bismuth metal is liquid at the ZEBRA cell operating temperature (Tm= 271.4˚C) and thus, does not block the capillary tube. Since, during conductivity measurements, the molten Bi metal can easily flow and take the shape of the conductance cell. By shaking the cell slightly, the liquid salt mixture can wet the

remaining Bi metal surface inside the capillary and maintain the current path within the tube. Moreover, Figure 5.25 shows that the ΔG° of the Bi chlorination is lower than $NbCl_4$ and therefore, Bi metal can reduce the chlorine pressure of niobium chlorides and stabilize $NbCl_3$ and $NbCl_4$ within the mixture.

As the highest conductivity values was obtained by adding 30 mole % $NbCl_5$ to $NaAlCl_4$ (Figure 5.23 and 5.24), different concentrations of Bi were added to 30 mole % $NbCl_5$ and the conductivity of the mixtures was measured versus temperature (Figure 5.28).

For the purposes of the experiments, the following three composition parameters m, n and t were defined in following patterns.

$$m = \frac{X_{Bi}}{X_{Bi}+X_{NbCl_5}} \quad (5.4)$$

$$n = \frac{X_{NbCl_5}}{X_{NbCl_5}+X_{NaAlCl_4}} \quad (5.5)$$

$$t = 1 - X_{NaAlCl_4} = X_{Bi} + X_{NbCl_5} \quad (5.6)$$

The n value is fixed at 0.3 and the compositions (X) are in mole percent.

Figure 5.28 shows that by adding 0.2 mole fraction Bi to the $NbCl_5$ + $NaAlCl_4$ mixture (Nb:Na=0.3, Bi:Nb=0.2), the conductivity of the liquid electrolyte approximately doubles between 190 and 500˚C.

Figure 5.31 shows the effect of addition of Bi on total conductivity of the 30 mole % $NbCl_5$ - $NaAlCl_4$ mixture at 300˚C. The highest conductivity appears at 0.2 mole fraction Bi (Nb:Na= 0.3, Bi:Nb= 0.2) and the lowest one is for 0.75 mole fraction Bi (Nb:Na= 0.3, Bi:Nb= 0.75).

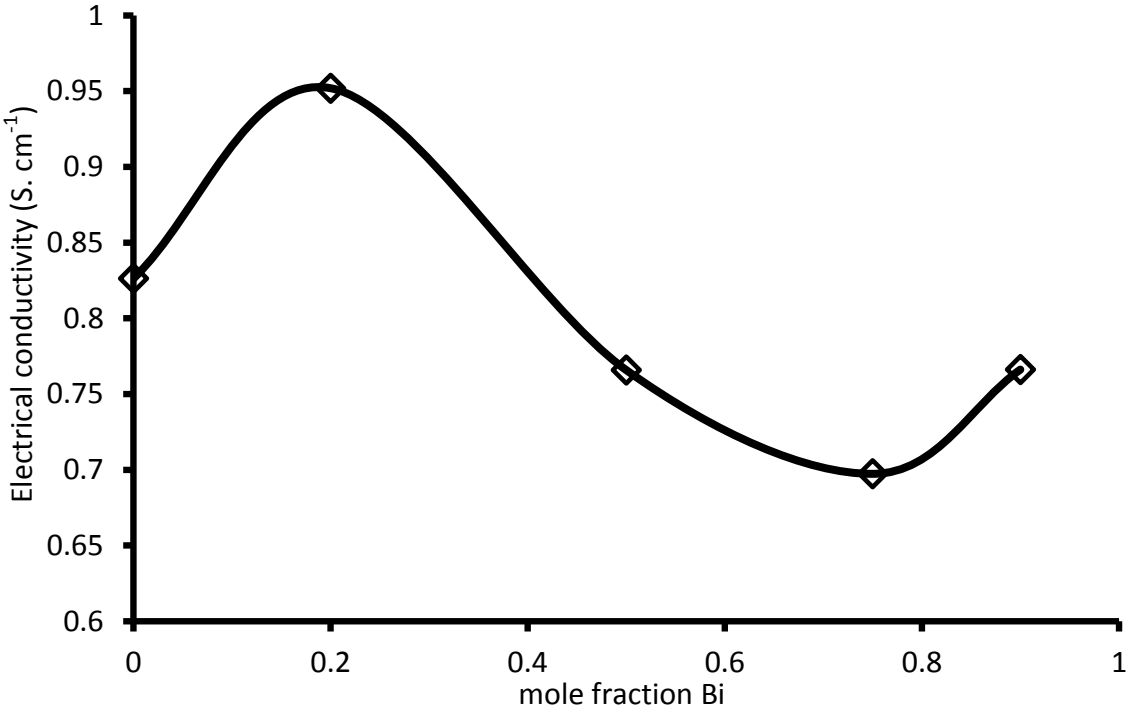

Figure 5.31 The effect of different concentrations of Bi addition to 30 mole % $NbCl_5$- $NaAlCl_4$ mixture at 300˚C.

The conductivity values in Figure 5.28 and 5.31 depict the total electrical conductivities, i. e., ionic and electronic. In order to find out the contribution of electrons to total conductivity the electronic conductivity of the above mixtures was measured. In this regard, a potential bias is applied to the two electrode cell with 1 mV/s scan rate and the measured current at each voltage is plotted versus potential.

Figure 5.32 shows the I-E curve for pure $NaAlCl_4$ and different mixtures of Bi+ $NbCl_5$+ $NaAlCl_4$.

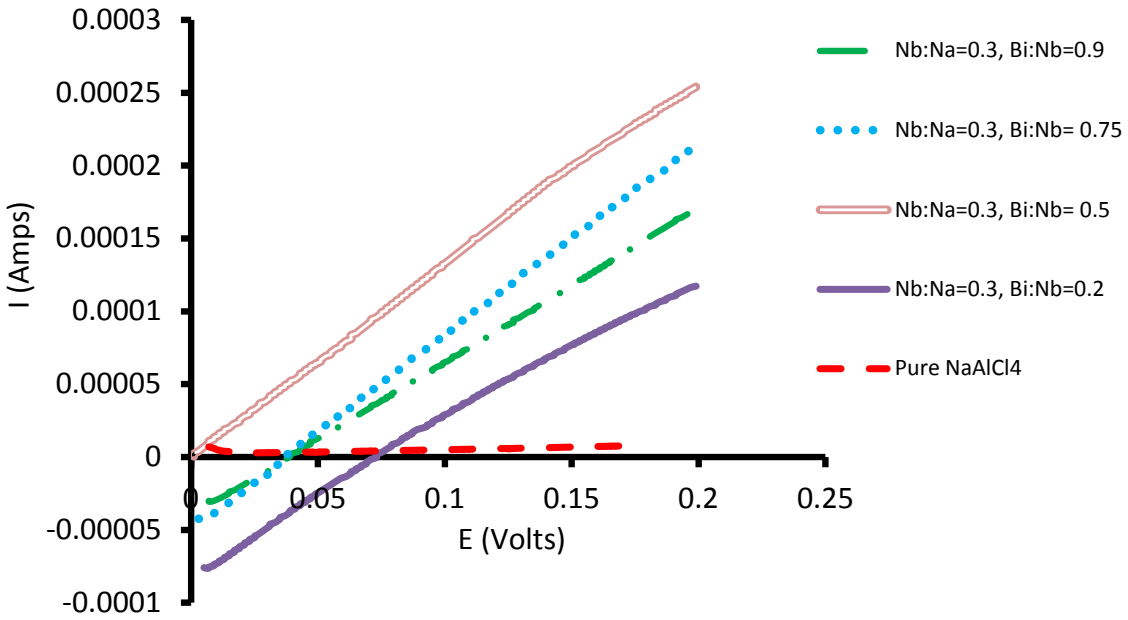

Figure 5.32 The I-E curve for different mixtures of Bi + $NbCl_5$ + $NaAlCl_4$. The scan rate is 1 mV/s and the range of voltage is 0-0.2 V vs. Reference.

Based on Ohm's law the slope of the above curve is electronic conductance, $k = \frac{I}{V}$. Knowing the cell constant and using equation 2.24, one can determine the electronic conductivity (σ_e). However, some of the curves in Figure 5.32 do not pass through zero on the current axis and this deviation can be explained as follows:

1- During conductivity measurements, the cell and one side of the electrical wires were positioned at high temperatures, whereas, the other side of wires

was connected to potentiostat at room temperatures. Based on the Seebeck effect, the temperature difference between the two ends of the wires generates current that flows through the wires and this causes some deviations in electronic conductivity measurements.

2- During measurements, some of the liquid Bi metal remained inside the conductance cell and formed a double layer structure. The Bi metal introduced a new interface within the liquid electrolyte. Based on the surplus or deficit of electron in the surface atomic layer of the metal, the metal side of the interface is charged. This charge can form a strong chemical bonding with the opposite charges of the liquid side of the interface. This is known as first layer. The second layer forms due to the coulombic force between ions with the opposite charge of the first layer and the surface charge [105]. In fact, the presence of double layer at the liquid metal and liquid electrolyte interface can act like a capacitance. This interface introduces a new semicircle at medium frequency range (R_2) in the impedance plot (Figure 5.33).

In order to calibrate the electronic conductivity measurements, the resistance of the interface (R_2) should be subtracted from the total electronic resistance (R_{DC}) that is obtained from DC measurements (equation 5.7).

$$R_{electronic} = R_{DC} - R_2 \quad (5.7)$$

Table 5.4 shows the electronic conductivity values for the pure $NaAlCl_4$ and the four compositions in Figure 5.32.

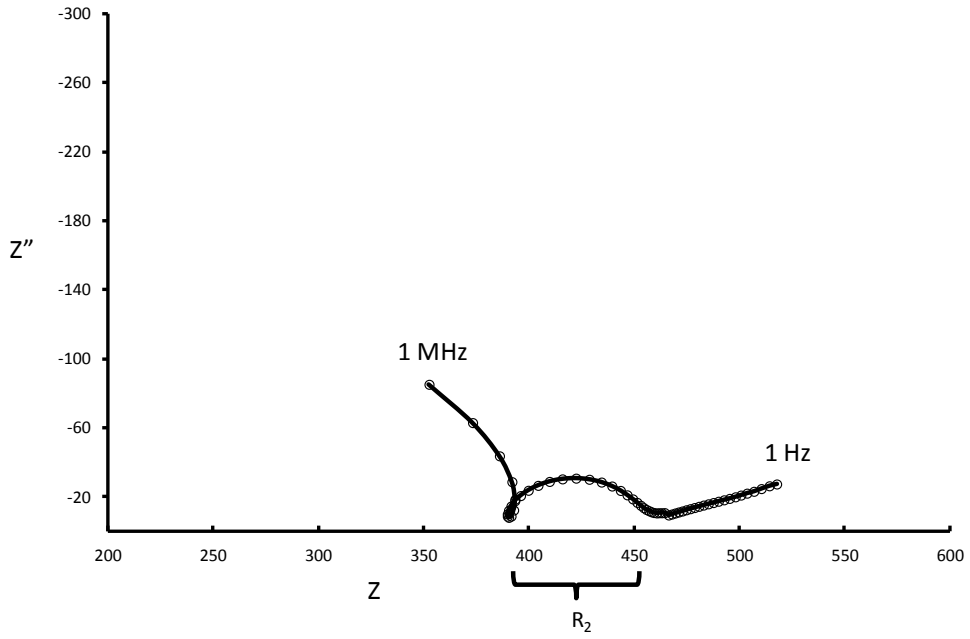

Figure 5.33 Impedance plot for 0.2 mole Bi + $NbCl_5$ + $NaAlCl_4$.

Table 5.4 Electronic conductivities of different mixtures at 300˚C.

Composition	Electronic conductivity (S/cm)	Standard deviations
Pure $NaAlCl_4$	0.011	0.0023
Nb:Na=0.3, Bi:Nb=0.2	0.53	0.017
Nb:Na=0.3, Bi:Nb=0.5	0.57	0.013
Nb:Na=0.3, Bi:Nb=0.75	0.57	0.027
Nb:Na=0.3, Bi:Nb=0.9	0.50	0.032

For better illustration, the electronic conductivity values in Table 5.4 were plotted in Figure 5.34.

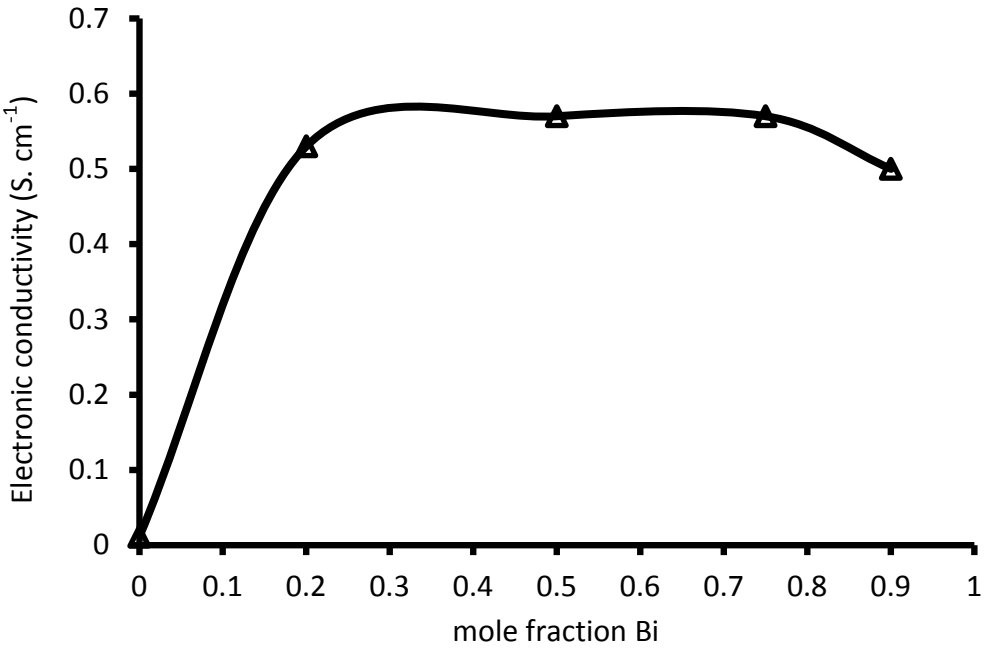

Figure 5.34 The electronic conductivity of adding different concentrations of Bi to $NbCl_5$ and $NaAlCl_4$ mixtures at 300˚C.

As mentioned before, the slope of pure $NaAlCl_4$ curve in Figure 5.32 is approximately zero which points out that it is only an ionic conductor. The positive slope of the curves in Figure 5.32 indicates that adding different concentrations of Bi has a significant contribution to electronic conductivity.

In general, the electronic conductivity values follow an increasing trend with Bi addition (Figure 5.34). The electronic conductivity is almost zero for pure $NaAlCl_4$ and it reaches 0.6 S/cm for Nb:Na=0.3, Bi:Nb=0.5 and Nb:Na=0.3, Bi:Nb=0.75.

Thermodynamic calculation of adding different mole fractions of Bi to $NbCl_5$ at 300˚C is shown in Figure 5.35 (a). For better accuracy, the calculations around zero value of logarithms of activity are plotted at higher magnification in Figure 5.35 (b).

Figure 5.35 (a) shows that the chlorine pressure gradually decreases by increasing the amount of Bi and it reaches around 10^{-16} atm for Bi concentrations more than 0.7 mole fraction. Up to 0.5 mole fraction Bi the most stable phases are $NbCl_3$ and $NbCl_4$. The simultaneous formation of the above phases increases the probability of electrons hopping. Therefore, the increase in electronic conductivity can be attributed to the electron exchange between different valence states of Nb ions (Nb^{3+} and Nb^{4+}) in the mixture. At Bi concentrations more than 0.5 mole fraction the amount of $NbCl_4$ phase in the solution decreases in the mixture and thus the electronic conductivity of the solution decreases too. It should be mentioned that measured conductivity cannot be explained only by thermodynamic equilibria especially at Bi concentrations more than 0.75 mole fraction in Figure 5.31.

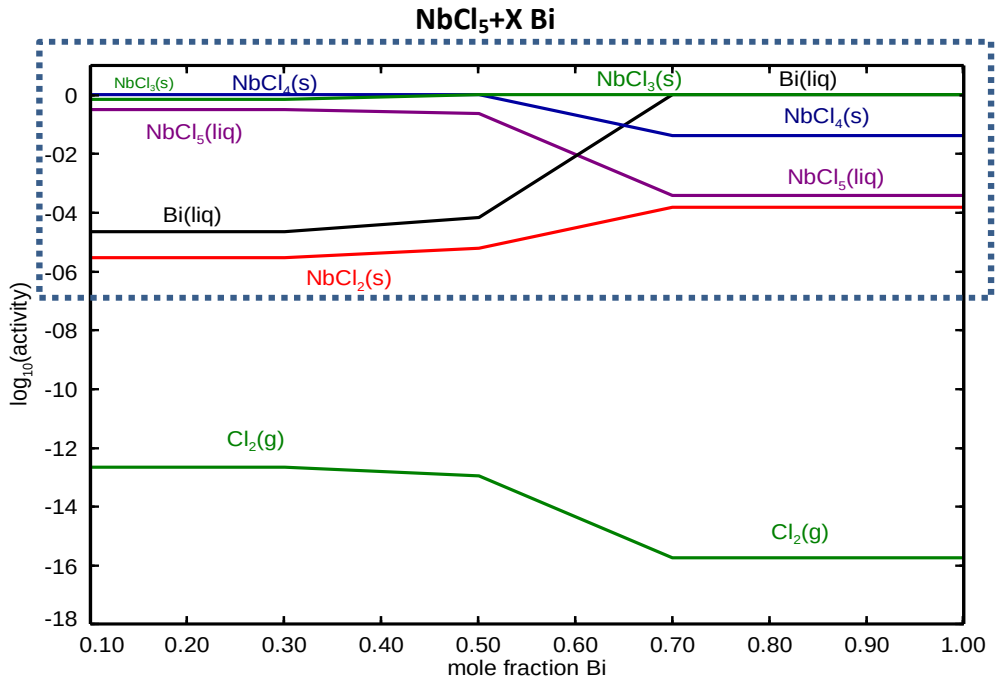

(a)

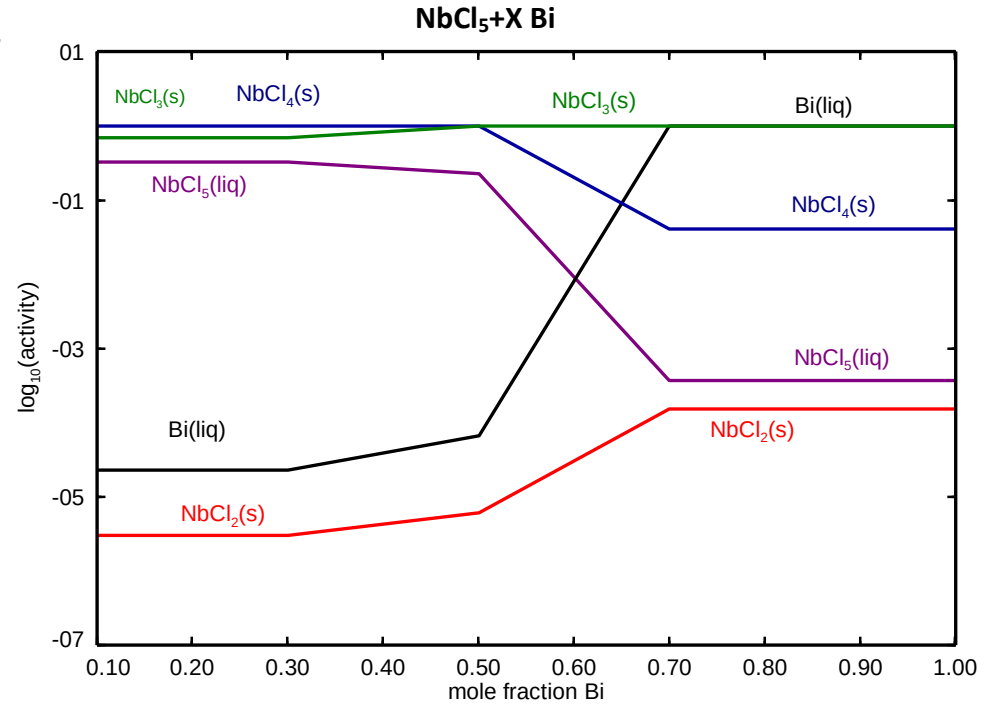

(b)

Figure 5.35 Phases present at different concentrations of Bi in the $NbCl_5$ at 300˚C.

Comparing the electronic conductivities with total conductivities of the mixtures reveals that the electronic conductivity values change within a narrow range (between 0.5 and 0.57 S/cm); however, the total conductivity values fluctuating within a wider range (0.69 S/cm for 0.75 mole fraction Bi and 0.95 S/cm for 0.2 mole fraction Bi) (Figure 5.36). Therefore, the difference in the total conductivity values is attributed to the difference in ionic conductivity of the mixtures.

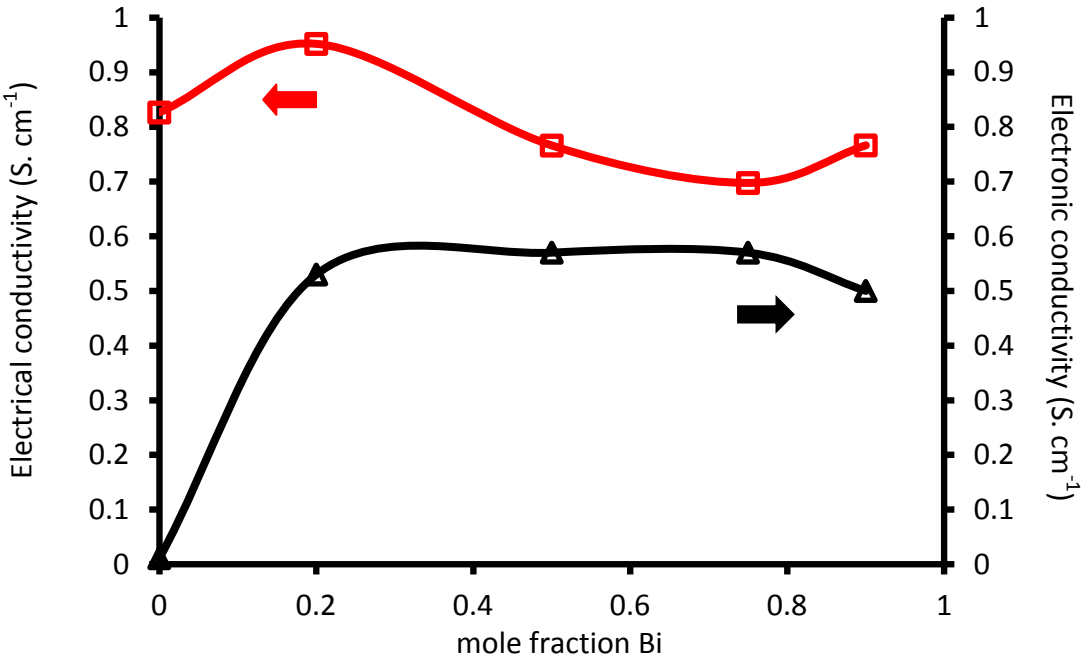

Figure 5.36 Comparing the total conductivity with the electronic conductivity of Bi+ $NbCl_5$+ $NaAlCl_4$ mixtures at 300˚C.

Huber et al. [102-103] reported that $NbCl_5$ has a large solubility in alkali chloride melts. However, the solubility of $NbCl_3$ is very low [103-104]. In addition, thermodynamic calculations show that at Bi concentrations more than 0.5 mole fraction $NbCl_3$ is the only stable phase. As a result, the presence of insoluble $NbCl_3$ as the only stable phase at Bi concentrations more than 0.5 mole fraction may increase the viscosity and decrease the ionic conductivity.

5.3.1 Effect of NaF and Na_2S on electronic conductivity of the $NaAlCl_4$

NaF and sulfur are added to the ZEBRA cell to improve its properties. Section 2.5.2 and 2.7 explain their role in improving energy and capacity of the ZEBRA cell, respectively. However, the effect of these additives on the conductivity of the $NaAlCl_4$ has not been investigated. In this regard, different concentrations of the above additives were added to the $NaAlCl_4$ and the electrical conductivity was measured. As sulfur is not soluble in $NaAlCl_4$ [106], Na_2S salt was used instead of pure sulfur.

The electrical conductivity of adding different concentrations of NaF and Na_2S in mole fraction to $NaAlCl_4$ at 300˚C are shown in Figure 5.37 and 5.38, respectively.

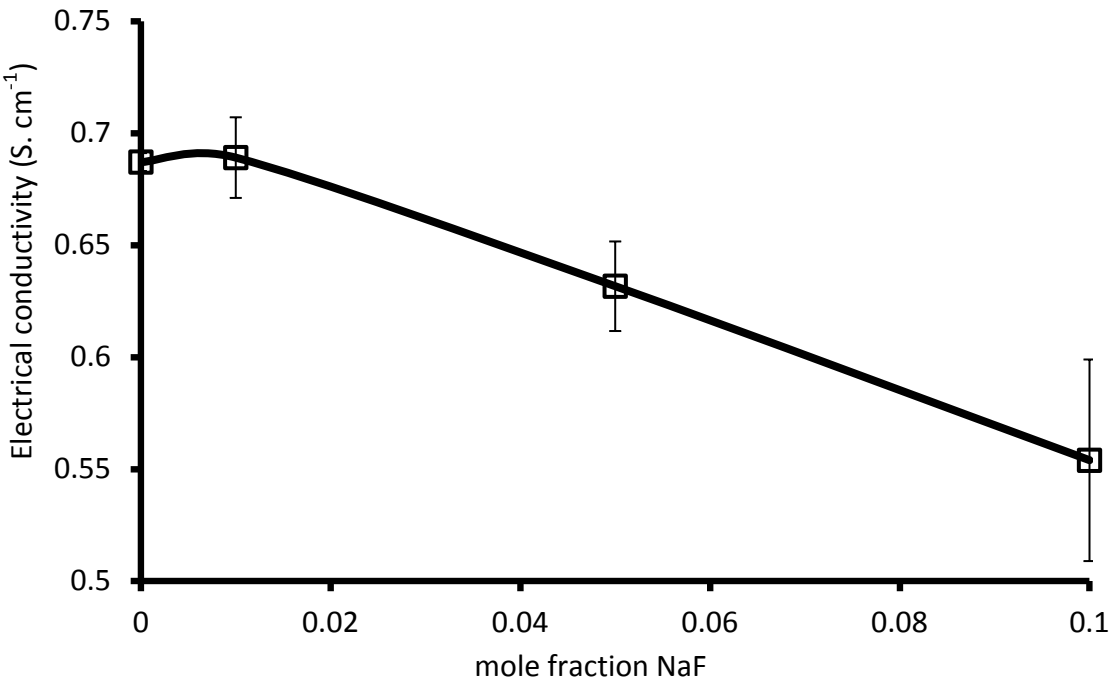

Figure 5.37 The electrical conductivity as a function of NaF addition to $NaAlCl_4$ at 300˚C.

Figure 5.37 shows that adding NaF up to 0.01 mole fraction does not have significant influence on the conductivity; however, increasing the amount of NaF more than 1 mole percent considerably decreases the electrical conductivity.

It is probable that NaF reacts with AlF_3 and forms Na_3AlF_6 in the mixture. Therefore, the decrease in conductivity at NaF concentrations more than 0.01 mole fraction might be attributed to the formation of Na_3AlF_6 in the mixture.

Furthermore, the electrical conductivity behavior of adding different concentrations of Na_2S to $NaAlCl_4$ is shown in Figure 5.38.

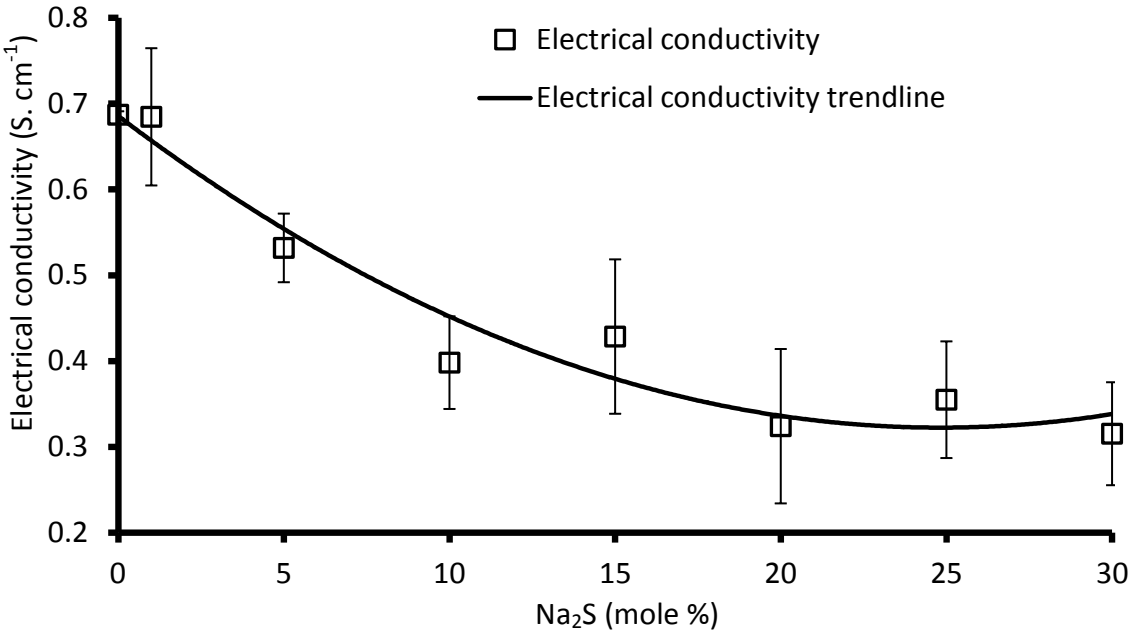

Figure 5.38 The electrical conductivity as a function of Na_2S addition to $NaAlCl_4$ at 300˚C.

By increasing the amount of Na_2S the conductivity of the mixture decreases. Similar to the Al_2S_3-$NaAlCl_4$ system (explained in section 2.11.4.2), the Na_2S can react with $NaAlCl_4$ molten salt and form aluminum chlorosulfides.

$$Na_2S + NaAlCl_4 \rightarrow NaAlSCl_2 + 2NaCl \quad (5.8)$$

The highly polymerized $NaAlSCl_2$ compound can dissolve in equimolar NaCl-$AlCl_3$ molten salt. Consequently, the decrease in conductivity with increasing Na_2S can be due to the formation of highly viscous $NaAlSCl_2$.

Moreover, the effect of the above mentioned additives on electronic conductivity of $NaAlCl_4$ was also investigated.

Figure 5.39 shows the I-E curve for different concentrations of Na_2S and 10% mole NaF at 300˚C. The results show that adding 10 mole percent NaF does not improve the electronic conductivity; however, this is not the case for Na_2S.

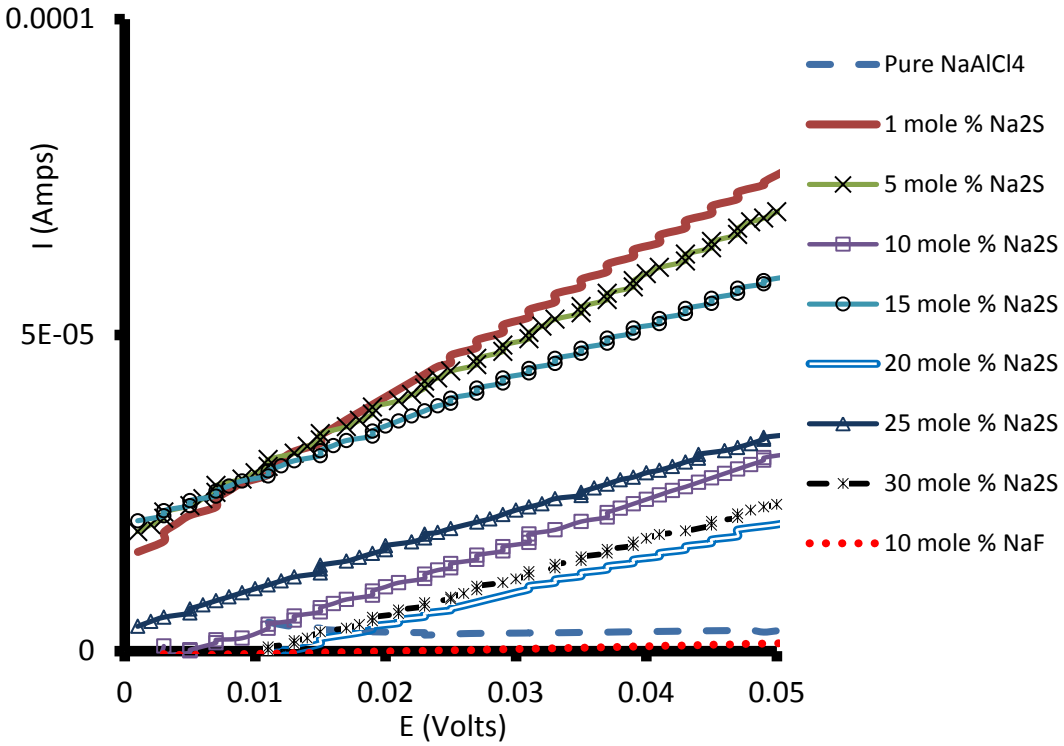

Figure 5.39 Effect of Na_2S and NaF additives on electronic conductivity of $NaAlCl_4$ at 300˚C.

To better illustrate, the electronic conductivity values with different concentrations of Na_2S in $NaAlCl_4$ at 300˚C is plotted in Figure 5.40. In this Figure the electrical conductivity and the electronic conductivity values are overlapped. As it is shown they both follow the same trend which means that Na_2S and $NaAlCl_4$ mixtures contribute only to electronic conductivity.

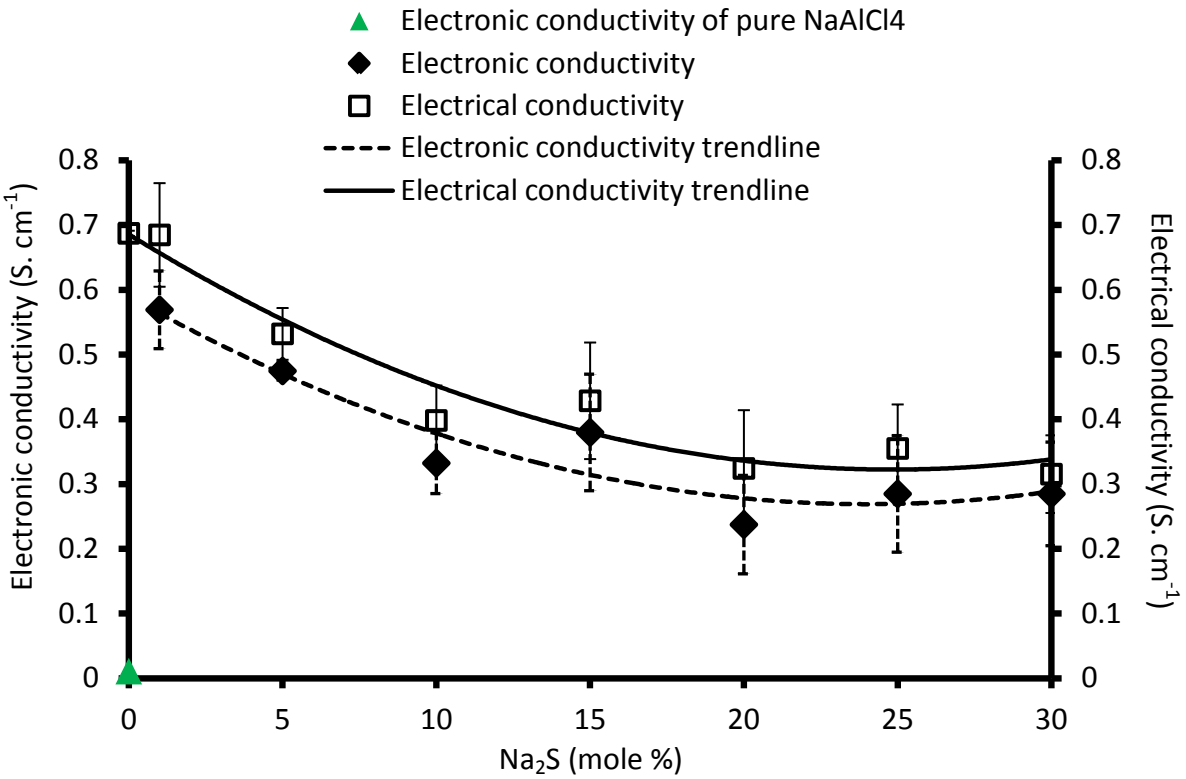

Figure 5.40 The electronic conductivity of Na_2S+$NaAlCl_4$ mixture (♦) and pure $NaAlCl_4$ (▲) overlapped with the electrical conductivity of Na_2S+$NaAlCl_4$ (□) mixture at 300˚C.

Comparing the electronic conductivity of the Na_2S+$NaAlCl_4$ mixtures with the electronic conductivity of pure $NaAlCl_4$ (▲ in Figure 5.40) shows that adding 1 mole % Na_2S to $NaAlCl_4$ increases the electronic conductivity from approximately zero for pure $NaAlCl_4$ to around 0.7 S/cm.

Moreover, it has been reported that the presence of $NaAlSCl_4$ in the chemistry of the sodium-nickel chloride cell improves the high current performance of the cell. The cathode composition, in which this compound is present in a range of from 0.3 wt % to

10 wt % based on the total weight of the cathode composition, can considerably improve the working capacity of the cell and reduce the degradation rate of the cell capacity [107].

6. CONCLUSIONS

The following points summarize the results obtained in this thesis:

1. Applying the vacuum distillation technique prior to SEM analysis is an effective way to remove a fraction of the $NaAlCl_4$, enough to expose the major components of the cathode.
2. SEM analysis revealed the morphology of different phases in ZEBRA cells such as $NiCl_2$, large Ni particles in aged cells, needle-like $FeCl_2$ crystals and Na_6FeCl_8.
3. XRD and EDS analysis have confirmed the formation of different phases in the ZEBRA cell cathode including NaCl, Na_6FeCl_8, Ni, $NaAlCl_4$, $FeNi_3$, $NiAl_2Cl_8$.
4. Microstructural details observed in the cathode during post-mortem analysis may be artifacts from transformations during cooling and not present during cell operation. For example, NaCl crystals could precipitate from the non-stoichiometric liquid salt.
5. FactSage thermodynamic software provided an appropriate database for modeling ZEBRA chemistry. For instance, $NiAl_2Cl_8$ crystals identified by XRD are evidence of an overcharged cell; Ni_3Al formation indicates an overdischarge condition. Both of these results are well illustrated by thermodynamic analysis based on available molten salt solution models.

6. Thermal arrests during battery cycling can introduce non-equilibrium conditions to individual cells and it is recommended that special care be exercised following thermal shutdowns.
7. The isolated Ni particles that are revealed by FIB analysis are surrounded only by ionically conducting salt. These passive Ni particles cause an increase in resistance and thus, capacity loss.
8. It is proposed that a mixed ionic-electronic conducting electrolyte will allow isolated Ni particles to participate in the cell reaction and therefore, avoid capacity loss.
9. A special conductance cell was designed to measure the conductivity of hygroscopic and volatile $NaAlCl_4$ at high temperatures. The cell was made of two parts. The first part was a U-shaped capillary cell with high cell constant which was made of quartz and the second part was two tungsten electrodes that were sealed off to two Pyrex tubes via uranium glass. After loading the U-shaped tube with salt powder, the two parts were joined to each other by O-ring clamps and made a closed volume cell.

   An inlet and outlet valve were attached to the Pyrex tube. By purging the cell with argon gas, all experiments could be performed outside the glovebox.
10. The conductivity of pure $NaAlCl_4$ was measured between 150˚C and 400˚C and the results show an increasing trend with temperature. The conductivity data

were compared with the literature. It was seen that the previous data had a scatter up to approximately 10 % and were in accord with our results at this level of precision. The deviations among the results may be due to impurities and inaccuracies in the composition of the melt.

11. The solidification point of pure $NaAlCl_4$ was observed to be near 160˚C by conductivity measurements.
12. Niobium metal is a promising additive to introduce conductivity as it has multiple valence states, namely, Nb^{2+}, Nb^{3+}, Nb^{4+}, and Nb^{5+}. Moreover, niobium chloride species are stable at chlorine pressures fixed by Ni-$NiCl_2$ and they do not react with other components of the ZEBRA cell cathode. Therefore, different concentrations of $NbCl_5$ were added to $NaAlCl_4$ electrolyte in an attempt to make it a mixed conductor. Among different concentrations, adding 30 mole percent $NbCl_5$ increased the conductivity of the electrolyte up to 20 % between 250˚C and 436˚C. The increase in conductivity can be partly attributed to decreased viscosity of the molten salt, judging from the observed fluidity.
13. Adding $NbCl_5$ to $NaAlCl_4$ can slightly increase the conductivity due to the fully saturated electron structure of Nb in $NbCl_5$. All electrons in $NbCl_5$ compound are bounded to chlorine and therefore, electron transfer is not possible.
14. The effect of different reducing agents on decreasing the chlorine pressure of $NbCl_5$ was determined by FactSage software. Ni-$NiCl_2$, Cu-CuCl, Sn-$SnCl_2$, and Bi-

$BiCl_3$ reactions have a ΔG° of formation more negative than that of $NbCl_3$-$NbCl_4$ and hence, Ni, Cu, Sn, and Bi can act as reducing agents.

15. At the chlorine pressure of the ZEBRA cathode which is fixed at $P_{Cl2}=1.48X10^{-20}$ atm by the Ni-$NiCl_2$ equilibrium, the most stable phases are $NbCl_3$ and $NbCl_2$. Therefore, Ni is a good candidate for reducing chlorine pressure. However, it is solid at operating temperature (300˚C) and it blocks the current path inside the capillary tube. The chlorine pressure of Bi-$BiCl_3$ at 300˚C is near $P_{Cl2}=10^{-16}$ (close to the Ni-$NiCl_2$ pressure), and at this pressure different species of niobium chloride ($NbCl_3$ and $NbCl_4$) are stable in the mixture. Therefore, Bi metal was used in the experiments as a surrogate for Ni.
16. Among different reducing agents, Bi is most promising. By adding 0.2 mole fraction Bi to $NbCl_5$ + $NaAlCl_4$ molten salt mixture (Nb:Na=0.3, Bi:Nb=0.2), the conductivity of the liquid electrolyte approximately doubles between 190 and 500˚C. Moreover, dc measurements confirm the electronic conductivity under these conditions. The electronic conductivity is almost zero for pure $NaAlCl_4$ and it reaches 0.6 $S.cm^{-1}$ for the Nb:Na=0.3, and Bi:Nb=0.5 mixture. Thermodynamic calculation predicts the presence of $NbCl_3$ and $NbCl_4$ at Bi concentrations up to 0.5 mole fraction. The highest electronic conductivity is due to simultaneous formation of $NbCl_3$ and $NbCl_4$ which can facilitate the electron exchange.

17. The ionic conductivity of pure $NaAlCl_4$ is 0.68 S. cm^{-1}. In order to have an electrochemical cell that works effectively, the electronic conductivity inside the cathode should not be less than the ionic conductivity. In the ZEBRA cell, the electronic conductivity is provided by interconnected solid Ni inside the cathode; however, it is well beyond the amount needed for a ZEBRA cell. Moreover, Ni metal is the most expensive component of the ZEBRA cell but, as shown by FIB analysis, many of the Ni particles lose contact and do not participate in the reaction. In case of having a mixed ionic-electronic conducting electrolyte with the electronic conductivity value in the range of the ionic conductivity of the electrolyte, the amount of Ni consumption in ZEBRA cell construction can decrease and consequently, the ZEBRA cell cost will be reduced.
18. It was found that the amount of NaF and Na_2S that are already added to the ZEBRA cell to improve its properties play an important role. Adding more than 1 mole percent NaF and Na_2S to the electrolyte can significantly decrease the conductivity of the electrolyte, probably due to the formation of $NaAlF_6$ and $NaAlSCl_2$, respectively.

7. REFERENCES

1- H. Bo¨hm, G. Beyermann, “ZEBRA batteries, enhanced power by doping”, Journal of Power Sources, 84, 1999, P. 270–274.

2- J. Prakash, L. Redey , and D. R. Vissers, “Morphological Considerations of The Nickel Chloride Electrodes for ZEBRA Batteries”, Journal of Power Sources, 84, (1999), p. 63–69.

3- E. C. Kluiters, D. Schmal, W. R. ter Veen, and K. J.C.M. Posthumus, “Testing of Sodium/Nickel Chloride (ZEBRA) battery for electric propulsion of ships and vehicles”, Journal of Power Sources, 80, 1999, p. 261–264.

4- M. A. Vallance, and R. E. White, “High-Temperature Sodium / Metal Chloride Storage Battery”, Excerpt from the Proceedings of the COMSOL Conference Boston 2008.

5- N. D. Nicholson, D. S. Demott, and R. Hutchings, “Characterization of The Positive Electrode in Sodium-Metal Chloride (ZEBRA) cells”, Power Sources 12, Proceeding in 16 th International Power Sources Symposium Committee, paper No. 37, (1988), p. 549-561.

6- Battery technologies, The sodium Nickel chloride ZEBRA battery, Meridian International Research, (2005), p. 104-112.

7- R. C. Galloway, S. Haslam, “The ZEBRA Electric Vehicle Battery: Power and Energy Improvements”, Journal of Power Sources, 80, (1999), p. 164–170.

8- J.L. Sudworth, “The Sodium/$NiCl_2$ (ZEBRA) Battery”, Journal of Power Sources, 100, (2001), p. 149-163.

9- R. C. Galloway, R. J. Bones, D. A. Teagle, and M. L. Wright, Patent 4. 529. 676. (1985).

10- R. C. Galloway, “A Sodium/Beta-Alumina/Nickel Chloride Secondary Cell”, Journal of the Electrochemical Society: Accelerated, Brief Communication, Vol. 134, No. 1, Jan. (1987), p. 256-257.

11- P. T. Moseley, R. J. Bones, D. A. Teagle, B. A. Bellamy, and R. W. M. Howes, “Stability of Beta Alumina Electrolyte in Sodium / $FeCl_2$ (ZEBRA) Cells”, Journal of Electrochemical Society, vol. 136, No.5, May (1989), p. 1361-1368.

12- C. H. Dustmann, “Advances in ZEBRA Batteries”, Journal of Power Sources, 127, (2004), p. 85-92.

13- J. L. Sudworth, A. R. Tilley, “The Sodium Sulfur Battery”, Chapman and Hall Ltd, (1985).

14- K. M. Abraham and J. E. Elliot, “Moderate Temperature Sodium Cells,V. Discharge Reactions and Rechargeability of NiS and NiS2 Positive Electrodes in Molten”, Journal of The Electrochemical Society: Electrochemical Science and Technology, Oct. (1984), p. 2211-2217.

15- R. J. Bones, D. A. Teagle, and S. D. Brooker, “Fabrication of discharge positive electrode for sodium-metal chloride (ZEBRA) battery cells”, Power Sources 12, Proceeding in 16 th International Power Sources Symposium Committee, paper No. 36, (1988), p. 537-547.

16- R. J. Bones, J. Coetzer, R. C. Galloway, and D. A. Teagle, “A Sodium/Iron Chloride Cell with a Beta Alumina Electrolyte”, Journal of the Electrochemical Society: Electrochemical Science and Technology, Oct. (1987), p. 2379-2382.

17- R. J. Bones, J. Coetzer, R. C. Galloway, and D. A. Teagle, “A Sodium Iron Chloride Cell with a Beta Alumina Electrolyte, The Electrochemical Society, Extended Abstract, Abstract No. 763, Vol. 86, 2, San Diego, CA, Oct. (1986), p. 1122.

18- R. J. Bones, D. A. Teagle, S. D. Brooker, and F. L. Cullen, “Development of a Ni, NiCl2 Positive Electrode for a Liquid Sodium (ZEBRA) Battery Cell”, Journal of the Electrochemical Society, Vol. 136, No. 5, May (1989), p. 1274-1277.

19- J.L Sudworth, “High Temperature Battery System”, Philosophical Transactions of the Royal Society Lond. A., 354, (1996), p.1595-1612.

20- K. Kronsbein, “Investigatio and Modeling of the ZEBRA System to Optimize State of Charge Detection”, Thesis, Institut fur Werkstoffe der Elektrotechnik, Karlsruhe Institue für Technologie, May (2004).

21- H. Bloom, W. A. Benjamin, “The Chemistry of Molten Salts; an Introduction to the Physical and Inorganic Chemistry of Molten Salts and Salt Vapors”, INC. New York Amsterdam, (1967).

22- H. A. Hjuler, R. W. Berg, K. Zachariassen, and N. J. Bjerrum, “Specific Conductivity of NaCl-$AlCl_3$ and NaCl-$AlCl_3$-Al_2S_3 Melts”, Journal of Chemical and Engineering Data, 30, 2, (1985), p. 203-208.

23- N. C. Baenziger, “The Crystal Structure of $NaAlCl_4$”, Acta Chrystallographica, 4, (1951), p. 216-219.

24- W. WEPPNER and R.A. HUGGINS, “Ionic Conductivity of Alkali Metal Chloroaluminates”, Physics Letters, 58A, 4, 6 September (1976).

25- M. G. Macmillan, “Electrical Conductivity of the Systems $NaAlCl_4$, and NaCl(s)/$NaAlCl_4$, in the Range 100-200°C”, Journal of the Chemical Society, Faraday Transactions, 91, 18, (1995), p. 3157-3161.

26- D. Trickett, “Current Status of Health and Safety Issues of Sodium/Metal Chloride (ZEBRA) Batteries”, National Renewable Energy Laboratory, NREL/TP-460-25553, November (1998).

27- R. M. Dell, R. J. Bones, “High Temperature Sodium Batteries”, A Comparative Review, Bulletin of Electrochemistry, 4(4), Apr. (1988), p.319-326.

28- I. Bloom, P. A. Nelson, L. Redey, S. K. Orth, C. L. Hammer, R. S. Skocypec, D. W. Dees, M. C. Hash, and D. R. Vissers, “Design Considerations for the Development of

Advanced Sodium/Metal-Chloride Cells", proceedings of the 25th Inter Society Energy Commission Energy Conference, Reno, NV, August (1990), Vol. 3, p. 341-347.

29- J. Rijssenbeek, Y. Gao. Z. Zhong, M. Croft, N. Jisrawi, A. Ignatov, and T. Tsakalakos, "In situ X-ray diffraction of prototype sodium metal halide cells: Time and space electrochemical profiling", Journal of Power Sources, 196, (2001), p.2332-2339.

30- B. C. Knutz, H. A. Hjuler, R. W. Berg, and N. J. Bjerrum, "Mechanism of Reaction in $NaAlCl_4$ Molten Salt Batteries with Nickel Felt Cathodes and Aluminum Anodes I. Modeling of the Battery Properties at Thermodynamic Equilibrium", Journal of the Electrochemistry Society, Vol. 140, No. 12, Dec.(1993), p. 3374-3379.

31- K. T. Adendorff and M. M. Thackeray, "The Crystal Chemistry of the $Na/FeCl_2$ Battery", Journal of the Electrochemical Society: Electrochemical Science and Technology, Vol. 135, No. 9, Sep. (1988), p. 2121-2123.

32- J. Coetzer, G. D. Wald, and S. W. Orchard, "Mechanism of the Cathode Reaction in Sodium-Ferrous Chloride Secondary Cells", Journal of the Applied Electrochemistry, 23, (1993), p. 790-800.

33- J. Prakash, L. Redey, and D. R. Vissers, "Electrochemical Behavior of Non Porous $Ni/NiCl_2$ Electrodes in Chloroaluminate Melts", Journal of the Electrochemical Society, 147, 2, (2000), p. 502-507.

34- C. H. Dustmann and R. Tilley "Power Improved ZEBRA Battery for Zero Emission Vehicles", Society of Automotive Engineers, Vol. 1156, (1996), p. 113-118.

35- J. Prakash, L. Redey, and D. R. Vissers, “Corrosion Studies of Nickel-200 in High-Temperature ZEBRA Batteries at 300°C”, Letter/Corrosion Science, 41, (1999), p. 2075-2082.

36- T. M. O’Sullivan, C. M. Bingham and R. E. Clark, “Zebra Battery Technologies for the All Electric Smart Car”, SPEEDAM 2006, International Symposium on Power Electronics, Electrical Drives, Automation and Motion.

37- J. Coetzer, J. L. Sudworth, “A Second Generation Sodium Nickel Chloride ZEBRA Cell”, EVS 13, Osaka, Oct. (1996).

38- J. Prakash, L. Redey, D. R. Vissers, and J. D. Ggruson, “Effect of Sodium Iodide Additive on the Electrochemical Performance of Sodium Nickel Chloride Cells”, Journal of the Applied Electrochemistry, 30, (2000), p.1229-1233.

39- B. C. Knutz, R. W. Berg, H. A. Hjuler, and N. J. Bjerrum “Mechanism of Reaction in $NaAlCl_4$ Molten Salt Batteries with Nickel Felt Cathodes and Aluminum Anodes II. Experimental Results and Comparison with Model Calculations”, Journal of the Electrochemical Society, Vol. 140, No. 12, Dec. (1993), p. 3380-3390.

40- L. Steinbock and C.-H. Dustmann, “Investigation of the Inner Structures of ZEBRA Cells with a Microtomograph”, Journal of the Electrochemical Society, 148 (2), (2001), p. A132-A136.

41- P.W. Atkins, “Physical Chemistry,” Third Edition, New York: W.H. Freeman, (1986), p. 663-671.

42- A.J. Bard and L.R. Faulkner, "Electrochemical Methods: Fundamentals and Applications" Wiley, New York, (1980), p. 64-67.

43- K. S. Mohandas, N. Sanil, Tom Mathews, and P. Rodriguez, "An Electrochemical Investigation of the Thermodynamic Properties of the NaCl-$AlCl_3$ System at Subliquidus Temperatures", Metallurgical and Materials Transactions B, 32B, August (2001), p. 669-677.

44- N. R. Carmichael and S. N. Flengas, "Molar Volume and Electrical Conductivity Measurements in the Ternary Molten Salt System NaCl-CsCl-$MnCl_2$, II.Elected Conductivities, Journal of the Electrochemical Society: Electrochemical Science and Technology, 126 (I2), Dec. (1979), p. 2104-2110.

45- G. J. Janz, R. P. T. Tomkins, C. B. Allen, J. R. Downey, G. L. Gardner, U. Krebs, and S. K. Singer, "Properties of Chlorides and Mixtures", Journal of Physical and Chemical Reference Data, 4 (4), (1975), p. 874-922.

46- H. Bloom and E. Heymann, "The Electric Conductivity and the Activation Energy of Ionic Migration of Molten Salts and Their Mixtures", Proceedings of the Royal Society of London, Series A, 188, (1947), p. 392-414.

47- H. A. Hjuler, R. W. Berg, K. Zachariassen, and N. J. Bjerrum, "Specific Conductivity of NaCl-$AlCl_3$ and NaCl-$AlCl_3$-Al_2S_3 Melts", Journal of Chemical and Engineering Data, 30(2), (1985), p. 203-208.

48- R. A. Carpio, F. C. Kibler, Jr., L. A. King, W. Brockner, K. TØrklep, H. A. Øye, "Density, Viscosity, and Electrical Conductivity of Acidic - LiCl - NaCl Melts", Journal of Physical Chememistry, 85, (1981), p. 31 -38.

49- R. C. Howie and D. W. Macmillan, "The Conductivity of The Binary Molten Salt System Aluminium Chloride/Sodium Chloride", Journal of Inorganic Nuclear and Chemistry, 33, (1971), p. 3681-3686.

50- K. S. Mohandas, N. Sanil and P. Rodriguez, "Development of a High Temperature Conductance Cell and Electrical Conductivity Measurements of $MAlCl_4$ (M=Li, Na and K) Melts", Mineral Processing and Extractive, Metallurgy (Transactions of the Institution of Mining and Metallurgy Section C), 115 (1), (2006), p. 25-30.

51- L. F. Grantham and S. J. Yosim, "Negative Temperature Coefficients of Electrical Conductance in Molten Salts", Journal of Chemical Physics, 45(4), 15 August (1966).

52- A. J. Darnell, W. A. McCollum, and S. J. Yosim, "The Electrical Conductivities of Molten Bismuth Chloride, Bismuth Bromide, and Bismuth Iodide at High Pressure", Journal of Physical Chemistry, 73 (12), (1969), p .4116 -24.

53- K. Fukushima, M. Hayakawa, Y. Iwadate, "Ionic Conductivity of Molten $GdCl_3$-NaCl and $GdCl_3$-KCl Systems", Journal of Alloys and Compounds, 245, (1906), p. 66-69.

54- C. R. Boston, S. J. YOSIM, and L. F. Grantham, "Electrical Conductivity of Aluminum Chloride Liquid and Supercritical Vapor", Journal of Chemical Physics, 51, (1969), p. 1669-1671.

55- P. L. Spedding, “The Basic Modes of Transport in Molten Salts”, Journal of Physical Chemistry, 76 (9), (1972), p. 1348-1351.

56- H. A. Levy and M. D. Danford, “Molten Salt Chemistry”, M. Blander, Ed. Interscience Publishers, Inc., New York, (1964) p. 109-125.

57- Y. Yamaguti, and S. Sisido, “Studies on the Electrolytic Conduction of Fused Salts”, Journal of the Chemical Society (Japan), 59 (1938), p. 1311-20.

58- I. A. Kryagova, Journal of General Chemistry of the U.S.S.R, 9, (1939), p. 2061-2066

59- R. H. Moss, “Doctoral Dissertation Series No. 12730”, University Microfilms, Ann Arbor, MI, (1955), p. 1-57.

60- R. Midorikawa, Journal of the Electrochemical Society (Japan), 24, (1956), p. 23-7.

61- V.A. Plotnikov and P.T. Kalita, Zh. Russ. Fiz. Khim. Obshch., 62 (1930), p. 2195.

62- K. Matiasovsky, p. Fellner, M. Chrenkova-Paucirova, G. Brautigam, H. Emons, Journal of Electrochimica Acta, 25, (1980), p. 195-200.

63- A. I. Gubanov, Soviet Physics-Technical Physics (English), 27, (1957), p. 2335.

64- L.G. Parent, S.G. Davison, and H. UEBA, “Electronic Theory of Molten Salts”, Journal Electroanalytical Chemistry, 113, (1980), p. 51—62.

65- D. O. Raleigh, “Electronic Conduction in Bi-BiI_3 Melts. A Theoretical Model”, Journal of Chemical Physics, 38(7), April 1st (1963), p. 1677-1684.

66- S.R. Morrison, “The Chemical Physics of Surfaces”, Plenum Press, New York, (1977).

67- J. Halpern and L. E. Orgel, “Oxidation-Reduction Reactions in Ionizing Solvents. Introductory Paper Electron-Transfer Reactions”, Discuss. Faraday Soc., 29, (1960), p. 7-20

68- F. A. Cotton, G. Wilkinson, C. A. Murillo “Advanced Inorganic Chemistry”, New York: Wiley, (1999), p. 1355.

69- H. Taube, “Advances in Inorganic Chemistry and Radiochemistry”, Academic Press, New York, 1, 1, (1959).

70- M. C. Petty, “Molecular Electronics: from Principles to Practice”, Wiley, (2007), P. 114.

71- W. F. LIBBY “Electron Transfer among the Transition Elements; the Controlling Role of the Franck-Condon Principle on Rates”, Journal of Chemical Physics, 18(2), 15 Jan. (1963).

72- J. Owen, “Experiments on Charge Transfer and Exchange Interactions”, Discussions of Faraday Society, 26, (1958), p. 53-57.

73- L. F. Grantham,and S. J. Yosim, “Electrical Conductivities of Molten Bi-BiI_3 Solutions”, Journal of Chemical Physics, 38(7), April 1st (1963).

74- A. H. W. Aten, Zeitschrift fur Physikalische Chemie (Z. Physik. Chem.), 66, (1909), p. 641.

75- A. H. W. Aten, Zeitschrift fur Physikalische Chemie (Z. Physik. Chem.), 73, (1910), p. 578.

76- H.R. Bronstein and M.A. Bredig, "The Electrical Conductivity of Solutions of Alkali Metals in Their Molten Halides", Journal of American Chemical Society, 80, (1958), p. 2077-2081.

77- H. R. Bronstein and M. A. Bredig, "The Electrical Conductivity of Solutions of Metals in Their Molten Halides. II. Sodium-Sodium Iodide, Potassium-Potassium Iodide, Potassium-Potassium Fluoride", Journal of Physical Chemistry, 65 (7), (1961), p. 1220–1224.

78- H. R. Bronstein, A. S. Dworkin, and M. A. Bredig, "Electrical Conductance of Solutions of Salts in Liquid Metals. Potassium Iodide in Potassium", Journal of Chemical Physics, 34, (1961), p. 1843.

79- A. S. Dworkin, H. R. Bronstein and M. A. Bredig, "Ionic Melts as Solvents for Electronic Conductors", Discussions of Faraday Society, 32, (1961), p. 188-196.

80- L. F. Grantham, "Electrical Conductivity of Molten Mercuric-Mercurous Halide Systems", Journal of Chemical Physics, 49 (9), Nov. (1968).

81- J. R. MacCallum and C. A. Vincent, "Polymer Electrolyte Reviews -1", Elsevier Applied Science Publishers Ltd, (1987).

82- W. D. Callister, "Materials Science and Engineering: An Introduction", 7th Edition. New York, USA: John Wiley & Sons, (2007).

83- M. E Orazem, B. Tribollet, “Electrochemical Impedance Spectroscopy”, John Wiley & Sons, Inc., (2008).

84- G. Couturier, J. Salardenne, C. Sribi, M. Rosso, “Electronic and Ionic Conductivity Measurements in Ionic Conductors with a High Band Gap”, Solid State Ionics, Vol.9-10, Part 1, Dec. (1983), p. 699-705.

85- S. L. Schiefelbein, N. A. Fried, K. G. Rhoads, and D. R. Sadoway, “A High-Accuracy, Calibration-Free Technique for Measuring the Electrical Conductivity of Liquids”, Review of Scientific Instruments, 69 (9), Sep. (1998), p. 3308-3313.

86- J. A. A. ketelaar and P. P. E. Maenaut, “Conductivite Electrique du Chlorure de Sodium Fondu et Son Emploi Comme Sel de Reference a 1000˚C”, Electrochimica Acta, 17, (1972), p. 2195 to 2203.

87- G. J. Janz, C. Solomons, and H. J. Gardner, “Physical Properties and Constitution of Molten Salts Electrical Conductance, Transport, and Cryoscopy”, Chemical Reviews, 58 (3), (1958), p. 461–508.

88- G.D. Robbins, “Measurement of Electrical Conductivity in Molten Fluorides. A Survey”, Journal of the Electrochemical Society, 116 (6), (1969), p. 813.

89- F. Kohlrausch, L. Holborn, and H. Diesselhorst, “Neue Grundlagen fur die Werthe der Leitvermogen von Electrolyten”, Wied. Ann. Phys., 64, (1898), P. 417-455.

90- G. J. Janz and R. P. T. Tomkins, “Conductance Cell Calibrations: Current Practices”, Journal of the Electrochemical Society: Reviews and news, 124 (2), Feb. (1977), p. 55C- 59C.

91- H. C. Parker and E. W. Parker, Journal of American Chemical Society, 46, (1924), p. 312.

92- G. Jones and C. Bradshaw, Journal of American Chemical Society, 55, (1933), p. 1780.

93- R. Forthmann, G. Vogel, and A. Schneider, “Chemie der Seltenen Erden in geschmolzenen Alkalichloriden. I. Schmelzen von Alkalichloriden mit Lanthanchlorid und Neodymchlorid”, Z. Anorg. Chem., 367, (1969), p. 19.

94- D. Gagescu, “A Technique for Measurement of Molten Salt Electrical Conductivity in Low Constant Cells”, Chemical Instrumentation, 6, (1975), P. 93-106.

95- A. Mali, “Modification of Ceramic Components for the Sodium Nickel Chloride Battery”, PhD Thesis, McMaster University, Canada, January 2011.

96- D. L. Maricle and D. N. Hume, “Polarography in a Sodium Chloride-Potassium Chloride Melt Using Tungsten-in-Vycor Microelectrodes”, Analytical Chemistry, 33 (9), August (1961), p. 1188-1192.

97- R. E. Franklin, E. C. G. Kirk, J. R. A. Cleaver, and H. Ahmed, “Channeling Ion Image Contrast and Sputtering in Gold Specimens Observed In a High-Resolution Scanning Ion Microscope”, Journal of Materials Science Letters, 7, (1988), p. 39-41.

98- L. A. Giannuzzi, and F. A. Stevie, “Introduction to Focused Ion Beams, Instrumentation, Theory, Techniques and Practice”, Springer, New York, November 19, (2004).

99- I.S. Yaffe and E.R. Van Artsdalen, “Electrical Conductance and Density of Pure Molten Alkali Halides”, Journal of Physical Chemistry, 60 (1956), p. 1125-1131.

100- R. H. Moss, “Electrochemical Studies on Molten Salt Mixtures of Aluminum Chloride and Alkali Halide”, PhD Thesis, university of Connecticut, USA, 1955.

101- W. Weppner and R. A. Huggins, “Determination of the Kinetic Parameters of Mixed-Conducting Electrodes and Application to the System Li_3Sb”, Journal of the Electrochemical Society, 124 (10), Oct. (1977), p. 1569-1578.

102- K. Huber and E. Jost, “Die P-T-X-Phasendiagramme der Binären Systeme von Niobpentachlorid bzw. Tantalpentachlorid mit Alkalichloriden”, Helvetica Chimica Acta, New York, NY, Wiley-VCH, 41 (7), (1958), p. 2411-2424.

103- C. Rosenkilde and T. Østvold, “Chemistry of Niobium Chloride in the Cs-Cl-NaCl Eutectic Melt. 1. Electromotive Force Measurements of NbCl3 in the CsCl-NaCl Eutectic Melt at Temperatures between 600 and 700˚C”, Acta Chemica Scandinavica, 48, (1994), p. 732-737.

104- J. Dartnell, K. E. Johnson, and L. L. Shreir, “Electrochemistry of Niobium in Fused Halides” Journal of Less Common Metals, 6 (2), Feb. (1964), p. 85-93.

105- C. Vincent, B. Scrosati, “Modern Batteries: An Introduction to Electrochemical Power Sources”, 2nd Edition, Butterworth-Heinemann, Oct. 10, (1997).

106- D. Inman and D. G. Lovering, “Ionic Liquids”, New York : Plenum Press, (1981).

107- G. L. Soloveichik, R. L. Hart, and J. P. Lemmon, “Composition and Energy Storage Device”, United State Patent, Pub. No.: US 2012/0077070 A1, March 29, (2012).